Study of Plasma-Based Acceleration for High Energy Physics and Other Applications

Zur Erlangung des akademischen Grades eines
DOKTORS DER NATURWISSENSCHAFTEN

von der Fakultät für Physik
des Karlsruher Institutes für Technologie (KIT)

genehmigte
DISSERTATION
von

Dipl.-Phys.
Steffen Hillenbrand
aus Stuttgart

Contents

1. Introduction

Ever since beams of charged particles have been technologically realized towards the end of the 19th century, they have led to many great discoveries in fundamental physics; the most recent being the discovery of the Higgs Boson at CERN (cf. e.g. [1]). As the studied phenomena progressed to smaller and smaller scales - from atoms through nuclei to sub-atomic particles - the energy of the beams used to study them had to grow continuously. As a consequence, the size and cost of the particle accelerators used to generate these beams grew accordingly - from the table top device used by Lenard in the 1890s [2] to the 27 km circumference of LEP/LHC [3, 4] (Large Electron Positron collider/Large Hadron Collider). Even though the beam energies and luminosities required for the study of rare particles and processes continue to grow [5, 6], it is not clear how long it will be politically and economically affordable to construct larger and larger accelerators.

In particular, as the beam energy kept increasing, the transition from linear to circular accelerators was made. This allows to send the particle beam through the same accelerating structure many times, significantly reducing the number of required components and the associated costs. However, if charged particles are deflected in a magnetic field, they loose energy through a process referred to as synchrotron radiation [7]. The amount of power lost scales with the Lorentz factor of the particles γ and the deflection radius ρ as $W_{loss} \propto \gamma^4/\rho^2$. This means that if one wanted to double the final beam energy of LEP - the largest lepton collider built to date - one would have to quadruple the circumference to 108 km to keep the power loss constant. Otherwise, one would have to accept 16 times higher losses, corresponding to Gigawatts of power lost to highly energetic electromagnetic radiation. For future high energy lepton collider projects, it is therefore more efficient to go back to linear accelerators. Depending on the exact layout and the desired final beam energy, this results in facilities with a length of a few 10s of kilometres [5, 6]. One way to reduce this length is to increase the acceleration gradient, and, therefore, the energy gain the particles obtain in a given distance. However, for metallic acceleration structures (referred to as cavities), said gradient is limited to $\lesssim 100\,\mathrm{MV/m}$ due to discharges and material breakdown [5, 6].

One possibility to overcome the limit in acceleration gradient for conventional cavities is the use of plasma-based acceleration techniques. In 1979, it has been suggested by Tajima and Dawson [8] to use a plasma - an ionized gas - to transfer the energy of a high-power laser pulse to accelerate electrons. In the process referred to as Laser WakeField Acceleration (LWFA), the laser pulse disperses the plasma electrons from its path due to its ponderomitive force. After the laser pulse has passed, the plasma electrons oscillate back towards the laser beam axis, creating a locally over-dense region. The resulting space charge separation follows the laser pulse, the laser is driving a plasma wake. The longitudinal electric fields resulting from the plasma electron density modulation are used to accelerate electrons, the so called witness bunch. Without the limitation of material breakdown, this mechanism allows to increase the acceleration gradient by several orders of magnitude.

Since the invention of chirped pulse amplification in 1985 [9], the peak power of laser systems increased continuously, soon reaching the powers necessary to study the proposal by Tajima and Dawson. The field of laser wakefield acceleration has seen tremendous progress since. In 2006, electron beams have been accelerated to GeV energies within a centimetre scale plasma [10], corresponding to an energy gain of $\approx 100\,\mathrm{GeV/m}$. For comparison, reaching GeV energies using conventional accelerator technology requires tens of meters of acceleration distance. It is therefore hoped that plasma based acceleration techniques will allow to significantly reduce the size and cost of future lepton accelerators. However, current-day laser systems either feature a much too low energy to accelerate electrons/positrons to the desired TeV energies in a single stage, or their repetition rate is much too low to produce the data rates required for high energy physics experiments [11]. The required beam energy can be reached via staging of several acceleration modules operating at higher repetition rates (and a lower energy gain per stage). However, due to the physics of the laser-plasma interaction, the staging of several (hundred) plasma cells requires an alignment on the sub-micrometer scale and a temporal synchronization in the order of femtoseconds - which is technically very challenging. The number of required stages can be reduced if the energy of the driving pulse - the so called driver - is increased. One possibility to achieve this increase in driver energy with a reasonable repetition rate is to use particle beams instead of laser pulses [12, 13]. However, a limitation arises from the so called transformer ratio [14], which states that the energy gain of the witness bunch cannot exceed twice the energy of the driving particles, regardless of the ratio of charge between the two bunches. This means that if one were to efficiently accelerate electrons/positrons to TeV energies in a single plasma stage, one would require a driver of about half that energy. As mentioned before, it is not possible to generate electron beams of this energy in a circular accelerator due to synchrotron radiation losses. In other words, this option would again require a conventional, linear accelerator of several kilometres length.

The amount of energy lost to synchrotron radiation in a circular accelerator is, via γ, inversely proportional to the mass of the particle to the fourth power. For the same final energy, synchrotron radiation losses can therefore be reduced by 13 orders of magnitude if protons are accelerated instead of electrons. As they can be accelerated efficiently to

very high energies, it has been suggested by Caldwell et al. to study protons as potential drivers for high energy lepton accelerators [15].

In this work, different proposals for plasma-based linear collider found in the literature are reviewed; and protons, electrons and laser pulses as different driver technologies are compared. Based on these studies, three different scenarios for a facility capable of producing the recently discovered Higgs boson [16, 17] are developed and compared to the more conventional proposals ILC and CLIC [5, 6] (International Linear Collider, Compact LInear Collider).

As the technology required for these proposals will still take a few decades to mature [11], possible earlier applications are also investigated. In particular, LWFA are investigated as injectors for synchrotron light sources. As the ultra-short pulses customary for LWFA result in very interesting radiation properties, particular emphasis is put on the evolution of such a bunch in a storage ring.

In addition, studies carried out for the AWAKE experiment at CERN are described. Starting 2015, AWAKE aims to demonstrate proton-driven electron acceleration in a 10 m long plasma cell [18, 19].

The structure of this work is the following: After this introduction, the thesis begins by giving an introduction to the physics of plasma based acceleration and high-power laser systems in chapter 2. To put the following theoretical studies into perspective, a brief overview of the current status of plasma-based acceleration research is given in in chapter 3.

In chapter 4, plasma-based high energy lepton collider are discussed. In section 4.1, the general power requirements, and the phenomena at the interaction point are described. Whilst the fundamental mechanisms are independent of the acceleration method, significant differences will arise due to the different beam parameters resulting from the acceleration process. In the following sections 4.2 to 4.6, several collider proposals found in the literature are discussed. Starting from these results, I have investigated three scenarios for a plasma-based linear collider capable of producing the recently discovered Higgs boson. They are introduced and discussed in section 4.7.

To allow for an earlier technical application of plasma based acceleration techniques, I have studied the possibility to use laser wakefield accelerators as injectors for synchrotron light facilities in chapter 5.

Finally, investigations performed for the proton-driven plasma wakefield experiment AWAKE at CERN are described in chapter 6. After a short introduction to the experiment is given in section 6.1, section 6.2 describes my evaluation of the existing beam-plasma simulations and their consequences for the experiment. Section 6.3 describes my studies for possibly proton and electron energy spectrometer.

2. Theory of Plasma Based Accelerators

This chapters aims to give a theoretical foundation for the possible applications of plasma-based acceleration techniques discussed in chapters 4 to 6. After a brief introduction to plasma-based acceleration is given in section 2.1, sections 2.2 and 2.3 introduce important concepts from classical accelerator physics and plasma physics respectively. Following a short introduction to the physics of the required high-power laser-systems in section 2.4, laser-driven plasma-based acceleration in the linear regime is introduced in section 2.5. The differences for electron- and proton-driven acceleration are discussed in sections 2.6 and 2.7 respectively. Whilst not the main focus of this work, acceleration in the nonlinear regime is introduced in section 2.8 for completeness.

For perspective, the current state of the art is discussed in chapter 3.

A summary of the used acronyms and variables is given in the appendix, sections A and B respectively.

2.1 Introduction to Plasma Based Acceleration

2.1.1 General Principle

Conventional accelerators are limited to acceleration gradients on the order of $100\,\mathrm{MV/m}$ due to electrical breakdown [6]. This limitation can be overcome with plasma-based acceleration schemes, in which the plasma acts as a transformer, transferring the energy of a so-called driver to a so-called witness bunch. The general mechanism is the following [12, 20]: The driver pushes the electrons of the previously homogeneous plasma out of its path. (The plasma ions with their much higher inertia can normally be treated as immobile.) Due to the relativistic velocity of the driver, this displacement is almost solely transverse. The created displacement results in a space charge separation and therefore electric fields, acting to restore the equilibrium. Once the driver has passed, the plasma electrons are accelerated back towards the beam propagation axis, creating a region of enhanced electron density. They overshoot the equilibrium position, resulting in a harmonic oscillation of the plasma electrons around the beam propagation axis. This density

modulation results in longitudinal electric fields between the regions of higher and lower electron density, which in turn can be used to accelerate the witness bunch. The density modulation created by a laser driver is illustrated in figure 2.1.

2.1.2   Linear and Non-Linear Regime

For plasma based acceleration, there are two fundamentally different regimes; the (quasi-) linear and the non-linear regime [20].

In the linear regime, the density modulation is small and quasi sinusoidal, resulting in an electric field distribution which allows the acceleration and focusing of both electrons and positrons.

In the non-linear regime, the driver expels all plasma electrons from its path, leaving behind an electron free bubble (therefore, this regime is also referred to as blowout or bubble regime). The stronger density modulation results in stronger accelerating fields, and the pure ion column within the bubble has very attractive focusing properties for electron witness beams. However, for positrons the whole bubble is defocussing, and they can only be accelerated in the very narrow end of the bubble. For them, the attractive features of this regime are lost.

The difference between the two regimes is illustrated in figure 2.1.

2.1.3   Overview of Different Driver Technologies

A plasma can be driven either by a high intensity laser or a beam of charged particles. A laser driven accelerator is commonly referred to as Laser Wake Field Accelerator (LWFA), a beam driven accelerator as Plasma Wake Field Accelerator (PWFA). A laser driver creates the plasma wake due to its ponderomotive force, a particle beam driver creates the wake due to its Coulomb force. Whilst the general mechanism creating the plasma electron density modulation is very similar for both driver technologies, there are some differences worth noting:

i) For the laser systems currently used for LWFA, the energy stored in a laser pulse is normally in the order of a few Joule (cf. chapter 3.1.2), much lower than the energy that can be stored in a particle beam. This has direct implications for the maximal possible energy gain per acceleration stage.

ii) For a laser driver, the phase velocity of the created plasma wake is approximately equal to the group velocity of the laser pulse, with a relativistic γ normally in the order of 10-100. For a short beam driver, the phase velocity of the wake is given by the velocity of the drive beam, and the γ factor can be several orders of magnitude higher [12, 20, 22]. The lower phase velocity of a LWFA can lead to phase slippage between the laser driver and a witness bunch of high energy, limiting the achievable energy gain per stage. For acceleration in the bubble regime, the wake phase velocity also has direct implications for the trapping of plasma electrons. The lower phase velocity for LWFA allows the trapping of background electrons, thereby creating a witness bunch of appropriate length without the need for an injector. However, this can also lead to dark currents and an increased energy spread due to continuous injection of background electrons into the bubble.
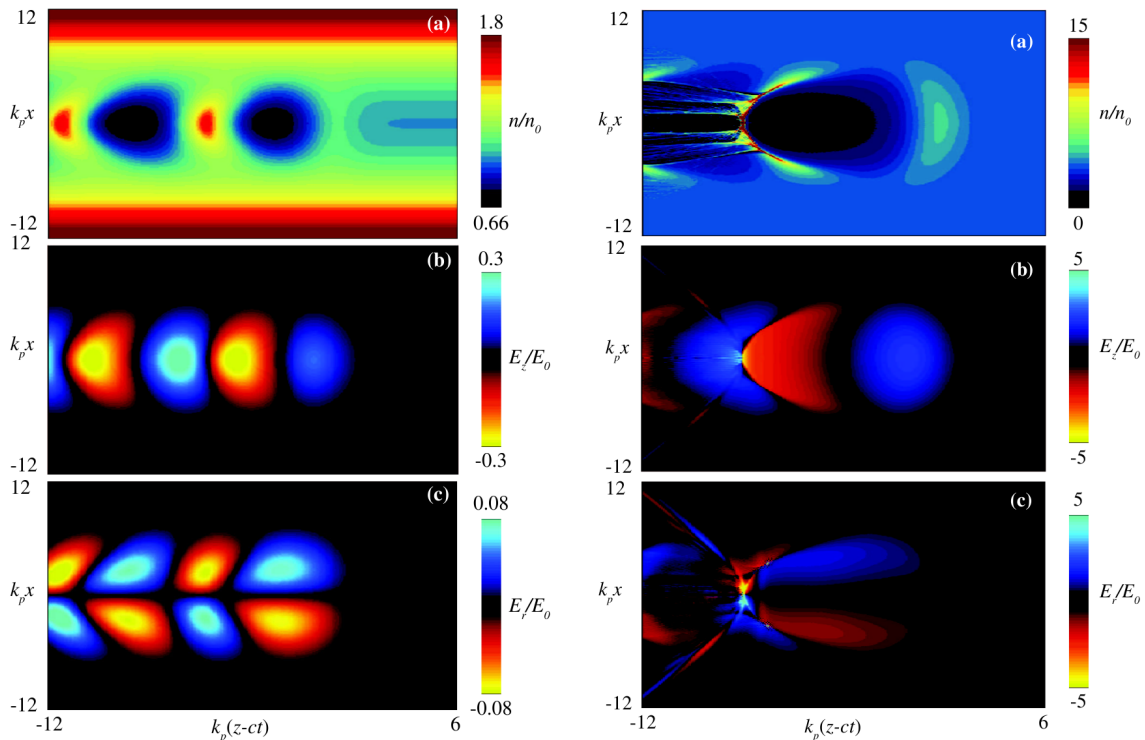
Figure 2.1: Plasma electron density distribution (a), and resulting longitudinal (b) and transverse (c) electric fields for the quasi linear regime (left) and the non-linear bubble regime (right); as simulated in [21]. The laser driver is propagating to the right, centred at $k_p(z - ct) = 0$. For both cases, the driver modulates the plasma electron distribution, resulting in strong space charge fields which can be used to accelerate and focus a so called witness bunch. In the quasi linear regime, the resulting density modulation is close to sinusoidal, resulting in close to symmetric patterns for the electric fields. Regions in which the fields are both accelerating ($E_z < 0/E_z > 0$) and focusing (E_r pointing away from / towards the propagation axis) are present for both electrons / positrons. In the bubble regime, the accelerating fields are significantly higher (note the different scales for the colour maps), and the whole bubble is focusing for electrons. However, positrons can only be focused and accelerated at the density spike at the end of the bubble at $k_p(z - ct) \approx -7.5$. For them, most of the attractive features of this regime are lost. Distances are normalized to the plasma skin depth k_p^{-1} ($\approx 15\,\mu$m for $n_0 = 10^{17}\,\text{cm}^{-3}$, see chapter 2.3.2); densities are normalized to the background plasma density n_0; electric fields are normalized to the classical wave breaking field E_0 ($\approx 30\,\text{GV/m}$ for $n_0 = 10^{17}\,\text{cm}^{-3}$, cf. chapter 2.3.3). The simulations for the linear regime use a preformed parabolic plasma channel, cf. chapter 2.5.4. Figure property of C.B. Schroeder, used with permission.

iii) The interaction cross section for a laser driver is given by its transverse profile. A beam driver, however, will always interact with plasma electrons up to one skin depth away, due to its Coulomb interaction (even for an infinitesimally narrow drive beam) [23, 24].

High power laser systems and laser wake field acceleration will be discussed in more detail in sections 2.4 and 2.5. Electron and proton beam drivers will be discussed in chapters 2.6 and 2.7 respectively.

2.2   Basic Accelerator Physics

Before going into the theory of plasma-based acceleration methods, some concepts of classical accelerator physics shall be reviewed first.

2.2.1   Emittance

For a bunch with 10^7 or more particles, it is not practical to solve the equations of motion for all particles. It is therefore customary to describe the bunch via its 6D phase space volume. Neglecting coupling in a linear approximation, this volume can be split into three independent 2D planes. For each spatial direction, the particles occupy an RMS area A in phase space. The geometric emittance is defined as [25, 26]

$$\epsilon_{geo} = \pi \cdot A. \tag{2.1}$$

As it is customary to give transverse momenta as the angle with the reference trajectory, the emittance is given in m·rad. This has the corollary that the geometric emittance decreases for increased longitudinal momentum. It is therefore useful to define a normalized emittance to allow easier comparison between bunches of different longitudinal momentum

$$\epsilon_N = \beta\gamma\epsilon_{geo}, \tag{2.2}$$

with the common definitions [27] $\beta = \sqrt{1 - \frac{1}{\gamma^2}}$, $\gamma = \frac{E_{kin} + m_0 c^2}{m_0 c^2}$ and m_0 the rest mass of the particle.

2.2.2   Beta-Function

Commonly, quadrupole magnets are used to focus particle beams. Let $k(s)$ be their position dependent strength, then the equation of motion for the beam particles is given by [25]

$$u''(s) - k(s)u(s) = 0. \tag{2.3}$$

The function $u(s)$ describes the transverse position as function of the position along the beam path With the ansatz

$$u(s) = A \cdot u(s) \cos\left[\psi(s) + \phi\right] \tag{2.4}$$

and for constant amplitude A and phase ϕ, one gets

$$u''(s) - \frac{1}{u^3(s)} - k(s)u(s) = 0. \tag{2.5}$$

This allows to define the beta function β as [25]

$$\beta(s) := u^2(s). \tag{2.6}$$

Combined with the constant emittance, it yields the RMS beam size via [25]

$$\sigma(s) = \sqrt{\epsilon_{geo}\beta(s)}. \tag{2.7}$$

Without further focusing and noting β^* as the value of the beta-function at the focus point, the beta value $\beta(s)$ after a drift of length s is given by [28]

$$\beta(s) = \beta^* + \frac{s^2}{\beta^*}. \tag{2.8}$$

It is important to mention that due to the field structure of a quadrupole, it is focusing in one plane and defocusing in the orthogonal plane. However, since the focusing strength depends on the transverse position, a net focusing in both planes can be achieved using two or more quadrupoles, cf. e.g. [29].

Phase Advance

The phase advance from a given point to a position s_0 is defined by the integral over the β function along the reference trajectory [29],

$$\mu(s_0) = \int_0^{s_0} \frac{1}{\beta(s)} ds. \tag{2.9}$$

2.2.3 Dispersion

For a particle with a deviation from the reference momentum $\delta = \Delta p/p_0 \ll 1$, equation 2.3 becomes[1] [26]

$$u''(s) - k(s) = \frac{1}{\rho_0}(s)\delta, \tag{2.10}$$

with ρ_0 the bending radius in a dipole magnet for a particle with reference momentum. Solving equation 2.10 allows to define a dispersion function $D(s)$, with $\delta D(s)$ giving the offset from the ideal trajectory for a particle with energy deviation δ. For Gaussian beams and non-zero dispersion, the beam size increases to [26]

$$\sigma(s) = \sqrt{\beta(s)\epsilon_{geo} + D^2(s)\delta^2}. \tag{2.11}$$

2.3 Introduction to Plasma Properties

A plasma is a state of matter similar to a gas, in which a certain amount of the particles is ionized. The high number of charge carriers make a plasma electrically conductive, and it responds strongly to electric and magnetic fields. Plasmas are quasi-neutral, meaning that

---

[1] Note that to be consistent with equation 2.3, we follow the sign convention for k used in [25]. This results in a minus sign on the left hand side of equation 2.10, as opposed to the plus sign given in the reference.

on macroscopic scales they are electrically neutral in spatial and temporal average. An over-density of charge carriers at a certain position immediately results in electric fields acting to restore the equilibrium.

In general, all the constituents of a plasma have high kinetic energies. Whilst each particle type can normally be described by a temperature T, the different particle types do not need to be in thermal equilibrium [27].

2.3.1 Plasma (Langmuir) Frequency

If the plasma electrons are displaced versus the plasma ions, the Coulomb force acts as restoring force and leads to harmonic oscillations. Assuming cold electrons (i.e. electrons with negligible thermal velocity) and immobile ions, the electron plasma frequency is given by [30]

$$\omega_{pe} = \sqrt{\frac{n_0 e^2}{\epsilon_0 m_e}}, \tag{2.12}$$

where n_0 is the electron number density, e is the elemental charge, m_e is the mass of the electron and ϵ_0 is the permittivity of free space. Substituting the electron mass for the mass of the corresponding ions m_i, one gets the ion plasma frequency

$$\omega_{pi} = \sqrt{\frac{n_0 Z^2 e^2}{\epsilon_0 m_i}},$$

with Z the charge state of the ion. As the ions move out of phase with the electrons the total oscillation frequency is given by

$$\omega_p^2 = \omega_{pe}^2 + \omega_{pi}^2.$$

If not noted otherwise, the approximation $\omega_p \simeq \omega_{pe}$ is made.

In practical units,

$$\omega_{pe}[\text{Hz}] \approx 5.64 \cdot 10^4 \sqrt{n_0[\text{cm}^{-3}]}. \tag{2.13}$$

2.3.2 Plasma Wavelength, Plasma Skin Depth

For a plasma, the collision-less skin depth results from the dispersion relation $c^2 k^2 = \omega^2 - \omega_p^2$. For $\omega < \omega_p$, k becomes imaginary, the wave decays exponentially. For $\omega \ll \omega_p$ [30]:

$$k_p^{-1} = \frac{c_0}{\omega_p} = \frac{\lambda_p}{2\pi} = \sqrt{\frac{c_0^2 \epsilon_0 m_e}{n_0 e^2}}, \tag{2.14}$$

with λ_p the plasma wavelength. In practical units

$$\lambda_p[\text{mm}] = \frac{3.3 \cdot 10^7}{\sqrt{n_0[\text{cm}^{-3}]}}. \tag{2.15}$$

The correlation between plasma wavelength and density is illustrated in figure 2.2.
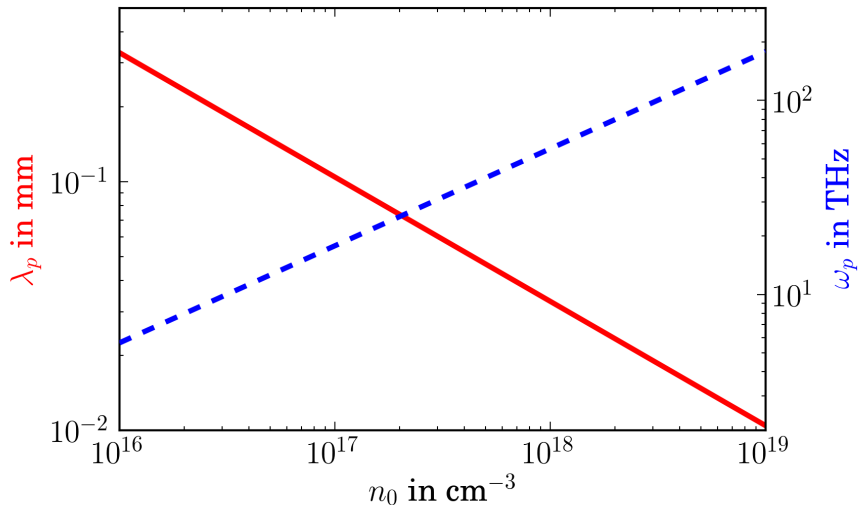
Figure 2.2: Plasma wavelength λ_p (red solid line) and plasma angular frequency ω_p (blue dashed line) over the average plasma electron density n_0.

2.3.3 Wave Breaking Field

A plasma can sustain fields in excess of the so called cold non-relativistic wave breaking field [31] (for which the thermal velocities and the relativistic mass increase of the electrons are neglected in the derivation). In one dimension, wave breaking happens when the oscillation amplitude of the plasma wave becomes bigger than one plasma wavelength, i.e. $k_p z \approx 1$, $z \approx eE_z/m\omega_p$. From Gauss's law the critical longitudinal field is [31]

$$E_0 = \frac{m_e c \omega_p}{e} = \sqrt{\frac{n_0 m_e c^2}{\epsilon_0}}. \tag{2.16}$$

Note that the electric field E_z can exceed E_0 for nonlinear plasma wakes. Simulations have shown that the scaling $E_z \propto E_0$ is still valid in the nonlinear regime [32].
In practical units

$$E_0[\text{V/m}] \approx 96\sqrt{n_0[\text{cm}^{-3}]}. \tag{2.17}$$

2.4 Introduction to High Power Lasers

Before laser-driven plasma-based acceleration techniques will be discussed in chapter 2.5, some important laser parameters shall be introduced.

2.4.1 Optical Intensity

The optical intensity is defined as the optical power per unit area, transmitted through an imaginary surface perpendicular to the propagation direction. For a monochromatic propagating wave such as a plane wave or a Gaussian beam, the local intensity I is related to the electric field amplitude E_L via [33]

$$I = \frac{v_p \varepsilon_0 \varepsilon_r \mu_r}{2}|E_L|^2 = \frac{c\varepsilon_0 n}{2}|E_L|^2, \tag{2.18}$$

with v_p the phase velocity, c the speed of light in vacuum and n the refractive index. For a Gaussian beam with optical power P and beam radius r_L, the peak intensity on axis is [33]

$$I_P = \frac{P}{\pi r_L^2/2}.$$

This is two times higher than one would naively assume.

For the high energy lasers considered in the scope of this work the electric fields of the laser E_L are in the order of 10^{10} to 10^{11} V/m, higher than the atomic electric field $E_{at} \simeq 5 \cdot 10^9$ V/m derived from the Bohr model. This means that any gas is immediately ionized at the very front of the laser pulse and the majority of the pulse propagates in plasma [34].

2.4.2   Laser Strength Parameter

For high power lasers, it is convenient and common to use the normalized electrostatic and vector potentials

$$\phi = \frac{e\Phi}{m_e c^2}, \quad \vec{a} = \frac{e\vec{A}}{m_e c^2}. \tag{2.19}$$

The strength of a laser system is then given by the laser strength parameter a_0, defined as the peak amplitude of the normalized vector potential of the laser field $\vec{a} = a_0 \hat{a}$.

Physically, $\vec{a}$ is the normalized quiver momentum of the electrons in an electric field [20]. In an electric field $\vec{E} = E\hat{e}_x \cos(\omega t - kz)$, a free electron oscillates with a classical velocity amplitude, the so called quiver velocity [34]

$$v_q = \frac{eE}{m_e \omega}. \tag{2.20}$$

If this velocity becomes comparable to c, the relativistic regime is reached. This is determined by the parameter a_0, depending if $a_0 \ll 1$ or $a_0 \gtrsim 1$ [34]:

$$a_0 = \frac{v_q}{c} = \frac{eE}{m_e \omega c}. \tag{2.21}$$

For a peak intensity I of a linear polarized Gaussian laser pulse of shape $\vec{a} = a_0 \exp\left(-\frac{r^2}{r_L^2}\right) \cos(kz - \omega t)\hat{e}_x$, with r_L the RMS laser spot radius and λ, ω the laser wave length and frequency respectively [20]:

$$a_0 = \sqrt{\frac{2e^2\lambda^2 I}{\pi m_e^2 c^5}} \simeq 8.6 \cdot 10^{-10} \lambda[\mu\mathrm{m}]\sqrt{I[\mathrm{Wcm}^{-2}]}. \tag{2.22}$$

It relates to the laser power P and the peak transverse electric field amplitude E_L via

$$P[\mathrm{GW}] \simeq 21.5 \left(\frac{a_0 r_L}{\lambda}\right)^2, \tag{2.23}$$

$$E_L[\mathrm{TV/m}] \simeq 3.2 \frac{a_0}{\lambda[\mu\mathrm{m}]}. \tag{2.24}$$

2.4.3   Polarization

A plane light wave can be described by is vector potential [35]

$$\vec{A}(r,t) = \Re\left(\vec{A}_0 e^{i\psi}\right), \tag{2.25}$$

where r and t are the space and time coordinates and $\psi = \vec{k} \cdot \vec{r} - \omega t$ is the phase. For linear polarization (LP), $\vec{A}_0 = A_0 \hat{e}_y$. For circular polarization (CP), $\vec{A}_0 = A_0(\hat{e}_y \pm i\hat{e}_x)$, with the sign depending on the rotation direction. With the dispersion relation in vacuum $\omega = |\vec{k}|c$ the electric and magnetic fields are then given by

$$\vec{E} = \Re\left(-\frac{i\omega}{c}\vec{A}_0 e^{i\psi}\right), \qquad \vec{B} = \Re\left(i\vec{k} \times \vec{A}_0 e^{i\psi}\right). \tag{2.26}$$

With the pointing vector $\vec{S} = \frac{c}{4\pi}\vec{E} \times \vec{B}$, the intensity of the light is given by

$$I = |\vec{S}| = \frac{\omega k}{8\pi}A_0^2 \cdot \begin{cases} 1 + \sin 2\psi & \text{for LP}, \\ 2 & \text{for CP}. \end{cases} \tag{2.27}$$

For linear polarization, the intensity oscillates with twice the phase, while it is constant for circular polarization. As a result, the averaged intensity is [35]

$$\bar{I}\lambda^2 = \xi\frac{\omega k\lambda^2}{8\pi}A_0^2 = \xi\frac{\pi}{2}cA_0^2 = \xi\frac{\pi}{2}P_0 a_0^2, \tag{2.28}$$

with $\xi = 1$ for linear polarization, $\xi = 2$ for circular polarization, and the relativistic power unit $P_0 = m^2 c^5/e^2 \simeq 8.7\,\text{GW}$.

For monochromatic light, circularly polarized light can be transformed into linearly polarized light and vice versa using a $\lambda/4$ optical wave plate. For non-monochromatic waves, full conversion is only achieved in a limited wavelength range [33].

2.4.4   Laser Wavelength, Chirped Pulse Amplification

To date, almost all of the highest energy laser systems depend on the method of Chirped Pulse Amplification (CPA) [9, 33, 36]. This method allows us to overcome previous energy limitations due to the damage potential of the high intensity laser beam to the gain medium and the optical components. In CPA, a ultrashort but spectrally broad laser pulse is positively chirped and temporally stretched by several orders of magnitude, meaning that the high frequency part of the spectrum lags behind the low frequency part. The low intensity beam is then introduced into the gain medium, where it is amplified by several orders of magnitude, before it is recompressed. To recompress the beam to ultra short durations (and therefore reach highest intensities), all spectral components must experience the same gain during the amplification progress. This limits the usable gain media to a few possibilities and the laser (carrier) wavelength to near infrared, $\lambda_L \approx 1\,\mu\text{m}$ [36].

If higher frequencies are desired, frequency multipliers can be used, several times if necessary [33].

2.4.5   Rayleigh Length

The Rayleigh length of a laser beam is the distance along its propagation direction after which the cross section of the beam doubles, measured from the beam waist (i.e. the point where the beam diameter is minimal). For a Gaussian beam in free space propagating in $\hat{z}$ direction, the Rayleigh length is given by [33]

$$z_R = \frac{\pi w_0^2}{\lambda}, \tag{2.29}$$

where λ is the laser wavelength and w_0 is the beam waist. The radius of the beam at a distance z from the waist is given by [20]:

$$w(z) = w_0 \sqrt{1 + \left(\frac{z}{z_R}\right)^2}. \tag{2.30}$$

The Rayleigh length is therefore comparable to the β^* value of classical accelerator physics. For typical laser wavelengths of about $1\,\mu$m and a laser spot diameter at focus in the sub-millimetre range, the Rayleigh length is below $1\,$mm.

2.4.6 Phase and Group Velocity

The phase velocity is the velocity of the wave phase fronts within a given wave. For a laser pulse, it is the velocity of light in the medium through which it propagates. It is given by [27, 33]

$$v_p = \frac{\omega}{|\vec{k}|} = \frac{\lambda}{T}. \tag{2.31}$$

The superposition of two harmonics waves $y_{1/2}(x,t) = A\cos(\omega_{1/2}t - k_{1/2}x)$ with frequencies ω_1, ω_2 and same amplitude A yields a wave, the envelope of which is modulated with $\cos(\Delta\omega t - \Delta k x)$, assuming propagation in $\hat{x}$-direction and $\Delta\omega = (\omega_1 - \omega_2)/2$, $\Delta k = (k_1 - k_2)/2$. The velocity of said modulation is given by $v_g = \Delta\omega/\Delta k$ [27]. A locally confined wave packet can be generated by superposition of an infinite number of harmonic waves with a continuous spectrum. The group velocity is then given by [27, 33]

$$v_g = \frac{\partial\omega}{\partial\vec{k}}. \tag{2.32}$$

Group and phase velocity can be different in a dispersive medium in which the phase velocity depends on the wavelength. The transport of energy through a medium happens with the group velocity.

2.5 Laser-Driven Acceleration in the Linear Regime

2.5.1 Introduction

In 1979, it has been suggested by Tajima and Dawson to use plasmas as a transformer to transfer the energy of a high power laser pulse to an accelerated particle beam [8]. This Laser Wakefield Acceleration (LWFA) mechanism allows the circumvention the so called Lawson-Woodward theorem [37–39], which states that no net energy transfer from an electromagnetic wave to a particle is possible in free space.

Since high power laser systems became readily available after the invention of chirped pulse amplification in 1985 [9], the field of LWFA has seen tremendous progress [20]. Acceleration gradients of over $100\,$GV/m and electron energies of over $100\,$MeV have already been achieved in the mid 1990s [40, 41]. However, these early beams where characterized by an exponential energy distribution, with most electrons at low energies and only a few high energy particles in the tail of the distribution. This dramatically changed in 2004, when

three groups independently achieved the production of high quality electron beams with charges of around 100 pC at a mean energy of approximately 100 MeV, low divergence and an energy spread of only a few percent [42–44]. High quality electron bunches of up to 1 GeV have been demonstrated in 2006 using a plasma-channel guided laser pulse [10]. In this chapter, the fundamental mechanisms relevant for LWFA will be reviewed.

2.5.2 Plasma-Based Laser-Driven Accelerator Concepts

While in the following this work will assume LWFA unless otherwise noted, some historically used laser-driven plasma-based acceleration schemes shall be mentioned as well.

Plasma Beat Wave Accelerator - PBWA

In a simplistic way, plasma electrons can be understood as an ensemble of oscillators, oscillating at the plasma frequency. To enforce the resonant swinging of these oscillators, the driver must contain a Fourier component close to the plasma frequency. A short dense driver has a broad spectrum and thus generates the wake field efficiently [45].

Before 1985, the ultra intense, ultra short laser pulses necessary of LWFA were not available. The Plasma Beat Wave Accelerator (PBWA) [8, 20, 46] relies on two long laser pulses with frequencies ω_1, ω_2 and normalized combined vector potential $a = a_1 \cos(k_1 z - \omega_1 t) + a_2 \cos(k_2 z - \omega_2 t)$. When the laser frequencies are adjusted so that the beat term is approximately the plasma period, $\Delta\omega = \omega_1 - \omega_2 \simeq \omega_p$, a plasma wake can be driven resonantly. The phase velocity of the plasma wave is given by $v_p/c \simeq 1 - \omega_p^2/(2\omega_1\omega_2)$. In the limit $\omega_p^2\omega_1^2 \sim \omega_p^2\omega_2^2 \ll 1$ the phase velocity of the wake is approximately given by the group velocity of the driving lasers. The beat wave effectively acts as a series of laser pulses with amplitude $a_1 a_2$ and pulse duration $\Delta\tau = 2\pi/\Delta\omega$, each generating a wake of amplitude $E_{max}/E_0 = \pi a_1 a_2/2$. The total wake amplitude generated by a beat pulse of length $L = N\lambda_p$ is $E_{max}/E_0 = N\pi a_1 a_2/2$, with N the number of beat periods within the pulse.

The results given above are based on linear plasma theory, and several non linear effects have been neglected. In particular, the plasma wave period increases as the plasma wake amplitude increases. Since the beat wave period is fixed, this will eventually lead to dephasing and limit the amplitude of the wake. In [46] the maximal field before saturation has been derived as

$$E_{sat}/E_0 = (16a_1a_2/3)^{1/3},$$

assuming that the beat frequency is exactly the ambient plasma frequency, i.e. $\Delta\omega = \omega_p$. A slightly higher field at saturation can be reached if the beat frequency is detuned to compensate for the lengthening of the plasma wake period [47].

The results above have been derived for weak pump amplitudes $a_1 a_2 \ll 1$, but the general concepts also apply in the highly nonlinear regime, $a_1 a_2 \gtrsim 1$ [20].

Resonant Laser Plasma Accelerator - RLPA

In the previous section, it has been pointed out that the PBWA effectively acts as series of laser pulses, the period of which could be adjusted to compensate for the detuning due to the increase of the plasma wave length with growing wake field amplitude. The

Resonant Laser Plasma Accelerator (RLPA) [20, 48, 49] builds on these findings and drives a plasma wake by a train of short laser pulses, the width and spacing of which is optimized to generate the highest wake field. This way, the saturation of the plasma wake due to resonant detuning can be eliminated.

Self-modulated Laser Wakefield Accelerator - SMLWFA

In the previous two sections, it has been sketched that a series of short laser pulses can drive a large amplitude plasma wake. In the Self-modulated Laser Wakefield Accelerator (SMLWFA) [20, 50–53] a single, long laser pulse is used instead. Under appropriate conditions, this beam can break up into a series of short pulses, each having a width in the order of λ_p. This process is called self modulation and occurs as the plasma wave produces regions of enhanced focusing and diffraction. To operate a SMLWFA, the laser pulse length should be longer than the plasma wave length, $L > \lambda_p$ and the laser pulse power should be larger than the critical power for which laser guiding occurs, $P > P_{crit}(1 - \Delta n/\Delta n_c)$. Here, $P_{crit} \simeq 17.4 \cdot \frac{\omega^2}{\omega_p^2}$ GW is the critical laser power, (which is explained in more detail in section 2.5.4), Δn is the depth of a preformed parabolic plasma channel (if present), $\Delta n_c = 1/(\pi r_e w_0^2)$ is the critical channel depth and r_e is the classical electron radius. Since $\lambda_p \propto n_0^{-1/2}$ and $P_{crit} \propto n_0^{-1}$, the conditions $L > \lambda_p$ and $P > P_{crit}$ can normally be reached by increasing the plasma density (assuming fixed laser parameters).

The SMLWFA concept has two main advantages compared to the standard LWFA: simplicity and increased acceleration. Simplicity in this case means that the laser pulse length does not have to be matched to the plasma density so that $L \simeq \lambda_p$, and that no preformed plasma channel is necessary to guide the pulse. The increased acceleration has four reasons: i) The SMLWFA normally operates at a higher plasma density, which leads to a higher accelerating field $E_z \propto n_0^{1/2}$. ii) The condition $P > P_{crit}$ means that the laser pulse will tend to focus to a higher intensity, and therefore increase E_z by increasing a_0. iii) Relativistic guiding will allow the pulse to propagate for several Rayleigh lengths, thus increasing the acceleration length. iv) As with the PBWA and RLPA the plasma will be excited resonantly by a series of pulses, as opposed to a single pulse in the LWFA.

The main disadvantages of the SMLWFA are: i) At higher densities the laser pulse group velocity decreases. As the plasma wake phase velocity is approximately equal to the laser pulse group velocity, this can lead to dephasing between the plasma wake and the accelerated electrons and thus limit acceleration distance. ii) The dephasing length is short compared to the laser propagation distance. This and continuous trapping of plasma electrons leads to a broad energy spectrum. iii) The modulated pulse structure eventually diffracts.

Experiments have shown that for SMLWFA laser pulses with fast rise times are beneficial [52, 53]. A faster rise time results in a stronger ponderomotive force and therefore a stronger initial plasma wake, acting as a seed for the self-modulation instability.

For the proton-driven AWAKE experiment described in chapter 6, a similar self-modulation of the proton bunch is used to drive the plasma wakefields, cf. section 2.7.2.

Laser Wakefield Acceleration - LWFA

The Laser Wakefield Accelerator (LWFA) [8, 20] uses a single, short ($\lesssim 1\,\mathrm{ps}$), high intensity ($\gtrsim 10^{17}\,\mathrm{W/cm^2}$) laser pulse to drive a plasma wake. When an intense laser pulse propagates through an underdense plasma, the plasma electrons are expelled from the region of the laser pulse. This is due to the ponderomotive force associated with the laser pulse envelope, $F_p \sim \nabla a^2$. (In the context of LWFA, underdense means that $\lambda/\lambda_p \ll 1$, the laser wavelength λ is much shorter than the plasma wavelength λ_p.)

Assuming an axially symmetric laser pulse, the plasma wave is driven most effectively if the laser pulse length L is in the order of the plasma wavelength λ_p, i.e. $L_{RMS} \lesssim \lambda_p$. The exact pulse length L that maximizes the wake amplitude depends on the shape of the axial pulse profile. For a Gaussian laser pulse, the wakefield reaches its maximum, $E_{max} = 0.76a_0^2 E_0$, when $k_p L_{RMS} = 1$, assuming $a_0^2 \ll 1$ [54]. The phase velocity of the excited wake is approximately the laser pulse group velocity.

As the wake is driven by a single pulse with $L \sim \lambda_p$, the amplitude of the exited wake is fairly insensitive to uncertainties in pulse duration and plasma density.

While the PBWA and SMLWFA schemes also produce high gradients and high energy electrons, the general consensus is that LWFA is most suitable for a real accelerator, as the SMLWFA relies on an instability, and the PBWA is susceptible to instabilities or degradation of the phase velocity of the wave, as has been confirmed in simulations [32].

2.5.3 Ponderomotive Force

In an inhomogeneous oscillating electromagnetic field, a charged particle experiences a nonlinear force, the so called ponderomotive force [55]

$$\vec{F}_p = -\frac{e^2}{4m\omega}\nabla\vec{E}^2,\tag{2.33}$$

with e the electrical charge of the particle, m its mass, ω the angular frequency of oscillation of the field and $\vec{E}$ the amplitude of the electric field. In addition to the fast oscillations a particle would experience in a homogeneous field, it also feels a force pushing it towards the regions of lower intensity. This can be understood by considering the motion of a single charge in the oscillating electric field. In a homogeneous field, the charge returns to its original position after one oscillation period. In an inhomogeneous field however, this is not the case, since the force the particle feels at the turning point in the low field area is lower than the one it experiences in the high field area. This results in a net force, the position the charge reaches after one oscillation shifts towards the low field region. The ponderomotive force can therefore be defined heuristically as the gradient of the time-averaged oscillation potential.

2.5.4 Diffraction, Optical Guiding

In vacuum, a focused laser pulse will diffract with the characteristic Rayleigh length, cf. chapter 2.4.5. This diffraction length can be much shorter than the dephasing and depletion length and therefore become the limiting factor for particle acceleration [20]. However, this diffraction can be mitigated by optical guiding of the laser pulse, due to

a lower plasma density on axis than off axis. This in turn can either be achieved by a preformed plasma channel or a sufficiently strong laser as shall be explained below.

For an electromagnetic wave of low intensity propagating through an unmagnetized plasma, the dispersion relation is given by [27, 35]

$$\omega^2 = \omega_{pe}^2 + c^2 k^2 \tag{2.34}$$

where k and ω are the wave number and angular frequency of the wave, c is the vacuum velocity of light and ω_{pe} is the plasma electron frequency. The refractive index n of the plasma is therefore given by

$$n = \sqrt{1 - \frac{\omega_{pe}^2}{\omega^2}} = \sqrt{1 - \frac{n_0}{n_c}} \tag{2.35}$$

defining the critical density for the electromagnetic wave $n_c = \frac{\varepsilon_0 m_e \omega^2}{e^2}$. For $\omega < \omega_p$ ($n_0 > n_c$), the refractive index becomes imaginary and the wave will be reflected. The plasma can be classified as overdense (inhibiting wave propagation) or underdense (allowing wave propagation) with respect to n_c.

However, equations 2.34 and 2.35 only hold for low intensity electromagnetic waves with $a \ll 1$. For high intensities (but still $a < 1$), the plasma electrons will be accelerated to relativistic energies, and their relativistic mass increase has to be taken into account. The refractive index is then given by [34]

$$n = \sqrt{1 - \frac{\omega_{pe}^2(r)}{\omega^2}}, \qquad \omega_{pe}(r) = \sqrt{\frac{n_0(r)e^2}{\gamma(r)m_e\varepsilon_0}} \tag{2.36}$$

The relativistic modification is related to the laser strength via $\gamma(r) \simeq \sqrt{1 + a^2(r)/2}$. For a laser pulse with its peak intensity on axis, the refractive index is maximum on axis and decreases with $\partial n/\partial r < 0$. This means that the wave propagation will be slower on axis than off axis. The resulting curvature of the phase front has the effect of a focusing lens, counteracting the natural diffraction [55, 56].

As explained in chapter 2.4.3, The radiation power of a Gaussian laser beam is given by [35]

$$P = \frac{I_p \pi r_L^2}{2} = P_0 \left(\frac{\omega^2}{16c^2} a_0^2 r_L^2 \right) \cdot \xi \tag{2.37}$$

with I_p the peak intensity on axis, $P_0 = m^2 c^5/e^2 \simeq 8.7\,\text{GW}$ the relativistic power unit, and $\xi = 1$ for linear and $\xi = 2$ for circular polarization of the laser beam. Self focusing occurs if this power exceeds the critical power P_{crit} [57],

$$P_{crit} = 2P_0 \frac{\omega^2}{\omega_p^2} \simeq 17.4 \cdot \frac{\omega^2}{\omega_p^2}\,\text{GW} \tag{2.38}$$

The radial decrease in density $\partial n/\partial r < 0$ can also be achieved via a preformed plasma channel, which allows to guide laser beams of lower intensities. This method has the additional advantage that the plasma channel also acts on the head of the beam [20].

2.5.5 Dephasing

In the linear regime with $a_0 \ll 1$ and neglecting the evolution of the laser driver during its propagation, the phase velocity of the plasma wake is equal to the group velocity of the laser driver [20]. The dispersion relation 2.34 yields $v_g = c(1 - \omega_p^2/\omega^2)^{1/2}$ and $\gamma_g = (1 - v_g^2/c^2)^{-1/2} = \omega/\omega_p$, often resulting in a phase velocity of the wake in the order of $\gamma_p \sim 10 - 100$ [22].

If a witness electron is accelerated, its velocity will increase and approach the speed of light, $v \to c$. As the phase velocity of the plasma wake is constant with $v_g < c$, the electrons can eventually outrun the plasma wake and slip into the decelerating / defocussing region of the wake. This limits the maximum energy gain of the electron and is referred to as dephasing. The dephasing length L_d is defined as the length distance an electron can travel before it slips by half a period of the plasma wake. For a highly relativistic electron with $v \simeq c$, it is given by $(1 - v_p/c)L_d = \lambda_p/2$.

For a linear polarized square profile laser pulse in the 1D limit ($r_0 \gg \lambda$) [20]

$$L_d \simeq \frac{\lambda_p^3}{2\lambda^2} \cdot \begin{cases} 1 & \text{for } a_0^2 \ll 1, \\ \frac{\sqrt{2}}{\pi} \frac{a_0}{N_p} & \text{for } a_0^2 \gg 1 \end{cases} \tag{2.39}$$

where N_p is the number of plasma periods behind the drive laser pulse, and the phase slip is $\lambda_p/4$.

2.5.6 Depletion

During the acceleration process, the driving (pumping) laser pulse transfers its energy to the accelerated witness bunch. For a linear polarized square profile laser pulse in the 1D limit ($r_L \gg \lambda$), where the laser spot radius r_L is much larger than the laser wavelength λ, the so-called pump depletion length L_{pd} after which the laser has given off its energy is given by [20, 58]:

$$L_{pd} \simeq \frac{\lambda_p^3}{\lambda^2} \cdot \begin{cases} 2/a_0^2 & \text{for } a_0^2 \ll 1, \\ \frac{\sqrt{2}}{\pi} a_0 & \text{for } a_0^2 \gg 1 \end{cases}$$

with λ, λ_p the laser and plasma wave lengths respectively. For a Gaussian pulse with a pulse length close to the resonant value the pump depletion length becomes [58]:

$$L_{pd} \simeq 1.3 \frac{\lambda_p^3}{\lambda^2} \cdot \begin{cases} 2/a_0^2 & \text{for } a_0^2 \ll 1, \\ 1 & \text{for } a_0^2 \gg 1 \end{cases} \tag{2.40}$$

For efficient acceleration, one wants the acceleration distance to be equal to the pump depletion length.

2.6 Electron-Driven Acceleration in the Linear Regime

In a very similar way a laser can generate plasma wakes via its ponderomotive force, a charged particle beam can be used to generate a wake due to its space charge force [12, 59–61]. This concept is referred to as Plasma Wakefield Acceleration (PWFA).

2.6.1 Acceleration Gradient

In the liner regime ($n_b \ll n_0$; $eE \ll m_e \omega_p c$), the plasma response to a relativistic bunch with bi-Gaussian density distribution can be calculated by integrating the Green's function for a single electron. For a narrow bunch ($k_p \sigma_r \ll 1$), the maximal field can be approximated by [62]:

$$E = 240 (\text{MVm}^{-1}) \left(\frac{N}{4 \cdot 10^{10}} \right) \left(\frac{0.6 \, \text{mm}}{\sigma_z} \right)^2 \tag{2.41}$$

with N number of particles in the driving bunch and σ_z the rms length.

2.6.2 Transformer Ratio

For particle driven acceleration schemes, a severe limitation comes from the so called transformer ratio for longitudinally symmetric bunches [14, 15]

$$R = \frac{E_{max}^{witness}}{E_{max}^{drive}} \leq 2 - \frac{N_{witness}}{N_{drive}}, \tag{2.42}$$

the ratio between the maximal decelerating electric field in the drive beam E_{max}^{drive} and the maximal accelerating field in the witness beam $E_{max}^{witness}$ for a given ratio of particles per bunch $N_{witness}/N_{drive}$. The energy gain ΔE of an accelerated bunch is given by

$$\Delta E = R \cdot E_{drive}. \tag{2.43}$$

The transformer ratio can be improved to $R \leq 2\sqrt{M} - \frac{N_{witness}}{N_{drive}}$ by using M drive bunches with appropriately varied phase to each other [14]. The transformer can also be improved by using non-symmetric bunches [63]. However, both these methods require manipulation on a time (length) scale much smaller than the plasma frequency (plasma wavelength). Therefore, they are technically very challenging.

2.6.3 Dephasing

For a short drive beam, the phase velocity of the plasma wake is equal to the velocity of the driver, $v_p = v_b$ [12]. Since the relativistic γ-factor of a particle drive beam is normally much higher than the γ-factor associated with a laser driver, dephasing is normally not the limiting factor when using beam drivers [22].

2.6.4 Diffraction, Head Erosion

As a laser pulse is subject to Rayleigh diffraction (chapter 2.4.5), a particle beam diverges on a scale length of β^*, the β value at focus. Whilst the witness bunch can be focused by the transverse fields of the wake, part of the drive beam propagates in neutral gas / homogeneous plasma. Since the plasma wake has not yet been created there, there are no focusing fields present and the beam head is subject to erosion.

2.7 Proton-Driven Acceleration

To complement the Large Hadron Collider (LHC), a high energy lepton collider is desirable. The energy and luminosity requirements for such a collider [64–66] make staging necessary for both laser and electron/positron driven collider schemes. To circumvent the challenges associated with this staging, it has been suggested to study protons as possible drivers [15]. Protons can be accelerated to very high energies using synchrotrons, without excessive losses due to synchrotron radiation emission. The energy stored in a ultra-relativistic proton beam is sufficient to accelerate electrons/positrons to TeV energies in a single stage.

2.7.1 Positively Charged Driver

Theory predicts that in the linear regime, the wake excited by a positively charged driver is the same as for an electron driver, only shifted in phase [15]. Therefore, the points discussed in section 2.6 also hold for proton driver.

However, for the highly nonlinear regime significant differences arise. The drive beam does not 'blow out' the electrons any more, it pulls them towards the beam axis instead. This lead leads to an increase of the local electron density, resulting in a shorter local plasma wavelength. This in turn makes the use of an even shorter drive bunch necessary to excite the wake resonantly [15]. Or, for fixed beam parameters, the necessary plasma density can be up to an order of magnitude lower than what linear theory would predict [67]. However, simulations in [15, 67] show that a bubble similar to that formed by a negatively charged driver is also created by a positively charged driver. The plasma electrons are accelerated towards the axis, overshoot, and create a bubble.

2.7.2 Self Modulated Driver

For the lepton drivers discussed in chapter 2.6, it was possible to compress the drive beam to a length comparable to the plasma wavelength. For the proton driven AWAKE experiment described in chapter 6, this would require a compression by 4 orders of magnitude, translating into GV of RF voltage and kilometres for the bunch compressor chicane [68]. Since this is beyond the scope of a demonstration experiment, it has been decided to use a long proton bunch as driver. This proton bunch will self modulate, comparable to the SMLWFA discussed in chapter 2.5.2 [18, 19, 45]. The modulation occurs due to the coupling of the transverse wake field and the beam radius evolution [22, 45, 69]. In other words, the transverse wake fields will focus and defocus parts of the beam, leading to a density modulation. In turn, this density modulation drives the wake more efficiently. Once the instability develops, nothing can keep the most part of the beam from transverse dispersion [70]. For an illustration of the modulation, cf. figure 6.7, page 6.7.

For the highly relativistic drive beam discussed for our experiment, the longitudinal effect on the beam is very weak [45].

In principle, the self-modulation instability can grow from noise. However, for a not perfectly axis-symmetric beam, other instabilities like hosing (cf. section 2.8.2) can grow on a similar time scale, ruining the beam quality. This can be circumvented by pre-seeding the self modulation instability. As an added benefit, seeding will increase the

shot-to-shot reproducibility and the quality of the wakefield [45]. Possibilities to seed the self-modulation instability include a laser or electron pre-pulse or a sharp step in the proton bunch density [18, 19].

2.7.3 Dephasing

Short Driver

For a short ($\sigma_z \simeq \lambda_p$) proton driver, the phase velocity of the plasma wake is equal to the velocity of the drive beam, as for the PWFA case. It is worth noting however, that due to the higher mass of the proton this makes much higher proton energies necessary to maintain a driver velocity close to the speed of light. Otherwise, dephasing can become the limiting factor. In particular, for $\gamma_e \gg \gamma_p$, this imposes the condition for the phase slippage δ [71]:

$$\delta = k_p \Delta d \approx \frac{1}{eE_{acc}/(m_e c \omega_p)} (\gamma_{e,fin} - \gamma_{e,in}) \left[1 - \frac{\gamma_{p,fin} - \gamma_{p,in}}{\sqrt{\gamma_{p,fin}^2 - 1} - \sqrt{\gamma_{p,in}^2 - 1}} \right] < \pi \quad (2.44)$$

Here, $k_p \Delta d$ is the difference in travelled distance between the protons and the electrons normalized to the plasma skin depth, $eE_{acc}/(m_e c \omega_p)$ is the accelerating field of the plasma wake normalized to the classical wave breaking field and $\gamma_{e,in}, \gamma_{e,fin}, \gamma_{p,in}, \gamma_{p,fin}$ are the initial and final relativistic gamma factors of the electrons and protons respectively.

Note, that although the accelerating gradient and therefore the length of the plasma stage depend on the plasma density, the condition for the phase slippage does not, as the distance the electron may outrun the proton beam also depends on the plasma wave length and therefore the plasma density.

Self Modulated Driver

For the self modulated case, the phase velocity of the wake is not determined by the driver velocity, as one might naively assume. During the development of the instability, it is considerably reduced due to the spatio-temporal nature of the self focusing instability [22, 69]. Due to the instability dispersion, the phase velocity is given by [69]:

$$v_p = v_b \left[1 - \frac{1}{2} \left(\frac{\xi}{ct} \right)^{1/3} \left(\frac{n_b m_e}{2 n_0 m_p \gamma_b} \right)^{1/3} \right] \quad (2.45)$$

with $\xi = \frac{v_b}{c} ct - z$, $\tau = z/c$ and v_b, γ_b and n_b the properties of the drive beam. The γ factor of the wake can be up to an order of magnitude smaller than that of the driver. This is problematic, since it can lead to dephasing with an relativistic electron witness bunch before the instability has reached saturation (and the accelerating field therefore is still low).

Once the instability saturates, the phase velocity of the wake approaches the velocity of the driver again (for the planned experiment, this happens after about 5 m). This implies that the electron witness bunch should be injected at a later point along the plasma, either with a staged approach [22] or via side injection [69, 72].

2.8   Acceleration in the Nonlinear Regime

To also allow the acceleration of positrons for linear collider application, the main part of this thesis is based on acceleration in the (quasi) linear regime. Acceleration in the highly nonlinear regime will therefore only be discussed briefly. For more information, the reader is referred to e.g. [20, 32, 36, 73–76].

None the less, a set of scaling laws with plasma electron density has been derived during the course of this thesis. They are discussed in section 2.8.3. The important concepts of beam matching and hosing will be explained in sections 2.8.1 and 2.8.2 respectively.

Whilst an electron driver will be assumed in the following, the general principles work analogously for a laser driver.

For high enough driver intensities, all plasma electrons can be expelled from some region around the driver propagation axis. Due to the creation of this cavity, this regime is often also referred to as blowout, bubble or cavitation regime.

In addition to the higher accelerating gradient due to the stronger plasma electron density modulation, the structure of the electric fields within the plasma bubble makes it very attractive for the acceleration of electrons. In particular, the accelerating field is constant as a function of radius. Furthermore, the transverse focusing fields increase linearly with radius. This, in turn, leads to a preservation of the normalized witness beam emittance [20]. However, as the transverse fields are focusing for electrons within the whole bubble, they are in turn defocussing for positrons. Positrons can only be focused at the density spike at the very end of the bubble, making their acceleration very difficult [21].

The difference between the linear and the nonlinear regime is illustrated in figure 2.1, page 7.

2.8.1   Beam Matching, Electron Driver

In an underdense plasma with $n_b \gg n_0$, the drive beam creates an ion column, which acts as a thick focusing lens for an electron beam. This causes the beam to undergo betatron oscillations along the length of the plasma [77–79]. There are several advantages if the beam size can be matched to a constant radius [77]: i) Instabilities such as hosing (cf. section 2.8.2) are reduced. ii) Synchrotron radiation losses due to oscillations are minimized. iii) Since the focusing force is constant in both transverse dimensions, an initially matched beam will propagate with no significant change in beam size in spite of large energy gain or loss.

The beam transport in an ion column can be modelled by treating the ion column as an ideal lens with linear focusing force. For an initially round beam the beam transverse size σ_r is then obtained by solving equation 2.46 [77, 79–81]:

$$\frac{d^2\sigma_r(z)}{dz^2} + k^2\sigma_r(z) = \frac{\varepsilon^2}{\sigma_r^3(z)}, \quad k = \frac{\omega_p}{c}\frac{1}{\sqrt{2\gamma}}, \tag{2.46}$$

with ω_p the plasma period, ε the beam emittance, γ the relativistic beam factor and $(2\pi/k)$ the betatron wavelength. The matching condition $d\sigma_r/dz = 0$ yields $\sigma_r^2 = \varepsilon/k$ or

$$\sigma_r = \left(\frac{2\varepsilon_0 m_e c^2}{e^2}\frac{\gamma\varepsilon^2}{n_0}\right)^{1/4}. \tag{2.47}$$

In [77, 78], it has been shown experimentally that a matched beam can be channelled with almost constant transverse size over distances much longer than what one would estimate from its β-value at focus, cf. section 2.2.2.

For most plasma densities of interest, the matched beam size is in the order of a few μm. The requirements on the focusing can be relaxed by adiabatic matching [77]. For an adiabatic change in the focusing force $k^2 \propto n_0$ in the boundary of the plasma density profile, the beam can be matched to the constant density part of the plasma. The required beam parameters can be found by solving equation 2.46 for the peak plasma density with the initial conditions $\sigma_r(z_{peak})^2 = \varepsilon/k(z_{peak})$, $d\sigma_r(z_{peak})/dz = 0$ and then propagating the beam back to where $n_0 \approx 0$.

In a PWFA, the drive beam can lose a big fraction of its energy as it propagates through the plasma. This means that the focusing strength $k \propto 1/\gamma$ changes along z. However, simulations in [77] show that a matched beam remains closely matched even if the beam loses a big fraction of its energy.

2.8.2   Hosing

When an electron beam propagates through an underdense plasma, it is subject to a transverse instability called hosing [82–84]. The instability is caused by the coupling of the beam centroid to the electrons at the edge of the ion channel. It is similar to the transverse two-stream instability occurring for lower driver densities and the beam breakup observed in classical linear accelerators. Similarly, it can lead to a degradation of beam brightness and to total beam disruption. The growth of the instability can limit the useful acceleration length and make it difficult to aim the beam [85].

A more detailed discussion of hosing can be found in appendix D.

2.8.3   Scaling with Plasma Density

At SLAC, the energy of $42\,\text{GeV}$ electrons has been doubled in a plasma cell of $85\,\text{cm}$ [13]. However, the plasma densities n_0 were larger than $2 \times 10^{17}\,\text{cm}^{-3}$. This means that the size of the accelerating structures, on the order of the plasma collision-less skin depth c/ω_p, were smaller than $\approx 20\,\mu\text{m}$. Producing high charge, high quality accelerated bunches in such small scale structures is a challenge, even though no accelerating structure has to be manufactured. In the scope of this thesis, several scalings with plasma density for a beam-driven linear collider operating in the blowout regime have been derived (and published in [86]). They are based on the premise that while very high-gradient acceleration would lead to a minimization of the length of such a collider, beam quality and power requirements may favour operating at lower densities and therefore also lower gradients.

The following scalings are expressed with respect to the plasma density n_e. Assuming that the accelerating gradient scales proportionally to the cold plasma wave breaking field $E_0 = m_e c \omega_{pe}/e \propto n_0^{1/2}$, the plasma length L_p to reach a given final energy thus scales as $n_0^{-1/2}$. Furthermore, we assume that the drive and witness bunch lengths σ_z are a fixed fraction of the plasma skin depth c/ω_p, and therefore also scale as $n_0^{-1/2}$.

In order to minimize energy loss to synchrotron radiation due to betatron envelope oscillation of the bunches along the plasma, the beam size is assumed matched to the plasma's

very strong focusing force, cf. section 2.8.1. In this case, the beam's transverse size remains constant along the plasma,

$$\sigma_r = \left(\frac{2\epsilon_0 m_e c^2}{e^2} \frac{\gamma \epsilon^2}{n_0} \right)^{\frac{1}{4}} \propto n_0^{-\frac{1}{4}}. \tag{2.48}$$

We also assume that we set the bunch densities so that the ratio of the two bunches' density to the plasma density n_b/n_0 is kept constant. To keep up with the above scalings the number of particles per bunch scales as $N_b \propto \sigma_r^2 \sigma_z n_b = cst.$, i.e. the number of particles per bunch is independent from the plasma density. The increase in beam density is negated by the decrease of the bunches' dimensions. Note that due to the different dependence of the bubble size on the plasma density, this is a fundamentally different scaling than the $N \propto n_0^{-1/2}$ dependence found in chapter 4.2.

The matching condition between the plasma focusing force and the beam leads to extremely small transverse beam dimensions. Focusing the beam to the entrance of each plasma section is a challenge that can be relaxed by operating at a lower plasma density. With the normalized emittances typically expected for the ILC ($\epsilon_{xN} = 10^{-5}$, $\epsilon_{yN} = 3 \times 10^{-8}$ m·rad) the transverse sizes matched to a plasma with $n_0 = 10^{16}$ cm^{-3} are $\sigma_{x0} \cong 1\,\mu$m and $\sigma_{y0} \cong 57$ nm. The matched beta function (equal in both planes) is $\beta_{m,\,25GeV} \cong 17$ cm at an initial injection point into the plasma at 25 GeV, and $\beta_{m,\,500GeV} \cong 76$ cm at 500 GeV energy.

Beam Scattering

Beam scattering is slightly different in a PWFA than in a neutral medium. Since the bunch density is chosen to be larger than the plasma density, the witness bunch propagates in a pure ion column. Therefore, as far as scattering is concerned the bunch electrons "collide" with all the ions of the ion column, unlike in the case of a neutral medium in which the collisions are only with single nuclei, or in neutral plasmas where the maximum impact parameter is the Debye length. Therefore, the emittance growth resulting from this extended scattering range must be recalculated and can be expressed in terms of the bunches initial and final relativistic factors γ_{in}, γ_{fin}. For a bunch radius matched to the ion column [81]:

$$\Delta \varepsilon_N = \sqrt{2} r_e S (\sqrt{\gamma_{fin}} - \sqrt{\gamma_{in}}), \tag{2.49}$$

$$S = Q \cdot \ln \left(\frac{r_b}{r_a} \right) + \frac{1.78 Z(Z+1)}{Q} \ln \left(\frac{287}{\sqrt{Z}} \right), \tag{2.50}$$

with r_e the classical electron radius, $Q \cdot e$ the ion charge, $r_b = \sqrt{\frac{n_b}{n_0}} \sigma_r$ the blowout radius, r_a the atomic radius and Z the atomic number. For $Z = 1$, the contribution from the ion column (first term in S) and the neutral vapour (second term in S) are roughly the same. For higher Z the term from the neutral vapour dominates. Emittance growth due to multiple Coulomb scattering is negligible for low Z material but becomes important for higher Z.

Note that an initially matched beam remains matched as long as the emittance growth is small over one betatron wavelength. The emittance growth then only depends on the type of plasma ions (S-term) and the initial and final beam energy. It is essentially independent of the plasma density.

Ion Motion

For the low emittance beams considered for a future collider, the matched bunch radius given by equation 2.48 is very small, in the order of a few μm. The very dense bunches have large space charge fields that can pull the plasma ions toward the beam axis on the time scale of a plasma period , $\omega_{pi}^{-1} \propto n_i^{-\frac{1}{2}} \propto n_0^{-\frac{1}{2}}$. This results in non-linear plasma focusing forces, leading to beam emittance growth. To lowest order, the plasma ions of mass Am_p and ionization state Z execute a harmonic motion towards the axis and their phase advance over one plasma period is given by [87]:

$$\frac{\Delta\phi}{2\pi} = \left(\frac{2\pi Z r_a N_b \sigma_z}{A\epsilon_N}\right)^{1/2} (r_e n_0 \gamma)^{1/4} \qquad (2.51)$$

where r_e and r_a the classical radius of the electron and of the proton, respectively. For ion motion not to be an issue for emittance preservation, the value of $\frac{\Delta\phi}{2\pi}$ must remain $\ll \frac{1}{4}$. Under the assumption of constant beam to plasma density ratio, $\frac{\Delta\phi}{2\pi}$ is independent of n_0. Ion motion can be mitigated by i) Using lower charge or longer bunches than assumed here for the scaling. However, this makes it necessary to reduce the plasma density to still excite plasma wakes efficiently ($\sigma_z \propto \lambda_p \propto n_0^{-1/2}$) and reduces the acceleration gradient ($E_z \propto n_0^{1/2}$). It might also require operating at a higher repetition rate to fulfil the luminosity requirements of a linear collider. ii) Using heavier ion plasmas. This however increases the emittance growth due to scattering, as denoted by equation 2.50. iii) More sophisticated techniques that require either the transverse density shaping of the beam [88] or an adiabatic change of the plasma ion species from heavier to lighter ions [89].

Ion motion can be a major problem for the afterburner concepts discussed in chapter 4.3.2 [87–90].

Beam Head Erosion

It was noted in recent experiments that head erosion of the drive bunch may limit the acceleration length and therefore the energy gain in a single plasma section [13]. This erosion occurs because the head of the drive bunch propagates either in a neutral vapour (field-ionized plasma case) and / or in a neutral plasma without focusing forces (pre-ionized plasma case). Therefore, the point along the bunch where the plasma focusing force counters the natural beam divergence recesses. This effect is significant only when the matched beam beta function $\beta_m = \frac{c\sqrt{2\gamma}}{\omega_{pe}} \propto n_0^{-1/2}$ is shorter than the plasma length L_p. Note that head erosion appears to be an issue for beams with parameters typical of ILC beams matched to meter-long plasma sections with densities in the $10^{16}\,\mathrm{cm}^{-3}$ since their beta function is on the order of $17\,\mathrm{cm}$. However, head erosion is only an issue for the drive bunch that is discarded at the end of each of plasma section. In a multi-stage acceleration scenario the drive bunches only have a $25\,\mathrm{GeV}$ initial energy decreasing to close to zero. Therefore, they need not to be matched to the plasma focusing force. Their larger size will generate extra betatron radiation, but mitigate both the drive bunch head erosion and the effect of plasma ions motion from the drive bunches. In [91], an expression for the head erosion rate in a field ionizing plasma was derived that indicates that for head erosion not to be an issue, the following condition must be satisfied :

$$\frac{1}{2466}\frac{c}{\omega_{pb}}(\mu\mathrm{m})\frac{\sigma_r(\mu\mathrm{m})E_{thresh}(\mathrm{GV/m})}{\frac{N_b}{2\times10^{10}}}\frac{1}{\beta^*} < 1 \qquad (2.52)$$

In this equation ω_{pb} is the beam plasma frequency, σ_r is the matched beam size and $\beta^* = \gamma\sigma_r^2/\epsilon_N$ is the matched beam beta function, and E_{thresh} is the electric field threshold for field ionization of the ambient gas (e.g., $E_{thresh} \cong 6\,\text{GV/m}$ for lithium). This limit scales as $n_0^{-5/4}$.

2.9 Beam Loading

In a particle accelerator, there are several interactions between a bunched particle beam and the waveguide structure. The resulting effects are referred to as beam loading. They can lead to a reduction, redistribution and phase shift of the RF field in the waveguide, excitation of other waveguide modes and various transient phenomena [92]. This directly influences the number of particles that can be accelerated and the efficiency of that acceleration as well as the energy distribution of the accelerated particles. In general, beam loading leads to a reduction of the maximal energy and an increase of energy spread [23]. The maximum charge that can be loaded is given approximately by the number of charged particles required to cancel the wake-field generated by the driver (beam loading limit) [21, 93].

For the nonlinear regime, it was demonstrated in [94] that an optimization of the loaded current can lead to a reduction of the energy spread by suppressing the continuous trapping of background electrons (cf. chapter 2.1.3).

For the linear regime of plasma acceleration, a detailed discussion of beam loading can be found in [23]. A short summary is given below. In particular, the possibility to minimize the energy spread generated during the acceleration process via a shaping of the bunch charge density is discussed. This bunch shaping is assumed for many of the linear collider proposals discussed in chapter 4.

2.9.1 Beam Loading in the Linear Regime

The wake field produced by an arbitrary beam of relativistic particles of charge density $\rho_b(r,\theta,\xi)$ is given by

$$E_z(r,\theta,\xi) = (-2k_p^2)\int_{+\infty}^{\xi} d\xi' \int_0^\infty r'dr' \int_0^{2\pi} d\theta' \rho_b(r',\theta',\xi') \tag{2.53}$$

$$\times K_0(k_p\left|\vec{r}-\vec{r'}\right|)\cos k_p(\xi-\xi'), \tag{2.54}$$

where K_0 is the zeroth-order modified Bessel function and $\xi = z - ct$. When the particle beam and the accelerating wave have nearly uniform transverse profiles and are much larger than c/ω_p, the beam-loading problem is approximately one-dimensional. Then, in one dimension, for an infinitesimally thin sheet of charge per unit area q/A,

$$E_z = (-4\pi q/A)\theta(t - z/c)\cos\omega_p(t - z/c). \tag{2.55}$$

In a cold plasma, the wake function (2.54) is a simple sinusoid, just as is the accelerating wave field:

$$E_z^{wave} = E_0\cos(\omega_p t - k_p z + \phi) = (-4\pi e n_1/k_p)\cos(\omega_p t - k_p z + \phi) \tag{2.56}$$

where $n_1 < n_0$ is the perturbed plasma density and ϕ a constant phase factor. Therefore, one could exactly cancel the accelerating wake field by placing a short ($\ll k_p$) electron beam at a minimum of the accelerating field. Comparison of equations 2.55 and 2.56 yields that the total field ($E^{wave} + E^{beam}$) behind the beam equals zero if $q = -N_0 e$, with the number of electrons N_0 given by

$$N_0 = \frac{E_0}{4\pi e} \cdot A \cong \frac{n_1}{k_p} A. \tag{2.57}$$

Equation (2.57) represents the maximum number of electrons that can be accelerated in an ultrashort, unshaped bunch. Since all of the wave energy is absorbed, this idealized case corresponds to 100% beam-loading efficiency. Unfortunately, in this idealized beam-loading model 100% efficiency is achieved only at the expense of 100% spread in the energy gain of the beam. This is because an electron at the front of this infinitesimally short beam feels the full accelerating field E^{wave}, while the last electron feels the superposed field $E^{wave} + E^{beam} = 0$. Since the reduction in the accelerating field for the last particle is linear in the number N of particles loaded, the fractional energy spread will be

$$\frac{\Delta\gamma_{max} - \Delta\gamma_{min}}{\Delta\gamma_{max}} = \frac{E_i - E_f}{E_i} = \frac{N}{N_0}, \tag{2.58}$$

where $E_{i,f}$ are the field amplitudes in front of and behind the accelerated bunch, and $\gamma_{max,min}$ refer to the maximum and minimum energy gain by a particle in the bunch. On the other hand, the fraction of wave energy absorbed by the particles is $1 - E_f^2/E_i^2$. Since $E_f = E_i(1 - N/N_0)$ the beam-loading efficiency is

$$\eta_b = \frac{N}{N_0}\left(2 - \frac{N}{N_0}\right). \tag{2.59}$$

Equations (2.58) and (2.59) illustrate the trade off between energy spread and efficiency for short, unshaped beams.

Tailoring of Bunch shape

To reduce the energy spread of the beam without lowering the beam loading efficiency, two methods have been suggested. The first possibility is to divide the number of particles N one wants to accelerate into m bunches, positioned at different phases of the accelerating wake. The last bunch is positioned at the phase corresponding to the maximal accelerating field, and each preceding bunch is advanced in phase by one wavelength plus $\delta\phi_m$, so that it feels the same accelerating field E_z. Since there are only N/m particles in each bunch, the energy spread is reduced by a factor of m. (This scheme assumes ultra short bunches.) A more effective way which allows for finite bunch length has been suggested in [95]. In this scheme, the density of the accelerated bunch is ramped down in a way that keeps the superposition E_a of the wake field and field of the bunch constant within the bunch. With this ansatz the optimal bunch shape has been found to be triangular,

$$\rho_b(\xi) = -\frac{k_p E_0}{4\pi}[(k_p \cos k_p \xi_0)\xi + (\sin k_p \xi_0 - k_p \xi_0 \cos k_p \xi_0)] \tag{2.60}$$

with the peak density at the head of the bunch and the bunch starting at $\xi = \xi_0$ ahead of the wave minimum and $-k_p E_0/4\pi e = n_1$ the density perturbation associated with the

wave. The back of the bunch could be truncated at any point to yield an trapezoidal shape. The corresponding peak bunch density, maximum bunch length, accelerating field and the number of particles are

$$\rho_b(\xi_0) = \rho_b^{max} = -en_1 \sin(k_p\xi_0), \tag{2.61}$$

$$l_{max} = (\tan k_p\xi_0)k_p^{-1}, \tag{2.62}$$

$$E_a = E_0 \cos k_p\xi_0, \tag{2.63}$$

$$N = N_0 \frac{\sin^2 k_p\xi_0}{2\cos k_p\xi_0} \tag{2.64}$$

with $N_0 = n_1 A/k_p$ and A as defined in equation 2.57. The beam loading efficiency is then given by

$$1 - E_a^2/(E^{wave})^2 = 1 - \cos^2 k_p\xi_0, \text{ or} \tag{2.65}$$

$$\eta_b = \sin^2 k_p\xi_0. \tag{2.66}$$

Bunches shaped this way suffer no energy spread, but equations 2.62-2.64 show the trade-off between accelerating gradient and efficiency, as illustrated in figure 2.3. For example, if
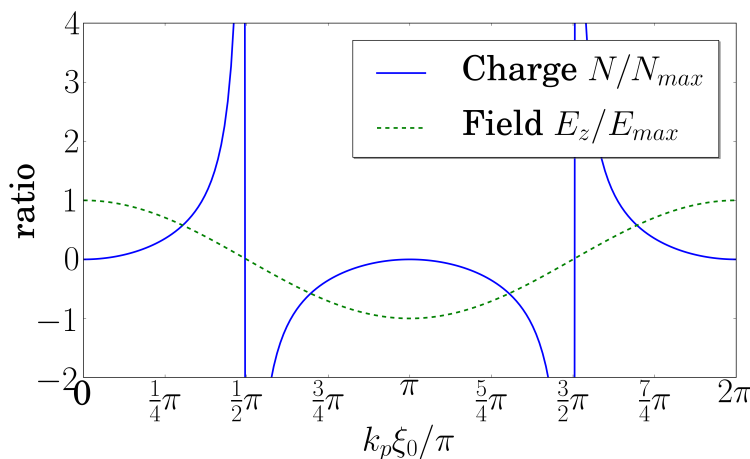
Figure 2.3: Correlation between the maximal number of particles that can be accelerated and the maximal acceleration gradient for a triangular bunch, as given by equations 2.63 and 2.64.

one places the front of a triangular bunch ahead of the wave-field minimum by an amount $\xi_0 = \pi/3k_p$ with $N = 3N_0/4$ particles over a length $\sqrt{3}/k_p$, then the predicted gradient is 50 % of the peak accelerating wave amplitude and the beam-loading efficiency is 75 %, without energy spread. Also, see figure 2.4.

In [95], the following scheme for shaping bunches has been suggested: One starts with a bunch duration of the same order as the fall time needed for the final bunch. A spectrometer provides horizontal momentum separation. Then, both ends of the momentum distribution get cut by collimators. Afterwards, the momentum distribution is transferred back into a time distribution (This requires a correlated energy spread). As similar scheme is used for the wire mesh mask setup described in [96].

Gaussian Bunches

For the bunch shaping described above to work, the bunches have to be shaped and positioned with a accuracy better than k_p^{-1}. Since this may prove to be difficult, Gaussian bunches are investigated. We compare them to a triangular bunch truncated at length $l = l_{max}/2$, thus containing three fourths of the number of particles given in equation 2.64. The Gaussian bunch density is of the form

$$\rho_b(\xi) = (-en_1 \sin k_p\xi_0) \exp[-(\xi - \xi_0 + l/2)^2/2\sigma^2],$$

where $\sigma = 3l/8\sqrt{2\pi}$, so that the total number is that of the half triangle. The resulting total field is shown in figure 2.4 (for $k_p\xi_0 = \pi/3$). For particles within 1σ of the centre, the accelerating field is approximately one third of the wave amplitude and varies by $\sim \pm 10\,\%$. For the same number of particles in an ultrashort bunch (at $\xi_0 = 0$), equation 2.58 predicts an energy spread of $56\,\%$. Thus, a well-placed Gaussian may suffer less energy spread than an ultrashort bunch, but more than the ideally shaped bunch.

Transverse Beam Loading Consideration

The beam loading described above is valid when the beams and the accelerating waves have the same transverse profile and are wide compared to k_p. For beams with arbitrary radius, it can be shown that even if the beam radii differ by orders of magnitude, their radial wake profiles do not. Physically, this means that even very narrow beams can absorb plasma wave energy out to a skin depth k_p.
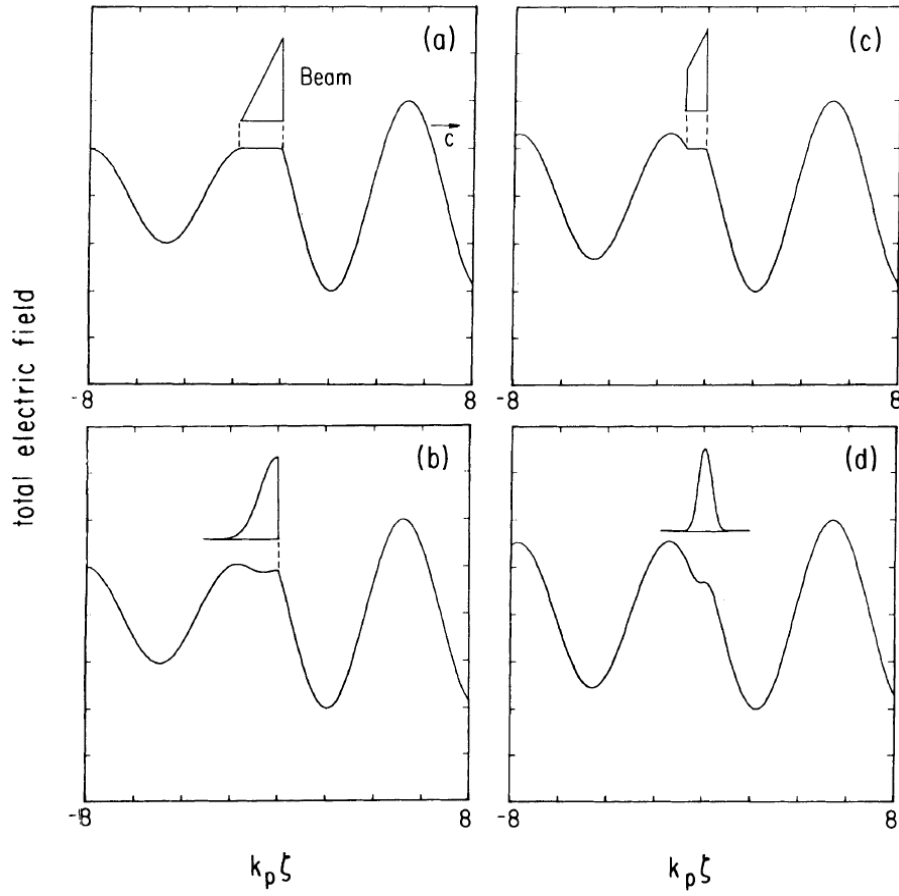
Figure 2.4: Total electric field for various beam shapes: a) triangle (eq. (2.60), $N = 3N_0/4$, $k_p\xi_0 = \pi/3$), b) half Gaussian, same number of particles, c) truncated triangle ($N = 9N_0/16$), and d) Gaussian of same number as c). Figure property of Thomas Katsouleas [23], used with permission.

3. Status of Experimental Studies

This chapter aims to give an overview of the current status of plasma-based acceleration research and high-power laser systems. This is important to give perspective to the studies of high energy lepton colliders discussed in chapter 4, and the study of LWFA as injectors for synchrotron light sources discussed in chapter 5. Particular emphasis is put on the correlation between bunch length and bunch charge, and on the achieved beam quality - both questions critical to the successful operation of an accelerator.

My participation to a laser wakefield acceleration experiment at the Rutherford Appleton Laboratory, Oxfordshire, UK is described in section 3.2.

3.1 Laser Wakefield Acceleration

3.1.1 Achieved Electron Beam Parameters

Laser-driven plasma-based acceleration has first been demonstrated in 1995 [40, 97]. For these experiments, the electron energy spectra still showed an exponential characteristic, with the majority of the electrons at the low energy end of the spectrum and a few electrons reaching a few tens of MeV. This changed dramatically in 2004, when three groups independently achieved the acceleration of high quality electron beams. For these experiments, a charge of approximately $100\,\mathrm{pC}$ was accelerated to a mean energy of approximately $100\,\mathrm{MeV}$, with a small energy spread of a few percent and a low divergence of a few milliradians [42–44]. In 2006, high quality electron bunches of up to $1\,\mathrm{GeV}$ mean energy have been demonstrated experimentally [10]. Following experiments demonstrated emittances on the $1\,\pi\mathrm{mm}$-mrad level [98, 99], $1\,\mathrm{fs}$ pulse duration [100], energy spreads on the $1\,\%$ level [99, 101], and shot to shot stability of the central energy of $3\,\%$ [99, 102].

In 2010, $1.45\,\mathrm{GeV}$ beam energy has been demonstrated by [103], but with a charge of less than $4\,\mathrm{pC}$ and an efficiency of less than $1\,\%$. In 2011, $1.8\,\mathrm{GeV}$ maximal beam energy have been reported by [104], with the same exponential energy distribution.
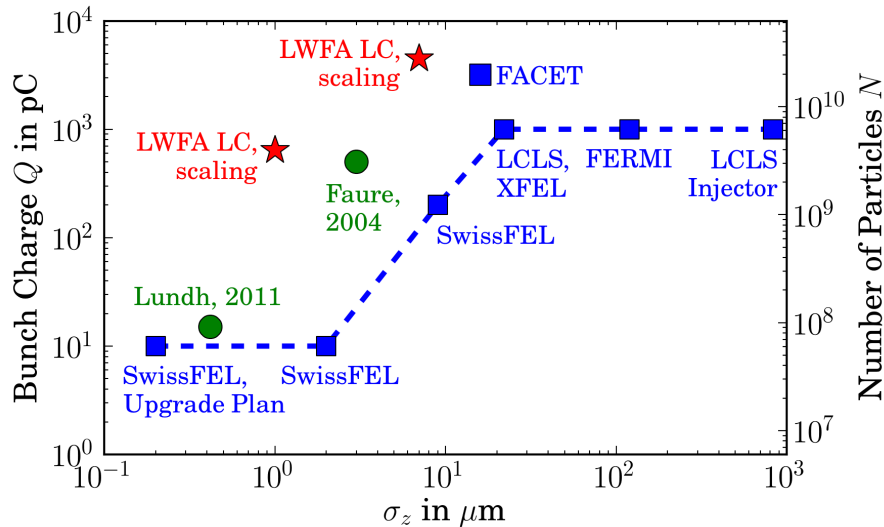
Figure 3.1: Comparison of bunch charge vs. bunch length for conventional and laser-based accelerators. The connected blue squares represent design parameters of exemplary running or near future FEL-facilities [106, 108, 110, 111]. The different bunch lengths for 1 nC are for different beam energies, ranging from 150 MeV for the LCLS injector over about 1.5 GeV for FERMI to several GeV for LCLS and XFEL. See tables 3.2 and 5.1 for more information and numerical values. The disconnected blue square represents FACET. Here, a higher charge for a shorter bunch length has been achieved, but for a much higher beam energy of 23 GeV [109]. The green circles represent parameters achieved with LWFA by Lundh et al. [100] and Faure et al. [42]. Note that these parameters were achieved for a much lower energy on the order of $\mathcal{O}(100\,\text{MeV})$, and with a much larger energy spread and much larger fluctuations in mean energy and charge (From [100]: "we measured: peak energy $84 \pm 21\,\text{MeV}$, energy spread $21 \pm 17\,\text{MeV}$ (FWHM), peak charge $15 \pm 7\,\text{pC}$"). Finally, the red stars represent parameters calculated in [11, 21] as parameters for linear colliders operating at plasma densities of $n_0 = 10^{17}\,\text{cm}^{-3}$ (lower charge) and $n_0 = 2 \cdot 10^{15}\,\text{cm}^{-3}$ (higher charge) respectively. Also published in [112].

External injection has been demonstrated in [105]. However, the electron bunches used there were a few tens of plasma wavelengths long, resulting in a continuous energy spectrum up to some maximum energy.

An important question regarding the use of LWFA as injectors is the amount of charge stored for a given bunch length. An overview over achieved and desired bunch parameters is given in tables 3.1 and 3.2, and is illustrated in figure 3.1.

Bunch Shaping

As described in detail in chapter 2.9.1, the proper shaping of the longitudinal charge density along the bunch can be used to reduce the energy spread acquired during the acceleration process. This theoretically simple method is e.g. employed in several of the linear collider proposals discussed in chapters 4. However, to the best of the authors knowledge, bunch shaping has not been demonstrated for bunches of the $\sigma_z \approx 1\,\mu$m length scale customary for LWFA.

Year	2004	2006	2008	2010	2011
Facility	LOA	LBNL	MPQ	SUPA	LOA
Plasma density [$10^{18}\,\mathrm{cm}^{-3}$]	6	4.3	7.3	50	10
Electron mean energy [MeV]	170	1000	198	137	84
Mean energy fluctuation [%]	5	7	6 [b)]	3	21
Energy spread [%]	10	2.5	6.1	<1 [c)]	11
Bunch charge [pC]	500	30	10	2-10	15
Charge fluctuation [pC]	200	[a)]	4 [b)]		7
Bunch length [fs]	<21[c)]			0.8 [d)]	1.5
Bunch length [μm]	< 9			0.25[d)]	0.5
Laser pulse energy [J]	1.0	1.7	0.85	0.9	1.0
Laser pulse length [fs]	13	16	18	15	13
Laser pulse length [μm]	4	5	5	4	4
Laser peak power [TW]	33	40	20	26	33
Efficiency [%]	10	2	0.2	0.03-0.2	0.1

Table 3.1: Achieved beam parameters for different experiments, achieved at Laboratoire d'Optique Appliquée (LOA), France [42, 100]; Lawrence Berkeley National Laboratory (LBNL), USA [10]; Max-Planck-Institut für Quantenoptic, Germany [102]; Scottish Universities Physics Alliance (SUPA), Scotland [99]. Not all information was available for all experiments. If possible, missing values have been calculated from the ones given. If applicable, values are given in RMS. The efficiency is given for the energy transfer from the laser beam to the quasi monoenergetic electron beam. Much of the mean energy fluctuations is related to fluctuations in the laser pulse energy. [a)]For a lower beam energy of $0.5\,\mathrm{GeV}$, enough statistics was obtained to calculate a fluctuation of charge of $\pm 34\,\%$. [b)]For a lower plasma density of $n_0 \approx 6.8 \cdot 10^{18}\,\mathrm{cm}^{-3}$, an unprecedented shot-to-shot stability of $2.5\,\%$ fluctuation in mean energy and $16\,\%$ in charge was obtained. This came at the expense of a reduced peak charge of $7\pm 3\,\mathrm{pC}$, a reduced electron mean energy of $122 \pm 3\,\mathrm{MeV}$ and a reduction in electron injection probability from $80\,\%$ to $71\,\%$, indicating the laser pulse was just above the injection threshold. [c)]Resolution limited. [d)]Bunch length from simulations, not measured. An increase in relative energy spread for lower mean energies indicates a fixed absolute energy spread of about $0.6\,\mathrm{MeV}$ for the experimental conditions. A normalized emittance $\varepsilon_N \sim 1\pi\,\mathrm{mm}\cdot\mathrm{mrad}$ has bean measured (resolution limited, the inferred normalized emittance is about half this value).

Length [μm]	Charge [pC]	Status	Comment
0.4	15	achieved	LWFA, Lundh
3	500	achieved	LWFA, Faure
20	3500	achieved	FACET
22	1000	planned	LCLS
830	1000	planned	LCLS
0.2	10	planned	SwissFEL
2	10	planned	SwissFEL
9	200	planned	SwissFEL
1	640	scaling	ICFA BDN
7	4500	scaling	ICFA BDN

Table 3.2: Comparison of bunch parameters achieved, planned and required by the scalings in [11, 21]. The parameters for Laser Wakefield Acceleration (LWFA) are taken from [42, 100]. The parameters for the Linac Coherent Light Source (LCLS) are design goals before the first linac and after the last bunch compressor respectively [106]. Currently, LCLS has achieved a bunch charge of ∼250 pC at a final bunch length of 8-10 μm [107]. The parameters for the Swiss Free Electron Laser (SwissFEL) are for the long and short pulse operation and for the considered upgrade respectively, all at a beam energy of 5.8 GeV [108]. The parameters for FACET, the Facility for Advanced Accelerator Experimental Tests at SLAC are for an energy of 23 GeV [109]. The parameters required in [11, 21] are for plasma densities $n_0 = 10^{17}\,\mathrm{cm}^{-3}$ and $n_0 = 2 \cdot 10^{15}\,\mathrm{cm}^{-3}$ respectively. See figure 3.1 for a graphical comparison.

3.1.2 Status of High Power Laser Systems

Pulse Energy and Repetition Rate

An overview over the current status of existing and planned high power laser systems is given. Table 3.3 lists the key top level parameters of some exemplary laser systems. Currently, BELLA is the strongest laser facility dedicated to LWFA research, and other planned and existing facilities working on LWFA operate with similar parameter sets as e.g. SCAPA and LOA.

Significantly higher pulse energies have been achieved in facilities conducting research for laser-driven fusion. To date, the highest laser pulse energy was reached at the National Ignition Facility (NIF) [113] with 2.03 MJ in the ultra violet (UV) by frequency tripling a 3.6 MJ infrared laser (1050 nm). With a pulse duration of 23 ns, this corresponds to a peak power of 411 TW in the UV [114]. Allowing sufficient cool down time for the components to avoid damage results in a repetition rate of about 1 shot per day [115].

Future large scale facilities aim at even higher peak powers using shorter laser pulses with lower stored energy and higher repetition rate. Example parameters for the funded Extreme Light Infrastructure (ELI) are given in table 3.4 [116, 117].

Experiment	PHELIX	Mercury	BELLA	SCAPA	LOA	LOA
Pulse energy U_L [J]	1e3	61*	40	5-7	2.5	9e-3
Pulse length τ_L [fs]	20e6	15e6*	30-200	25-30	35	38
Peak power P_{peak} [TW]		*	110 - 630	250	100	
Repetition rate f [Hz]	185e-6	10	1	5	10	1e3
Average power P_{avg} [W]	0.2	600	40	25-35	25	9
Wavelength λ [nm]	1054	1047	800		810	810

Table 3.3: Overview over the laser parameters of some exemplary experimental facilities. All the facilities mentioned above are currently operational or in commissioning. PHELIX - Petawatt High Energy Laser for Heavy Ion Experiments, Germany, in operation [118, 119]; Mercury, USA, in operation [120]; BELLA - BErkeley Lab Laser Accelerator, USA, in operation [121]; SCAPA - Scottish Centre for the Application of Plasma-based Accelerators, Scotland, in commission [122]; LOA - Laboratoire d'Optique Appliquée, two of the available experimental stations, France, in operation [123]. If possible, values not found in the references have been calculated using the equations given in chapter 2.4.
*Frequency doubling and compression to 15 fs pulse length are a future plan, resulting in 1.4 PW pulse power at 524 nm. The design goal of Mercury is to demonstrate 100 J at 10 Hz.

High-repetition ultrahigh-energy diode-pumped solid-state lasers and other techniques as commercial drivers for fusion are actively developed, currently reaching about 100 J at 10 Hz [124]. A conceptual design of a 100 kJ, 100 Hz facility named GENBU (Generation of ENergetic Beam Ultimate) has been developed [124, 125]. The proposed High Power laser Energy Research facility (HiPER) aims at 200 kJ, 5 ns, 150 PW pulses at a repetition rate of up to 1 Hz [126, 127].

Diode-pumped optical fibres are actively researched as gain medium within ICAN, the International Coherent Amplification Network [128]. They hold the promise of very high

Pulse energy U_L [J]	9200	290	9	0.9
Pulse length τ_L [fs]	368	116	37	11.6
Peak power P_{peak} [TW]	10000	1000	100	10
Repetition rate f [Hz]	0.01	10	1000	1000
Average power P_{avg} [W]	92	2900	9000	900
Spot radius at focus $r_L[\mu\mathrm{m}]$	110	35	11	3.5

Table 3.4: Example laser parameters suggested for the planned ELI facility, extracted from table 6.8 in [117]. Note that these parameters are challenging long term goals and will not be available from the start (Cf. table 6.3, same reference).

efficiency of up to 50 % wall-plug to optical and of very high repetition rates in the order of 10 kHz [128, 129]. They have the additional benefit of being actively developed for the telecommunication industry, which makes them easy to mass produce at low cost. Example parameters for a possible 10 J demonstration module are given in table 3.5. Higher output energies could be reached by using more fibres, which makes this technique much easier to scale as current day bulk lasers, which require larger custom-build crystals.

The correlation between achieved laser pulse energies and repetition rate is illustrated in figure 3.2.

Pulse Energy	Repetition Rate	Average Power	Efficiency
> 10 J	> 1 kHz	> 10 kW	> 20 %

Table 3.5: Top level parameters for the proposed 10 J demonstration stage for a fibre based high power laser [129]. It is foreseeable to realize such a demonstrator by the end of the decade [130]. For a later stage, repetition rates in the order of 10 kHz are foreseeable, as well as a significant increase in beam energy by using more fibres.

Wall-plug Efficiency

The wall-plug efficiency of a laser system is its total electrical to optical efficiency. In principle, it should include the power losses on the power supplies and the power required for cooling, which can be significant for high power systems. However, it is common to calculate the wall-plug efficiency based on the power delivered to the laser diodes, neglecting the before mentioned losses [33].

Using this common definition, many diode-pumped laser systems today reach efficiencies in the order of 25 %, and it is to be expected that their efficiency will further increase within the next years [33]. As already mentioned in the previous section, diode-pumped optical fibres are actively researched as gain medium within ICAN, the International Coherent Amplification Network [128]. It is foreseeable that High-Gain fibre amplifiers will make about 50 % total plug-to-optical output efficiency reachable [129]. Furthermore, optical fibres have a very good surface to volume ratio, allowing for efficient cooling.

Currently, many LWFA experiments still rely on argon-ion laser systems, which have an efficiency of about 1 %. When pumped by argon-ion lasers, titanium-sapphire laser feature an even lower efficiency.
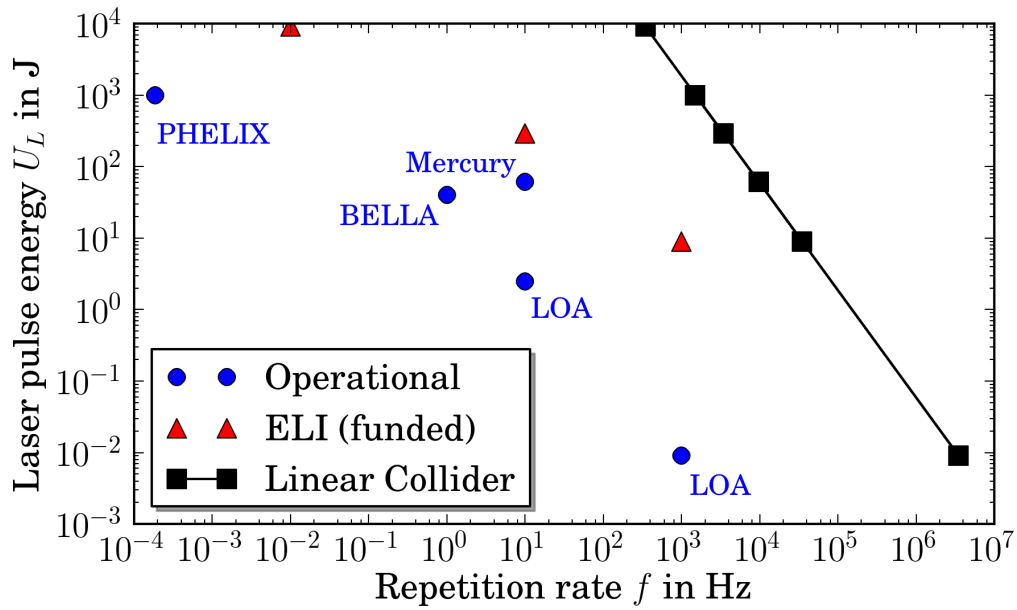
Figure 3.2: Laser pulse energy versus repetition rate for exemplary high power laser facilities [117–120, 123], cf. tables 3.3 and 3.4. For each operational facility, there is a marker which denotes the needed repetition rate for a linear collider operating at the corresponding pulse energy (connected black squares). Values were derived based on the scalings and example parameters in [21]. (Cf. tables 4.1 and 4.2 in chapter 4.2, page 52. In particular: $E_{CM} = 1\,\text{TeV}$, $\mathcal{L} = 2 \cdot 10^{34}\,\text{cm}^{-2}\text{s}^{-1}$, $\sigma_x^* = \sigma_y^* = 10\,\text{nm}$.) Also, cf. figure 5.1, page 78. Also published in [112].

3.1.3   Conversion Efficiencies

One assumes an efficiency from laser to electron beam of about 20 % [11, 23, 128], resulting from an efficiency of about 50 % from laser to plasma-wake and 40 % for plasma-wake to beam (cf. chapter 2.1.2.3 in [11]).

In [10], approximately 30 pC of charge have been accelerated to 1 GeV using a 40 TW, 40 fs laser pulse to drive a plasma wake in the bubble regime. This results in a laser to e-beam transfer efficiency of about 2 %. Similar efficiencies can be calculated for the parameters given in [98]. Note however, that the interest here was to demonstrate maximum acceleration, not the highest possible beam loading efficiency. Depending on the applied energy cut, a similar efficiency has been reached in simulations by Oliver Jansen, cf. chapter 5.2. In [75], based on analytic estimates backed by simulations, the conversion efficiency from laser energy to quasi mono-energetic electrons has been found to be about 20 % in the bubble regime.

The total efficiency of wall-plug to e-beam is given by the product of the laser to e-beam efficiency discussed here and the wall-plug to laser efficiency discussed in chapter 3.1.2. If a 50 % wall plug to optical conversion efficiency can be achieved, this would result in a wall plug to beam efficiency of about 10 %, comparable to the efficiency of the CLIC / ILC main linacs [11, 93, 128]. As mentioned in the previous section, the wall plug to optical conversion efficiency of the titanium-sapphire laser systems currently used is in the sub percent range.

3.2   Participation to LWFA Experiment

To get some hands-on experience regarding laser wakefield acceleration, I participated in a LWFA experiment at the Astra Gemini laser at the Central Laser Facility at Rutherford Appleton Laboratory (RAL), Oxfordshire, UK. Gemini is capable of delivering 15 J, 30 fs pulses at a rate of $^1/_{20}$ Hz [131]. Fig. 3.3 gives an impression about the size of the laser system and the experiment.

To give a feeling about the produced beams, figures 3.4 and 3.5 show measurement results obtained with the electron energy spectrometer and the beam profile monitor. It is important to point out that these measurements were taken during parameter scans, it was *not* their aim to demonstrate reproducibility. Due to the positioning of the screens, they could not be taken simultaneously.
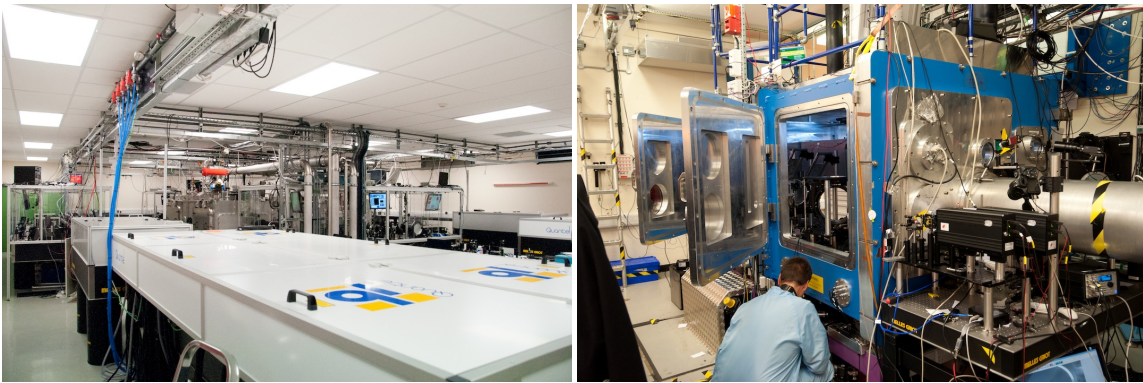
Figure 3.3: Astra laser at the Central Laser Facility at Rutherford Appleton Laboratory, Oxfordshire, UK.
Left: Laser area. The amplifiers are housed in the white boxes at the sides of the room, the pulse compressor is situated in the metal tank in the centre of the room.
Right: Target area. The laser pulses come in from the compressor chamber in the room above through the black metal pipes. The focussing mirror for the drive pulse is situated at the end of the large pipe to the right, approximately 3 m from its focal point.

3.2.1   Beam Position Monitor Measurements

During the last years, LWFA have seen tremendous progress in terms of beam quality and reproducibility. To develop them further towards practical applications, non-invasive diagnostics become a necessity. An obvious candidate are so called Beam Position Monitors (BPMs), which have been routinely used in conventional accelerators for decades. The usability of cavity-based BPMs has already been demonstrated in [134]. In the experiment at the Astra Gemini Laser, it was my aim to demonstrated the possibility of using a conventional pickup BPM.

Experimental Setup

Due to the size of the BPM used ($\sim 250 \times 320 \times 320$ mm, 60 mm inner beam pipe diameter), it was positioned behind the main chamber depicted in figure 3.3, centred around the laser propagation axis. The setup is illustrated in figure 3.6.
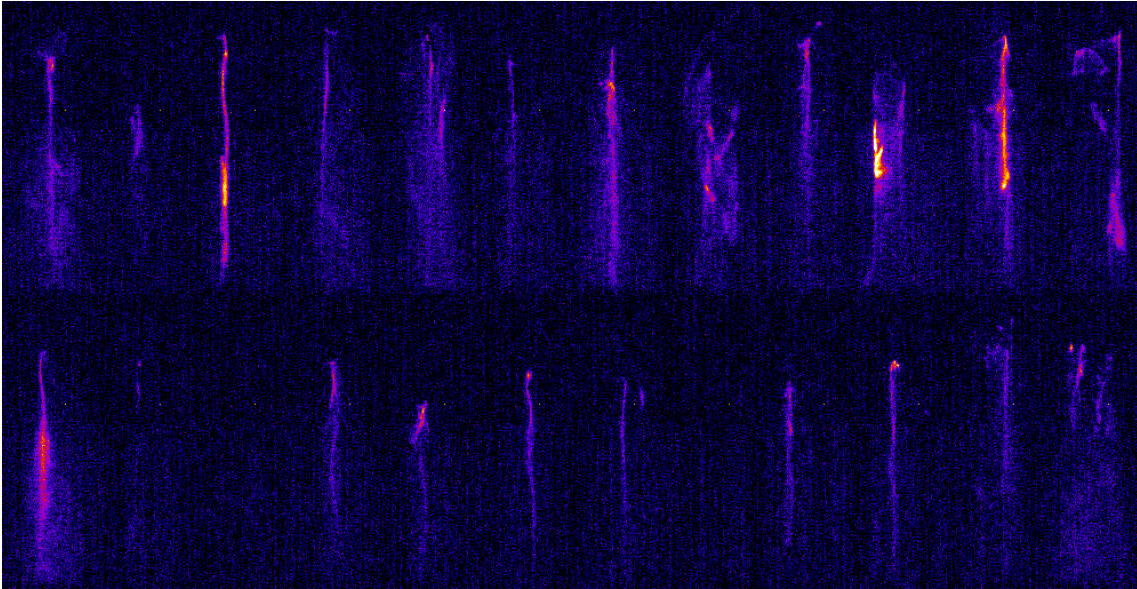
Figure 3.4: 24 consecutive measurements with the electron spectrometer, displayed in 2 rows. The horizontal axis gives information about the transverse properties of the beam, the vertical axis corresponds to the energy from about 0 to 800 MeV, with higher energies towards the top of the page. The colour code gives the intensity, with brighter colour corresponding to higher intensity. Data property of Jason Cole et al. [132].
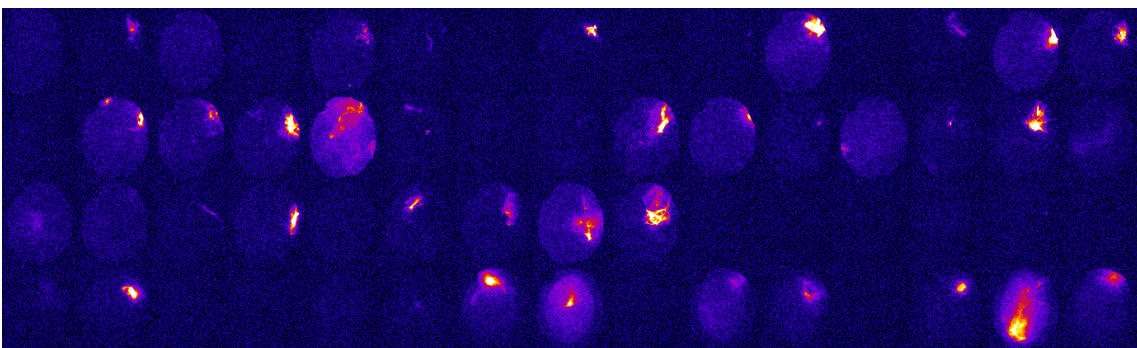
Figure 3.5: 60 consecutive measurements with the beam profile monitor, displayed in 4 rows. The screen is 3 inch in diameter, displaying both position and size of the electron beam. The color code gives the intensity, with brighter colour corresponding to higher intensity. Data property of Jonathan Wood et al. [133].
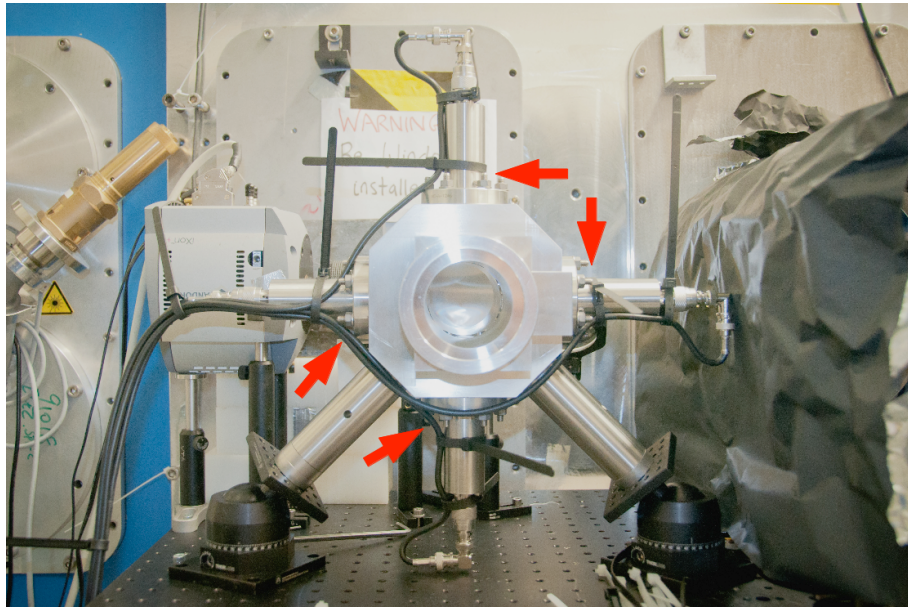
Figure 3.6: Photo of the in-air BPM setup, downstream of the main chamber. Arrows highlight the 4 pickup buttons, located around the central beam pipe.

The working principle of a BPM requires the electron bunch to pass trough it. For our given spacial constraints, this made its use mutually exclusive with two of the main diagnostics: The electron energy spectrometer, which measures the energy depended deflection of the witness beam in a magnetic field; and the X-ray camera, which could have been damaged by the impacting electrons[1]. For a future experiment, the installation of a smaller BPM inside the target chamber seems feasible, allowing operation in parallel with the other diagnostics. A detailed description of the BPM used can be found in [137].

Operation both in air and in vacuum has been tested. Both gas jets and gas cells have been used as target to generate the plasma and in turn to produce the electron beam (For a detailed description of the trapping of plasma electrons in the blowout regime, cf. e.g. [20]). The distance from the target to the sensors (centre of BPM) was approximately 3 m, depending on the target and setup used.

The 4 pickup sensors (referred to as buttons) of the BPM were read out via a 2.5 GHz oscilloscope, triggered by its own signal. The difference in induced voltage between the two opposing buttons gives information about the position of the bunch relative to the centre of the BPM. I compared the BPM measurements results to measurements using a beam profile monitor (Lanex screen) inside the target chamber.

---

[1] As illustrated in figure 2.1, page 7, the plasma electron density modulation due to the laser pulse does not only result in the strong longitudinal field used to accelerate the witness bunch. It also results in strong transverse field, focussing the beam. In turn, the beam undergoes so-called betatron oscillations, comparable to the focusing with quadrupole magnets described in chapter 2.2.2, page 8. This transverse acceleration of the witness bunch electrons leads to the emission of synchrotron radiation, as described in more detail e.g. in [135, 136]. This radiation, with typical photon energies in the keV range, is emitted in parallel with the propagation direction of the driving laser pulse and can be used to diagnose the acceleration process. However, the camera used to detect the radiation could be damaged by impacting electrons. Therefore, the witness bunch has to be deflected off the laser propagation axis with a dipole magnet.

Results

Figure 3.7 shows example measurements. The BPM signal can be clearly distinguished from the background noise. The position measurements are in good qualitative agreement with the beam profile monitor measurements. They also show the expected signal dependence on the bunch charge.
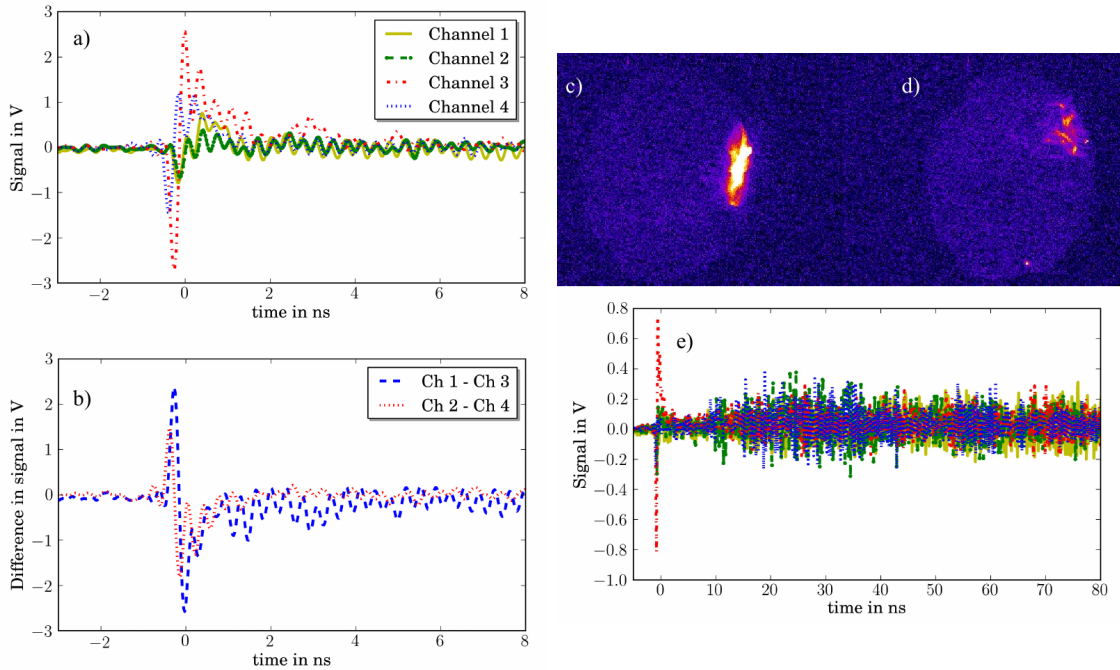
Figure 3.7: a) Signal of the 4 BPM channels with 2.5 ns/div horizontal and 1 V/div resolution (2.5 GHz sampling, 50 Ω termination).
b) Difference in signal for the horizontal (odd) and vertical (even) channels, showing that the centroid of the electron bunch passed the BPM in the upper right quadrant.
c) Corresponding beam profile monitor measurement. Brighter colour corresponds to higher beam intensity.
d) Beam profile measurement for a different shot, same monitor settings as in c).
e) BPM signal corresponding to d), with 10 ns/div horizontal and 200 mV/div vertical resolution. Channels are the same as in a). The initial signal can be clearly distinguished from the following noise. Also, note the lower voltage due to the lower bunch charge visible in d).

Discussion

A good qualitative agreement with the beam profile measurements has been observed. However, due to low statistics, the determination of the achievable resolution is left to a future experiment.

If calibrated, the sum signal of the 4 BPM buttons can give the charges of the bunch passing through. In our case, the electron bunch repeatedly scraped the mounting of the Lanex screen and possibly the vacuum window of the chamber. We have therefore not performed this calibration. It is worth pointing out that in contrast to a beam profile screen, a BPM only gives information of the centroid position of the electron bunch, it does not provide information about the spacial distribution.

Conceptually, BPMs can also be used to measure long (nanosecond) bunch lengths. Due to the cutoff frequencies of the BPM and the resolution of the oscilloscope, this is currently not possibly for the femtosecond bunch lengths customary for LWFA bunches.

For a LWFA providing beams for applications, beam transport in vacuum will be essential to avoid deterioration of beam quality due to scattering. For our proof of principle experiment, operation in air proved useful, as it allowed us to exchange the BPM and the different X-ray cameras without the need to vent and re-evacuate the target chamber, a process taking over an hour. The BPM was also operated in an in-vacuum setup by connecting it to the target chamber via a beam pipe. A significant change in signal characteristic compared to the in-air setup was not noticeable.

The observed signal of a prominent peak with subsequent ringing fits very well with the expectations. Since a different type of BPM was used, the signal characteristic is different from the one reported in [134] (cf. Figure 3 therein).

3.3 Plasma Wakefield Acceleration

So far, beam-driven acceleration has only been studied in experiments at SLAC, which culminated in the energy doubling of a small fraction of the initial 42 GeV electron beam [13]. For the coming years, PWFA experiments are planed at several facilities, cf. e.g. [109, 138, 139].

For the PWFA case with shaped bunches, an energy conversion efficiency of 51 % from drive to witness beam has been achieved in simulations [140]. For acceleration in the linear regime, the beam loading efficiency has been studied theoretically in [23], cf. chapter 2.9.1. Here, a beam loading efficiency of about 20 % is estimated. This is much higher than what has been achieved in the experiments at SLAC. As for the laser driven case, the interest there was to demonstrate maximum acceleration, not the highest possible beam loading efficiency possible.

4. Study of High Energy Lepton Colliders

A high luminosity lepton collider is highly supported by the physics community to complement the Large Hadron Collider (LHC). This means accelerating electrons and positrons to TeV energies. Since the energy lost to the emission of synchrotron radiation during one turn in a storage ring is proportional to γ^4/ρ [141], going to a higher Lorentz factor γ means either increasing the radius ρ or losing more and more energy to synchrotron radiation. Therefore, for the high energies envisaged, it is more efficient to build a linear collider (LC).

In the following chapter, some key requirements and LC schemes shall be discussed. Section 4.1 gives an overview over the technology independent constraints for a linear collider. Different collider proposals found in the literature are discussed in sections 4.2 to 4.6. Based on these findings, I have developed several scenarios for a collider capable of producing the recently discovered Higgs boson with a mass of approximately $125\,\mathrm{GeV}/c^2$ [16, 17]. They are introduced and discussed in section 4.7.

4.1   Constraints

Before going into the different possible linear collider schemes, some constraints shall be introduced first. Whilst the underlying physics leading to said constraints is independent of the acceleration method used, the results depend strongly on the chosen parameters; as will be illustrated in detail in chapters 4.7.3 and 4.7.4, pages 62 and 65 respectively. In particular, for a bunch length determined by the acceleration process, the luminosity requirements discussed in section 4.1.1 will result in certain conditions for the bunch charge density. As will be explained in section 4.1.2, this can result in a drastically different behaviour at the interaction point. The generation of so called Beamstrahlung can lead to severe background signal in the detector system and therefore limit the parameter range acceptable for the acceleration process.

4.1.1   Energy and Luminosity

All currently discussed collider schemes estimate the centre of mass energy to be interesting from a particle physics point of view to be between 0.5 and 3 TeV, with the exact energy to be defined depending on the findings of the LHC [5, 6, 11, 15, 21, 64, 65, 71, 93, 142–156]. The second key figure which is independent of the acceleration scheme is the luminosity, which gives a measure of the possible interactions per time interval. Assuming the same RMS beam size $\sigma^*_{x/y}$ at the interaction point (IP) and same particle number N for both beams, the luminosity $\mathcal{L}$ is given by [64]

$$\mathcal{L} = \frac{fN^2}{4\pi\sigma^*_x\sigma^*_y},\tag{4.1}$$

with f the collision frequency. For a fixed particle energy E_b, this can be rewritten in terms of power per beam $P_b = NE_bf$ as

$$\mathcal{L} = \frac{P_b}{4\pi E_b}\frac{N}{\sigma^*_x\sigma^*_y},\tag{4.2}$$

illustrating that the luminosity is determined by the product of the beam power and the transverse beam density. As most cross sections for electron-positron collisions fall as $1/E^2$, the luminosity has to fulfill the following scaling to provide sufficient data rates for the expected physics processes [64]:

$$\mathcal{L}[10^{34}\,\mathrm{cm}^{-2}\mathrm{s}^{-1}] \approx (E[\mathrm{TeV}])^2.\tag{4.3}$$

As illustrated by equation (4.2), with no change in transverse density, increasing the luminosity by a factor of 10 means increasing the beam power by the same amount. Current day collider designs have AC wall plug powers in the few hundred MW [5, 6, 21, 64, 65] with already relatively efficient energy conversion from wall plug to beam power. As wall plug power requirements in the GW range make the machine prohibitively expensive to operate, the only practical way to increase luminosity is to increase the beam density at the IP. However, limitations arise from [64]: i)the performance of the injectors, determining the initial emittance of the beams; ii) emittance growth in the main linacs; iii) the final focus optics; and iv) beam-beam interactions at the IP.

4.1.2 Beam-Beam Interaction

Beam disruption

At the interaction point (IP), the bunches feel an additional focusing force due to the interaction with the other beam. This leads to increase of the beam density and is generally a beneficial effect. However, it can lead to instabilities and make the luminosity very sensitive to offsets between the colliding bunches [64].

Beamstrahlung

Beam-beam collisions lead to the emission of radiation, the so called beamstrahlung. It has several deleterious effects [64, 157]:

- The emitted photons can enter the detector, increasing the background which can interfere with the detection of physics processes.

- The energy loss of the electrons / positrons during the radiation process increases the energy spread. For physics processes where a precise knowledge of the initial state is required, this can be a serious issue. Also, for processes at the maximal energy reach of the collider, a significant energy loss due to beamstrahlung can reduce the effective luminosity.

- For very large beamstrahlung parameters, it can lead to depolarization of the colliding beams in the order of a few percent.

As the amount of beamstrahlung increases with increased beam density, this can limit the maximum beam density. The features of beamstrahlung radiation can be expressed in terms of the (average) beamstrahlung parameter [64, 157, 158]

$$\Upsilon = \frac{2\hbar\omega_c}{3E_b} \cong \frac{5}{6} \frac{r_e^2}{\alpha} \frac{\gamma}{\sigma_z} \frac{N}{\sigma_x^* + \sigma_y^*}, \tag{4.4}$$

with $\hbar\omega_c$ the critical energy of the beamstrahlung photon spectrum, $\alpha = \frac{e^2}{4\pi\varepsilon_0 \; \hbar c}$ the fine-structure constant and $r_e = \frac{1}{4\pi\varepsilon_0} \frac{e^2}{m_e c^2}$ the classical electron radius. For collisions of Gaussian beams, the average number of beamstrahlung Photons emitted per initial particle is

$$n_\gamma \cong \frac{12\alpha^2\sigma_z}{5r_e\gamma} \frac{\Upsilon}{\sqrt{1 + \Upsilon^{2/3}}}, \tag{4.5}$$

and the average energy loss is

$$\delta_B \equiv \langle \frac{-\Delta E}{E} \rangle \cong \frac{5}{4} \frac{\alpha^2\sigma_z}{r_e\gamma} \frac{\Upsilon^2}{[1 + (1.5 \cdot \Upsilon)^{2/3}]^2}. \tag{4.6}$$

The average Photon energy is given by [157]

$$\frac{\langle\omega\rangle}{E} \approx \frac{4\sqrt{3}}{15}\Upsilon \frac{\sqrt{1 + \Upsilon^{2/3}}}{\left[1 + (1.5 \cdot \Upsilon)^{2/3}\right]^2} = \begin{cases} 0.46\Upsilon & (\Upsilon \to 0), \\ 0.25 & (\Upsilon \to \infty) \end{cases} \tag{4.7}$$

and remains finite at about a quarter of the energy of the initial particle in the limit $\Upsilon \to \infty$. In practice, background becomes excessive if $n_\gamma > 1$ and a final state energy spread of more than a few tens of percent is unacceptable for many physics processes [64].

For a fixed Υ, one could maximize luminosity by making both σ_x and σ_y as small as possible. For particle sources based on damping rings, it is normally not possible to reduce both dimensions simultaneously. The highest luminosity is then achieved with so called flat beams with $\sigma_y^* \ll \sigma_x^*$, which will be assumed for the remainder of this discussion. One can distinguish two regimes, the classical low beamstrahlung regime with $\Upsilon \ll 1$ and the quantum beamstrahlung regime with $\Upsilon \gg 1$. For collider designs operating in the classical regime, one can rewrite n_γ and δ_B as [64]

$$n_\gamma \cong \frac{12\alpha^2\sigma_z}{5r_e\gamma}\Upsilon \cong 2\alpha r_e \frac{N}{\sigma_x^*},$$

$$\delta_B \cong \frac{5}{4}\frac{\alpha^2\sigma_z\Upsilon^2}{r_e\gamma} \cong \frac{125r_e^3}{144}\frac{\gamma N^2}{\sigma_z(\sigma_x^*)^2}$$

This allows us to write the luminosity in terms of n_γ and δ_B by substituting N:

$$\frac{\mathcal{L}}{P_b} \cong \frac{1}{8\pi r_e\alpha}\frac{n_\gamma}{E_b\sigma_y^*} \cong \frac{3}{5\sqrt{5}\pi r_e^{3/2}}\frac{\sqrt{\delta_B\sigma_z}}{E_b\sigma_y^*\sqrt{\gamma}} \tag{4.8}$$

The luminosity per unit beam power is proportional to the number of beamstrahlung photons n_γ. For n_γ and E_b fixed, it can only be increased by decreasing the vertical beam size at the IP. It is also proportional to the root of the beamstrahlung energy spread δ_B, and for δ_B and E_b fixed, can be increased by decreasing the vertical beam size at the IP and / or by increasing the bunch length σ_z. In the low beamstrahlung regime, it is therefore favourable to operate with longer bunches.

For $\Upsilon \gg 1$, one can rewrite n_γ and δ_B as [64]:

$$n_\gamma \cong \frac{12\alpha^2\sigma_z}{5r_e\gamma}\Upsilon^{2/3} \cong 2\alpha\left(\frac{6\alpha r_e}{5}\right)^{1/3}\frac{1}{\gamma^{1/3}}\left(\frac{N\sqrt{\sigma_z}}{\sigma_x^*}\right)^{2/3},$$

$$\delta_B \cong \frac{5}{3^{4/3}\cdot 2^{2/3}}\frac{\alpha^2\sigma_z\Upsilon^{2/3}}{r_e\gamma} = \frac{\alpha}{18}\left(\frac{5^5\alpha r_e}{2}\right)^{1/3}\frac{1}{\gamma^{1/3}}\left(\frac{N\sqrt{\sigma_z}}{\sigma_x^*}\right)^{2/3} \cong \frac{n_\gamma}{3.3}.$$

This then gives the luminosity per unit beam power as

$$\frac{\mathcal{L}}{P_b} \cong \frac{\sqrt{5}}{16\alpha^2\sqrt{3r_e}\pi}\frac{\sqrt{\gamma n_\gamma^3}}{E_b\sigma_y^*\sqrt{\sigma_z}} \cong \frac{27}{25\sqrt{5}\pi\alpha^2\sqrt{r_e}}\frac{\sqrt{\gamma\delta_B^3}}{E_b\sigma_y^*\sqrt{\sigma_z}}. \tag{4.9}$$

For δ_B, n_γ and E_b fixed, it can be increased by reducing either the vertical beam size at the IP or the bunch length, as opposed to the classical beamstrahlung regime. Since $\Upsilon \propto \gamma$, for a collider with a centre of mass energy of $10\,\text{TeV}$ or more, it will be almost impossible to avoid entering the quantum beamstrahlung regime.

Coherent Beamstrahlung Pair Production

Beamstrahlung can lead to the coherent production of electron-positron pairs, constituting a detrimental background in detectors. The total number of created pairs per primary particle is given by [157, 159]

$$n_b = \left[\frac{\alpha\sigma_z}{\gamma\lambda_e}\Upsilon\right]^2 \Xi(\Upsilon), \tag{4.10}$$

with $\lambda_e \approx 2.4 \cdot 10^{-12}$ m the Compton wavelength of the electron and

$$\Xi(\Upsilon) \approx \begin{cases} (7/128)\exp(-16/3\Upsilon) & (\Upsilon \lesssim 1), \\ 0.295\Upsilon^{-2/3}(\ln\Upsilon - 2.488) & (\Upsilon \gg 1). \end{cases} \tag{4.11}$$

Note that the term in square brackets only depends on the beam density, cf. eq. (4.4). The values of the function Ξ are in the order $10^{-2} \lesssim \Xi < 10^{-1}$ for $2 \lesssim \Upsilon \lesssim 2000$. For $\Upsilon \lesssim 1$, $\Xi(\Upsilon)$ decreases exponentially, with $\Xi(\Upsilon \approx 0.3) \approx 10^{-9}$ - giving a much stronger suppression e.g. for longer bunches common for conventional accelerators.

Trident Cascade

In an electromagnetic field, electron-positron pairs can also be created through virtual photons carried by the primary particles. This process is sometimes called the trident cascade. The total number of created pairs per primary particle is given by [159]

$$n_\nu = \left[\frac{\alpha\sigma_z}{\gamma\lambda_e}\Upsilon\right]\Omega(\Upsilon), \tag{4.12}$$

with $\Omega(\Upsilon) \approx 0.23\alpha\ln(\Upsilon)$ for $\Upsilon \gg 1$. For $\Upsilon \lesssim 10^3$, $\Omega(\Upsilon) < \Xi(\Upsilon)$ [157].

4.2   Laser-Driven Linear Collider

For the quasi linear regime, a self consistent linear collider proposal supported by particle in cell simulations has been developed in [11, 21], and will be discussed below. Comparable numerical values have been found in [156].

The quasi linear regime allows for the acceleration of both electrons and positrons and allows some control over the transverse focusing forces, as the transverse force $F_\perp \propto \nabla_\perp a^2$. Operating in the quasi linear regime implies $k_p^2 r_L^2/2 > a_0^2/\gamma_\perp$ and $a_0^2 \sim 1$, with r_L the transverse RMS laser spot radius and $\gamma_\perp = \sqrt{1 + a_0^2/2}$. The accelerating field is then given by $E_z \approx 0.76(a_0^2/2\gamma_\perp)E_0$, with E_0 the classical wave breaking field (see chapter 2.3.3). Efficient excitation of plasma wakes in the linear regime requires the RMS laser pulse duration τ_L to be in the order of the plasma period, $\tau_L \omega_p \sim 1$ and hence $\tau_L \propto n_0^{-1/2}$. To avoid strong self-focusing of the laser (see chapter 2.5.4), one requires $P/P_c = (k_p^2 r_L^2 a_0)^2/32 \lesssim 1$ (for a linear polarized laser). Together with the condition that $k_p^2 r_L^2/2 > a_0^2/\gamma_\perp$, this implies a laser spot size of $3 \lesssim k_p r_L \lesssim 6$. With $P_L \propto \left(\frac{a_0 r_L}{\lambda}\right)^2$ (see chapter 2.4.2), for fixed a_0 and $k_p r_L$ the required peak power per LWFA stage therefore scales as $P_L \propto n_0^{-1}\lambda^{-2}$ and the laser energy per stage scales as $U_L \sim P_L \tau_L \propto n_0^{-3/2}\lambda^{-2}$. Assuming appropriately shaped bunches (as discussed in chapter 2.9.1), the number of particles that can be loaded into a short and narrow ($\ll \lambda_p$) segment without significant energy spread scales as $N \sim \pi n_0 k_p^{-3}(E_z/E_0) \propto n_0^{-1/2}$, assuming fixed E_z/E_0 (i.e. $\omega_p \tau_L$ and a_0 fixed). This means that a lower plasma density allows more charge to be loaded in a plasma wave bucket. Assuming laser dephasing and diffraction mitigated by appropriate plasma density tailoring (see chapters 2.5.4 and 2.5.5), the single stage energy gain is ultimately limited by the depletion of the laser. The energy depletion length is given by $L_d \sim \lambda_p^3/\lambda^2 \propto n_0^{-3/2}\lambda^{-2}$, giving a single stage energy gain of $W_{stage} \propto E_0 L_d \propto n_0^{-1}\lambda^{-2}$. The number of stages required to reach a given energy is then given by $N_{stages} \propto 1/W_{stage} \propto n_0\lambda^2$. The total length of the accelerator (determining the average acceleration gradient) is given by $(L_{stage} + L_c)E_b/W_{stage}$, with $L_{stage} \approx L_d$ the single stage plasma length, L_c the coupling distance for a new drive beam and E_b the final beam energy. Reducing the total linac length requires $L_c \sim L_{stage} \approx L_d$. The total linac length then scales as $L_{total} \propto L_d N_{stages} \propto n_0^{-1/2}$. This means that although operating at a lower plasma density increases the single stage energy gain, it also reduces the accelerating gradient and increases the depletion length, resulting in an increase of the total linac length. For a fixed luminosity (see equation 4.1), with E_B and the focusing at the interaction point fixed as well, the collision frequency has to scale as $f \propto N^{-2} \propto n_0$. This means that the beam power scales as $P_b = fNE_b \propto n_0^{1/2}$, the average laser power scales as $P_{avg} = fU_L \propto n_0^{-1/2}\lambda^{-2}$ and the total wall plug power scales as $P_{wall} \propto N_{stages}P_{avg} \propto n_0^{1/2}$, as illustrated in figure 4.1. A lower plasma density reduces the total power requirements, but increases the laser energy per stage and the total linac length. The scalings derived above are summarized in table 4.1. Based on particle in cell simulations, a set of consistent parameters of a linear collider has been found in [21], cf. table 4.2. A very similar set of parameters has been found by the ICFA-ICUIL joined task force [11, 93] (ICFA - International Committee for Future Accelerators, ICUIL - International Committee for Ultra-High Intensity Lasers). Except for the repetition rate, the required laser parameters for a single stage are very similar to those of the BELLA

$$
\begin{aligned}
E_z &\propto n_0^{1/2} & P_{peak} &\propto n_0^{-1}\lambda^{-2} \\
L_{stage} &\propto n_0^{-3/2}\lambda^{-2} & U_L &\propto n_0^{-3/2}\lambda^{-2} \\
W_{stage} &\propto n_0^{-1}\lambda^{-2} & f &\propto n_0 \\
N_{stage} &\propto n_0\lambda^2 & P_b &\propto n_0^{1/2} \\
L_{total} &\propto n_0^{-1/2} & \Upsilon &\propto n_0^{-1/2} \\
N &\propto n_0^{-1/2} & P_{avg} &\propto n_0^{-1/2}\lambda^{-2} \\
\tau_L &\propto n_0^{-1/2} & P_{wall} &\propto n_0^{1/2}
\end{aligned}
$$

Table 4.1: Scaling laws for LWFA linear collider as derived in [21] for a linear polarized laser pulse. Identical density scalings have been found in [156].
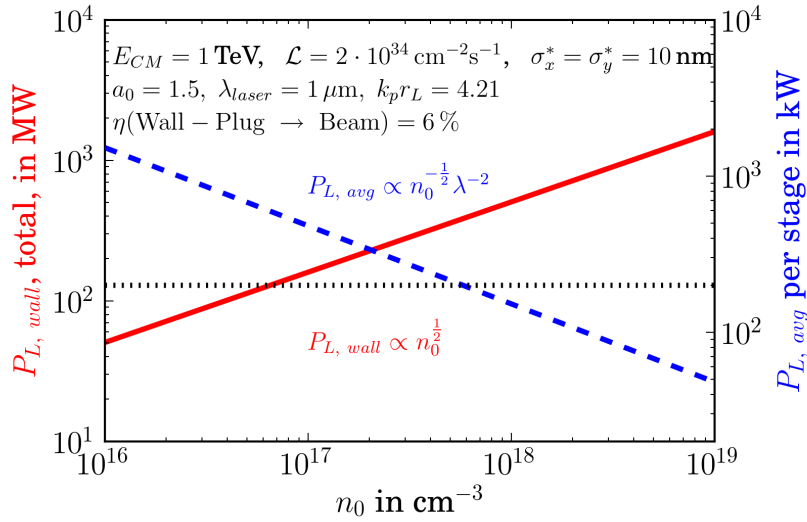
Figure 4.1: Total laser wall plug power $P_{L,\,wall}$ (red solid line) and average laser power per stage $P_{L,\,avg}$ (blue dashed line) over the average plasma electron number density n_0. Increasing the plasma density reduces the necessary laser power for each individual stage, but at the same time increases the total required wall plug power. Values derived using the scalings and example parameters determined in [21]. The total power consumption is for a linear collider with a centre of mass energy $E_{CM} = 1\,\text{TeV}$ and a luminosity of $\mathcal{L} = 2 \cdot 10^{34}\,\text{cm}^{-2}\text{s}^{-1}$ with a beam size at the interaction point of $\sigma_x^* = \sigma_y^* = 10\,\text{nm}$. A wall-plug to beam efficiency of $6\,\%$ is used in the example parameters. The dotted horizontal line marks the probable site power limit of $200\,\text{MW}$. Note that most current day laser systems have an average laser power of a few tens of Watts. The development of high intensity high average power lasers is actively pursued within ICAN, and tens of kW average laser power might become available within the next decades (see chapter 3.1.2, in particular tables 3.3 and 3.5).

facility, the *BE*rkeley *L*ab *L*aser *A*ccelerator [121, 160]. BELLA is operating at 1 Hz and aims at the development of 10 GeV LWFA modules operating in the quasi-linear regime. In [156], it has been suggested to work at significantly lower plasma densities to reduce the total power consumption. However, this results in a much higher number of particles per bunch, causing severe beamstrahlung effects. To limit the amount of generated beamstrahlung, one could accelerate less particles than possible for a given plasma density (increasing the repetition rate to keep up the luminosity), or distribute the N particles over m successive oscillations of the plasma wake. However, as shown in [155], this results in a higher power consumption, negating the advantages of operating at a lower plasma density.

Evaluation

Based on the scalings introduced above, the optimum plasma density for a given laser pulse energy has been calculated for a set of example laser facilities (which have been introduced in chapter 3.1.2, see tables 3.3 and 3.4). Based on the resulting number of particles in the accelerated witness bunch, the achievable luminosity for the corresponding repetition rate has been calculated via $\mathcal{L} = (fN^2)/(4\pi\sigma_x^*\sigma_y^*)$, see chapter 4.1. The result is illustrated in figure 4.2. Based on the scalings, a parameter scan has been performed. The results are given in tables 4.2 and 4.3 for centre of mass energies of 1 TeV and 3 TeV respectively. A facility capable of producing an expected Higgs boson with a mass of about 125 GeV/c^2 is discussed in chapter 4.7.4, page 65.

A question of interest that has not been discussed here is the availability of injectors to provide *shaped*, high charge bunches at a bunch length $\sigma_z \approx 1\,\mu$m. While the required charge and bunch length have both been reached individually, the bunches so far were of lower charge or longer than required. Also, to the best of the authors knowledge, bunch shaping has not been demonstrated for bunches of this length scale. An overview over beam parameters achieved so far is given in chapter 3.1.1.
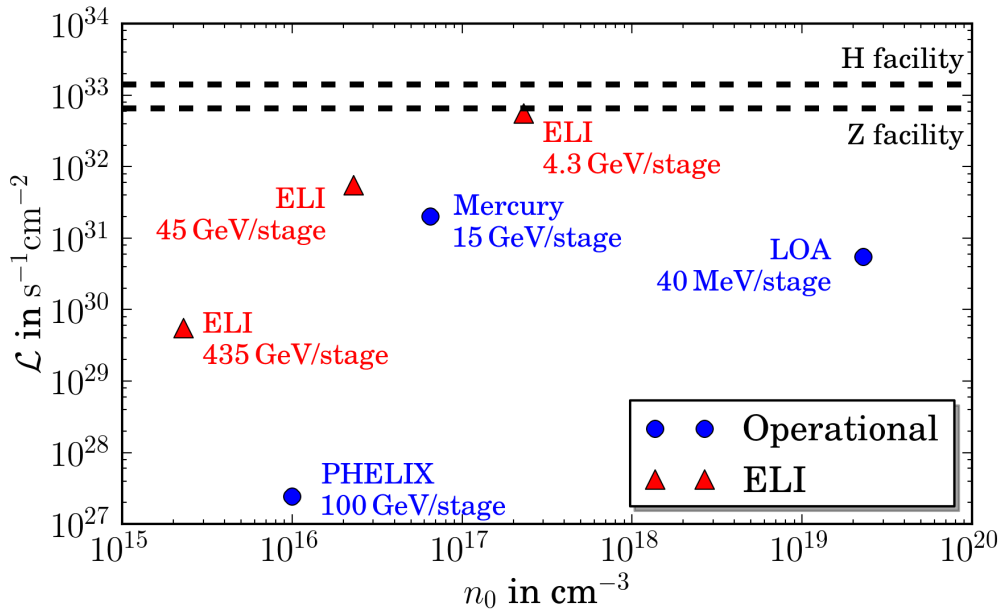
Figure 4.2: Achievable luminosity $\mathcal{L}$ versus plasma electron density n_0 based on laser pulse energy and repetition rate of exemplary high power laser facilities [117–120, 123]. Plasma density and number of particles per bunch were calculated from the pulse energy via the scalings in [21] (here, it has been assumed the pulse length can be adjusted accordingly and that enough modules are staged to reach the desired final energy). A spot size at the collision point of $\sigma_x^* = \sigma_y^* = 10\,\mathrm{nm}$ has been assumed.

The broken horizontal lines denote the minimal useful luminosity for a Higgs / Z-boson facility, as given by the scaling $\mathcal{L}[10^{34}\,\mathrm{cm}^{-2}\mathrm{s}^{-1}] \approx (E[\mathrm{TeV}])^2$ [64]. For a dedicated H / Z *factory*, a luminosity increase by two orders of magnitude would be desirable. A full scale TeV linear collider would require a luminosity in excess of $10^{34}\,\mathrm{s}^{-1}\mathrm{cm}^{-2}$ to generate sufficient event rates. Also see figure 3.2, which illustrates the correlation of laser pulse energy and repetition rate and tables 3.3 and 3.4 for parameters of existing laser facilities / ELI.

	2.0e15	1.0e16	2.3e16	6.5e16	1.0e17	2.33e017	1.0e18	2.32e019
Plasma electron density n_0 [cm^{-3}]								
Particles per bunch N_{bunch} [1e9]	28.3	12.6	8.3	5.0	4.0	2.6	1.3	0.3
Energy gain per stage W_{stage} [GeV]	500.0	100.0	43.5	15.4	10.0	4.3	1.0	0.04
Number of stages N_{stages}	1	5	12	33	50	117	500	11600
Laser energy per stage U_L [J]	11313.7	1011.9	290.1	61.1	32.0	9.0	1.0	0.01
Avg laser power per stage P_{avg} [kW]	3394.1	1517.9	1000.9	595.4	480.0	314.5	151.8	31.5
Collision frequency f [kHz]	0.3	1.5	3.45	9.75	15	34.95	150	3480
Total wall-plug power P_{wall} [MW]	22.6	50.6	76.7	129.0	160.0	244.2	506.0	2437.0
Laser pulse duration τ_{laser} [fs]	396.0	177.1	116.8	69.5	56.0	36.7	17.7	3.7
Beam power P_{beam} [MW]	0.7	1.5	2.3	3.9	4.8	7.3	15.2	73.1
Beamstrahlung parameter Υ	1272.8	569.2	375.3	223.3	180.0	117.9	56.9	11.8
No. of Beamstrahlung photons n_γ	5.420	3.160	2.388	1.683	1.455	1.092	0.664	0.220
Beamstrahlung energy spread δ_E	1.630	0.944	0.710	0.497	0.427	0.318	0.188	0.055
Coherent Beamstrahlung pairs n_b	1.57e+0	3.13e-1	1.36e-1	4.82e-2	3.13e-2	1.34e-2	3.13e-3	1.35e-4
Trident Cascade pairs n_ν	3.96e-1	1.77e-1	1.17e-1	6.94e-2	5.59e-2	3.67e-2	1.77e-2	3.67e-3
Length of single stage L_{stage} [m]	353.6	31.6	9.1	1.9	1.0	0.3	0.03	0.0003
Total linac length (1 arm) [km]								
$\quad L_{stage}$ for coupling	0.71	0.32	0.22	0.13	0.10	0.066	0.032	0.0066
$\quad$ 0 m for coupling	0.35	0.16	0.11	0.063	0.050	0.033	0.016	0.0033
$\quad$ 5 m for coupling	0.36	0.18	0.17	0.23	0.30	0.62	2.5	5.8
$\quad$ 10 m for coupling	0.36	0.21	0.23	0.39	0.550	1.2	5.0	11
$\quad$ 25 m for coupling	0.38	0.29	0.41	0.89	1.3	3.0	13	29

Table 4.2: Parameter scan for a possible linear collider, based on the parameters and scalings in [21] (the values for $n_0 = 10^{17}$ cm^{-3} are the ones from the reference). For $n_0 = 10^{17}$ cm^{-3} and $n_0 = 2 \cdot 10^{15}$ cm^{-3}, almost identical values have been found in [11]. The final energy per arm is $E_b \approx 0.5$ TeV. The luminosity is $\mathcal{L} = 2 \cdot 10^{34}$ cm^{-2}s^{-1}, for a beam size at the IP $\sigma_x^* = \sigma_y^* = 10$ nm and a bunch length $\sigma_z = 1\,\mu$m. The assumed laser wavelength is $1\,\mu$m. Plasma densities were chosen to correspond to the laser pulse energies given in tables 3.3 and 3.4, page 37. A wall-plug to beam efficiency $\eta = 6\,\%$ is assumed, $P_{wall} = 2 \cdot P_{beam}/\eta$. Parameters related to Beam-Beam interaction have been calculated using the equations given in chapter 4.1.2, under the pessimistic approximation that $\Xi(\Upsilon) = \Omega(\Upsilon) = 10^{-1}$.

	8.3e15	2.5e16	5.0e16	7.5e16	1.0e17	2.5e17	5.0e17	7.5e17	1.0e18	2.5e18	5.0e18	1.0e19
Plasma electron density n_0 [cm^{-3}]	8.3e15	2.5e16	5.0e16	7.5e16	1.0e17	2.5e17	5.0e17	7.5e17	1.0e18	2.5e18	5.0e18	1.0e19
Particles per bunch N_{bunch} [1e9]	13.9	8.0	5.7	4.6	4.0	2.5	1.8	1.5	1.3	0.8	0.6	0.4
Energy gain per stage W_{stage} [GeV]	120.5	40.0	20.0	13.3	10.0	4.0	2.0	1.3	1.0	0.4	0.2	0.1
Number of stages N_{stages}	13	38	75	113	150	375	750	1125	1500	3750	7500	15000
Laser energy per stage U_L [J]	1338.2	256.0	90.5	49.3	32.0	8.1	2.9	1.6	1.0	0.3	0.1	0.03
Avg laser power per stage P_{avg} [kW]	1666.1	960.0	678.8	554.3	480.0	303.6	214.7	175.3	151.8	96.0	67.9	48.0
Collision frequency f [kHz]	1.245	3.75	7.5	11.25	15	37.5	75	112.5	150	375	750	1500
Total wall-plug power P_{wall} [MW]	138.3	240.0	339.4	415.7	480.0	758.9	1073.3	1314.5	1517.9	2400.0	3394.1	4800.0
Laser pulse duration τ_{laser} [fs]	194.4	112.0	79.2	64.7	56.0	35.4	25.0	20.4	17.7	11.2	7.9	5.6
Beam power P_{beam} [MW]	4.1	7.2	10.2	12.5	14.4	22.8	32.2	39.4	45.5	72.0	101.8	144.0
Beamstrahlung parameter Υ	1874.4	1080.0	763.7	623.5	540.0	341.5	241.5	197.2	170.8	108.0	76.4	54.0
No. of Beamstrahlung photons n_γ	2.341	1.618	1.283	1.120	1.017	0.747	0.591	0.516	0.468	0.343	0.271	0.213
Beamstrahlung energy spread δ_E	0.705	0.486	0.384	0.335	0.304	0.222	0.175	0.152	0.137	0.099	0.078	0.060
Coherent Beamstrahlung pairs n_b	3.77e-1	1.25e-1	6.26e-2	4.17e-2	3.13e-2	1.25e-2	6.26e-3	4.17e-3	3.13e-3	1.25e-3	6.26e-4	3.13e-4
Trident Cascade pairs n_ν	1.94e-1	1.12e-1	7.91e-2	6.46e-2	5.59e-2	3.54e-2	2.50e-2	2.04e-2	1.77e-2	1.12e-2	7.91e-3	5.59e-3
Length of single stage L_{stage} [m]	41.8	8.0	2.8	1.5	1.0	0.3	0.1	0.049	0.032	0.008	0.003	0.001
Total linac length (1 arm) [km]												
$\quad L_{stage}$ for coupling	1.087	0.608	0.424	0.348	0.300	0.190	0.134	0.110	0.095	0.060	0.042	0.030
$\quad$0 m for coupling	0.54	0.30	0.21	0.17	0.15	0.10	0.07	0.06	0.05	0.03	0.02	0.02
$\quad$5 m for coupling	0.61	0.49	0.59	0.74	0.90	1.97	3.82	5.68	7.55	1.88	3.75	7.50
$\quad$10 m for coupling	0.67	0.68	0.96	1.30	1.65	3.84	7.57	11.3	15.0	37.5	75.0	150
$\quad$25 m for coupling	0.87	1.25	2.09	3.00	3.90	9.47	18.8	28.2	37.5	93.8	187	375

Table 4.3: Parameter scan for a possible linear collider, based on the parameters and scalings in [21]. The final energy per arm is $E_b \approx 1.5\,\mathrm{TeV}$. The initial scaling assumes a luminosity $\mathcal{L} = 2 \cdot 10^{34}\,\mathrm{cm^{-2}s^{-1}}$, for a beam size at the IP $\sigma_x^* = \sigma_y^* = 10\,\mathrm{nm}$ and a bunch length $\sigma_z = 1\,\mu\mathrm{m}$. Following the scaling 4.3, the luminosity should be increased to compensate for the lower interaction cross sections at higher energy. This could be achieved via a 9 times higher collision frequency (which would result in an increase in beam and wall-plug power by the same amount). Parameters related to Beam-Beam interaction have been calculated using the equations given in chapter 4.1.2, under the pessimistic approximation that $\Xi(\Upsilon) = \Omega(\Upsilon) = 10^{-1}$.

4.3   Electron-Driven Linear Collider

Several proposals on linear colliders based on PWFA can be found in the literature [140, 145–151, 161] They fall in two main categories; the staged approach and the afterburner concept, which will both be discussed below. All the before mentioned collider proposals aim at operation in the bubble regime. This makes the acceleration of positrons very difficult, as they can only be accelerated at the density spike at the end of the bubble. Simulations in [162] show that positrons can be accelerated in an electron beam driven bubble, if the energy content of the wake is not too high. However, this requires precise positioning and sophisticated bunch shaping on a scale given by the plasma wave length. Even then, an energy spread of several percent can not be avoided, due to the structure of the accelerating field which varies across the beam. Simulations in [163] also indicate the formation of a beam halo and an increase of the positron beam emittance. If positrons are used to drive the wake, the resulting accelerating field is lower than for the electron driver, and their effect of "sucking in" instead of blowing out plasma electrons leads to considerably different transverse fields [62]. A plasma in the shape of a hollow cylinder can be used to mitigate these problems. Another option would be to use electrons to drive a linear wake to accelerate positrons [164]. Alternatively, the collider could be constructed as photon-colliders, as discussed in section 4.5.

In the scope of this thesis, several scalings with plasma density for a beam-driven linear collider operating in the blowout regime have been derived. They have been discussed in chapter 2.8.3.

4.3.1   Staged Approach

The staged approach for PWFA [140, 145–147, 161] is conceptionally similar to the approach with LWFA (chapter 4.2), but due to the higher energy stored in each drive beam the number of necessary stages is significantly reduced. For example, the straw man design in [147] uses 10 stages, each adding 25 GeV to the witness bunch. While the length of the individual plasma cells would be in the order of 1 m, the overall length of the accelerator would probably be a few kilometres [145], to allow the coupling of the drive bunches and the transport of the witness bunch from stage to stage. In particular, to allow the use of one single, heavily beam-loaded drive linac, the distance between plasma cells is given by the rise time of the kicker magnet that distributes the beam to the different stages, resulting in a coupling distance of about 90 m [161].

A $\gamma\gamma$-collider based on 25 GeV stages is discussed in chapter 4.7.5.

4.3.2   Afterburner

The afterburner concept [148–151] was originally suggested in [148] to double the energy of the Stanford Linear Accelerator, to enable it to find a low mass Higgs boson. It has been suggested in [149] as a possibility to increase the energy or reduce the cost of the ILC.

The main idea is that electrons (positrons) will be accelerated to half the final energy in a RF linac like ILC, before they enter a plasma cell. In the plasma cell some of the electrons will drive a plasma wake, transferring their energy to the trailing bunch. The creation of

drive and witness bunch (with different particle number and bunch length) can be either achieved from the injector or by over compressing a long bunch in a magnetic chicane. The principle of the afterburner concept has been demonstrated at SLAC [13] and will be further investigated at FACET [109].

4.4 Proton-Driven Linear Collider

Three collider proposals utilizing the proton driven plasma wake field acceleration concept described in chapter 2.7 have been developed in [152, 153, 165].

The AWAKE experiment at CERN is working towards the first experimental demonstration of proton-driven electron acceleration. My contribution to the AWAKE project is described in chapter 6.

Proton Based ILC Upgrade

In [152], an upgrade of the ILC using proton driven plasma wake field acceleration has been suggested. The key idea is to accelerate protons in the same superconducting linacs used to accelerate the electrons and positrons. This would allow the doubling of the final energy with only a slight increase in accelerator length. Several dual path chicanes along the linacs would be used to compensate the phase slippage between the electrons and the protons of lower relativistic γ. A final dual path chicane would be used both to allow the protons to overtake the electrons (They would travel behind the electrons in the linacs to not spoil the electron bunches with their wake fields) and to compress their bunch length before entering into a long plasma cell in which the protons would transfer part of their energy to the electrons, accelerating them from $250\,\mathrm{GeV}$ to $500\,\mathrm{GeV}$. For the positron arm, a similar setup would be used, but with the proton beam injected later into the linac. The lower energy proton bunch of higher intensity would be used to create wake fields of comparable strength as for the electron arm while still being separable from the positrons due to their lower momentum. This concept is very similar to the afterburner concept discussed in section 4.3.2. The difference is that here protons are used to drive the plasma wake, not some of the bunches within a train.

Electron-Proton Collider

An electron-proton (e$^-$-p) collider similar to the linac-ring option of the proposed LHC upgrade LHeC [166] (Large Hadron electron Collider) has been developed in [165], employing existing CERN accelerators. The idea is to use self modulated proton bunches from the SPS to accelerate electrons to $100\,\mathrm{GeV}$ in a single $170\,\mathrm{m}$ plasma cell. These electron bunches will be collided with proton bunches within the LHC. The SPS accelerates 288 bunches with a cycling time of about $20\,\mathrm{s}$, resulting in a possible collision frequency of about $15\,\mathrm{Hz}$. Assuming an electron bunch with $1.15 \cdot 10^{10}$ particles ($10\,\%$ of the drive beam charge) and transversely matched beams with a β_p^* values for the proton bunch of $0.1\,\mathrm{m}$, an e$^-$-p luminosity of $1 \cdot 10^{30}\,\mathrm{cm}^{-2}\mathrm{s}^{-1}$ is predicted. This is roughly 3 orders of magnitude lower than what is targeted for LHeC, but with twice the electron energy and without the need to build a new accelerator.

Dedicated Proton Driver

The probably most promising possibility to reach the beam quality and luminosity desired for a future lepton collider is the construction of a dedicated facility. The ramp time of existing, circular colliders is typically in the order of 30 minutes, due to the characteristics of the super conducting magnets. If protons were to be extracted from such accelerators to accelerate electrons in a single, long plasma cell, the average extracted beam power would be in the order of a few kW, much lower than the estimated beam power of 50 MW for ILC. Assuming a 10 % efficiency for the coupling from the protons to the plasma wake and 50 % efficiency from the plasma wake to the witness bunch, 1 GW of proton beam power would be needed for a luminosity comparable to the one planned for ILC. In [153], it has been suggested to improve the proton accelerator cycling times by using a combination of a rapid cycling pre-accelerators, a 500 GeV to 1 TeV fixed field alternative gradient lattice and possibly a superconducting final synchrotron for the acceleration of protons to 2 TeV.

4.5   Photon-Photon Collider

Considering a photon ($\gamma\gamma$) Collider is appealing due to several reasons [21, 167]: i) The detrimental effects associated with beam-beam interaction discussed in section 4.1.2 are absent. ii) They eliminate the need for positrons, potentially even for damping rings. iii) $\gamma\gamma$ collisions can access many of the interactions available in e^+e^- colliders, and the different production channels would provide valuable additional information. iv) If a high energy e^+e^--collider where to be build, a second interaction region for $\gamma\gamma$ or γe collisions would be a comparably cheap addition. Moreover, in a $\gamma\gamma$ collider the cross section for several physics processes of interest is significantly larger than in an e^-e^+ collider of the same energy [93, 167, 168].

The required photon beams can be generated with sufficiently high rates via Compton scattering on an electron beam. The laser requirements are very similar to those needed for LWFA [21, 93]. The energy of the created photons is given by $\hbar\omega = E_b x/(1 + x + a_L^2)$, with E_b the energy of the electron beam on which the laser beam is backscattered and a_L^2 the normalized laser intensity. $x = (4 E_b \hbar\omega_L/(m_e^2 c^4)) \cos^2(\theta/2)$, with ω_L the angular frequency of the scattering laser and $\theta \ll 1$ the collision angle. To maximize the energy of the scattered photons while avoiding e^+e^- pair production in the same laser beam imposes the condition $x \leq 2(1 + a_L^2)(1 + \sqrt{2})$ or $\lambda_L\,[\mu m] \approx 4 E_b\,[\text{TeV}]$ on the scattering laser (for $a_L \ll 1$). By correlating the laser and electron beam pulse length to the Rayleigh length of the laser one can estimate the laser energy necessary for efficient energy conversion to $U_L\,[\text{J}] \approx (2/a_L^2) E_b\,[\text{TeV}]$. The pulses must be sufficiently long so that $a_L^2 < 1$ to avoid nonlinear scattering. Furthermore, minimizing bremsstrahlung puts a restraint on the peak electric field of the laser in the rest frame of the electron beam: $a_L < 2/x$.

The electron beam could be provided by any of the accelerator concepts mentioned above. The cross sections for charged particle production are somewhat higher in $\gamma\gamma$ collisions than they are for e^+e^-. This allows the reduction of the required luminosity in the high energy peak of the photon spectrum by about a factor of 5 as compared to the required

e^+e^--luminosity of a collider of similar energy [169]. However, due to the characteristics of the photon generation via Compton scattering, only about 10 % of the photons are in the high energetic peak of the photon spectrum. Therefore, the *geometric* luminosity, the luminosity the electrons would generate if not used to scatter photons, should be similar to that of an e^+e^--collider [168], roughly following the scaling given by equation 4.3 [169]. It is important to point out that a $\gamma\gamma$-collider is a relatively cheap upgrade of an existing e^+e^--collider, delivering interesting and complimentary physics. It is however unlikely that the high energy physics community will want a sole $\gamma\gamma$-collider without the option of e^+e^- collisions [168].

A design for a 130 GeV Higgs factory photon-photon collider has been developed in the course of this work and is discussed in chapter 4.7.5.

4.6 Muon Collider

Beamstrahlung is is a mixture of synchrotron radiation and Bremsstrahlung, with the ratio between the two depending on the beam parameters [170]. Either way, the amount of radiated power is proportional to γ^4, and can therefore be reduced significantly by using heavier particles. If one were to use muons instead of electrons, the amount of emitted radiation would be reduced by over 9 orders of magnitude ($m_\mu \approx 207\, m_e$). Muons are unstable and decay as $dN/dt = -N/\gamma\tau_0$. However, this becomes largely irrelevant for high accelerating gradients, as the fraction of surviving particles at the final energy E

$$\frac{N}{N_0} \approx \left(\frac{m_\mu c^2}{E}\right)^\kappa \tag{4.13}$$

is very close to 1 if $\kappa = (m_\mu c/\tau_0 G) \ll 1/\ln(E/m_\mu c^2)$ [154]. This condition is well fulfilled if the acceleration gradient $G \gg 3\,\mathrm{MeV/m}$. However, due to their production mechanism via scattering of a particle beam on a target, muon beams are created with a very large emittance. For a TeV scale collider, a reduction of the 6-dimensional phase space by a factor $\mathcal{O}(10^6)$ will probably be necessary. A convincing demonstration of the necessary muon cooling is envisaged on the timescale of 2020 [154]. While this approach allows to operate with much lower plasma densities without running into problems with excessive beamstrahlung, the usefulness of this approach has to be evaluated depending on the achievable efficiency in the generation of the Muons.

Another problem has not been discussed in the proposal mentioned above; due to the large emittance with which the muons are created, it is not at all clear if they can easily be focused into the small accelerating volume of the plasma wave. If not, it would make the use of conventional acceleration techniques necessary. The idea has therefore not been investigated further in this thesis.

4.7   A 130 GeV Higgs Factory

4.7.1   Motivation

Recently, the long sought Higgs boson has been discovered at the LHC [16, 17]. Its relatively low rest mass of approximately $125 \, \text{GeV}/c^2$ makes it interesting to consider a smaller scale linear collider based on plasma technology - both to study the new boson in more detail in electron-positron collisions and to develop the technologies necessary for a full scale collider.

To that end, I have investigated protons, electrons and laser pulses as potential drivers for such a facility, as will be discussed in sections 4.7.2 to 4.7.5.

For electron-positron collisions, the maximal cross section of $200 \, \text{fb}$ for $e^+e^- \rightarrow ZH$, is at a centre of mass energy of about $250 \, \text{GeV}$ [66], resulting in a required energy per beam of approximately $125 \, \text{Gev}/c^2$. For $\gamma\gamma$ collisions, a single Higgs can be produced [171, 172]. The required energy per driving electron beam is therefore $\frac{1}{2}(125/0.8) \approx 80 \, \text{GeV}$, cf. section 4.5, page 60.

4.7.2   Protons as Drive Beam

I have investigated protons a potential drivers. The energy stored in a $125 \, \text{GeV}$ Proton beam would be sufficient to accelerate electrons to the same energy in a single stage, avoiding the challenges associated with staging. However, as explained in chapter 2.7.3, dephasing can be a serious problem for protons drivers of moderate γ. Using equation 2.44, page 22

$$\delta \approx \frac{1}{eE_{acc}/(m_e c \omega_p)}(\gamma_{e,fin} - \gamma_{e,in}) \left[1 - \frac{\gamma_{p,fin} - \gamma_{p,in}}{\sqrt{\gamma_{p,fin}^2 - 1} - \sqrt{\gamma_{p,in}^2 - 1}} \right] \qquad (4.14)$$

the phase slippage in a single acceleration stage depending on the initial and final γ_p has been studied. An accelerating field in the order of the cold wave breaking field ($eE_{acc}/(m_e c \omega_p) \approx 1$) and an initial electron beam of low energy ($\gamma_{e,fin} - \gamma_{e,in} \approx \gamma_{e,fin}$) have been assumed. The condition on the phase slippage has been tightened to $\delta < \pi/2$ to not only stay in the accelerating but also in the focusing phase of the wake (for operation in the linear regime, allowing to accelerate positrons as well). As illustrated in figure 4.3, a proton driver with an energy significantly higher than $125 \, \text{GeV}$ would be needed to accelerate electrons to this energy without suffering from dephasing. This makes protons unattractive as potential drivers.

4.7.3   LWFA Electron-Positron Collider,
Classical Beamstrahlung Regime

For the collision of charged particles, the amount of generated beamstrahlung $\Upsilon \propto \gamma$ scales with the beam energy, cf section 4.1.2. For e^+e^- collisions, producing the Higgs particle at its maximal cross section requires a centre of mass energy of approximately $250 \, \text{GeV}$ [66]. It is important to point out that for these energies, it is still possible to operate in the favourable classical beamstrahlung regime $\Upsilon \ll 1$.
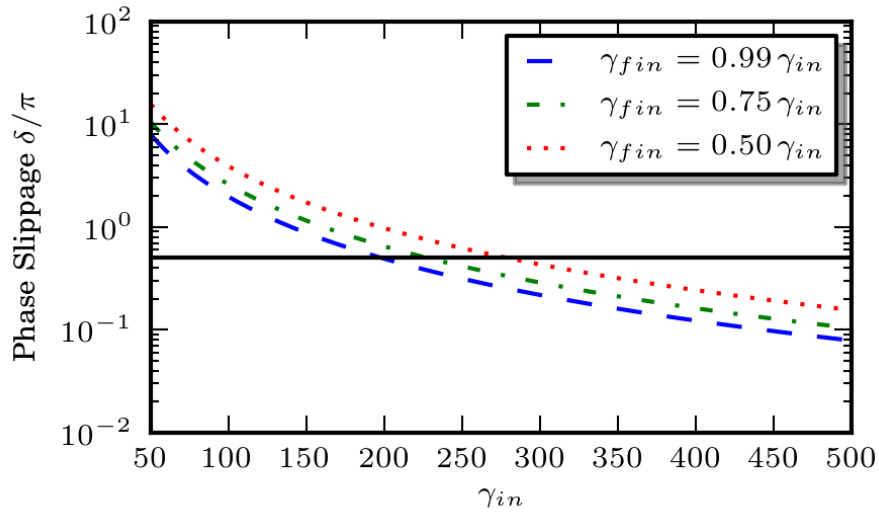
Figure 4.3: Phase slippage δ of an accelerated electron beam with respect to the driving proton beam, as calculated via equation 4.14. The x-axis is the initial relativistic γ-factor of the proton driver. The broken coloured lines denote different final energies of the driver, i.e. the transfer efficiency from the driver to the witness bunch. (Different final energies for the proton bunch can be achieved with different numbers of particles in the drive and witness bunch, cf. chapter 2.6.2.) The final energy of the electron beam used for the calculation is 125 GeV in all cases. (Although in practice, the electrons would not reach this energy if the phase slippage is too high.) The horizontal solid line denotes the maximal tolerable phase slippage $\delta = \pi/2$. As one can see, a proton driver with an initial energy much larger than 125 GeV would be needed to avoid detrimental phase slippage of $\delta \gtrsim \pi/2$.

As acceleration of positrons in the bubble regime is difficult, I have investigated a LWFA-collider operating in the linear regime, based on the example parameters and scalings given in [21] (cf. chapter 4.2, page 52). The beam parameters given there result in a beamstrahlung parameter $\Upsilon = 180$ for a centre of mass energy $E_{CM} = 1\,\text{TeV}$. As $\Upsilon \propto \gamma$, this leads to $\Upsilon \approx 45$ for $E_{CM} = 0.25\,\text{TeV}$. This makes it worth while trying to reach the classical beamstrahlung regime, in which the competing conventional collider proposals ILC and CLIC operate (ILC has $\Upsilon \ll 1$ for $E_{CM} = 1\,\text{TeV}$, CLIC has $\Upsilon \approx 5$ for $E_{CM} = 3\,\text{TeV}$ [64].). This is especially important as both n_γ and δ_B increase for lower beam energy, as stated by equations 4.5 and 4.6 on page 49.

As the final spot size at IP is independent of the plasma density, the amount of generated beamstrahlung scales with the number of particles per bunch N and therefore the plasma electron density n_0 as $\Upsilon \propto N \propto n_0^{-1/2}$. This hints at using higher plasma densities, resulting in less particles per bunch. However, this in turn results in a higher required collision frequency $f \propto n_0$ to keep up the luminosity and a higher required wall plug power $P_{wall} \propto n_0^{1/2}$. Scaling the parameters given in [21] to $E_{CM} = 0.25\,\text{TeV}$ and $n_0 = 10^{19}\,\text{cm}^{-3}$ results in $\Upsilon \approx 4.5$, still much higher than what is achievable with conventional accelerators like ILC.

I have performed a parameter scan, which shows that for $n_0 = 10^{19}\,\text{cm}^{-3}$, one already requires 1250 stages per arm and a wall plug power of 400 MW for a luminosity $\mathcal{L} = 2 \cdot 10^{34}\,\text{cm}^{-2}\text{s}^{-1}$, cf. table 4.6, page 68. As $P_{avg} \propto E_{CM}$, this is more than with ILC / CLIC technology. For comparison, the basic ILC design parameters are given in table 4.4.

Peak Luminosity $\mathcal{L}$ [cm^{-2}s^{-1}]	$2 \cdot 10^{34}$
Pulse rate [Hz]	5.0
Bunches per pulse	1000 -5400
Charge per bunch [nC]	1.6-3.2
Normalized horizontal emittance at IP [mm·mrad]	10 - 12
Normalized vertical emittance at IP [mm·mrad]	0.02 - 0.08
Typical beam size at IP (hor. × vert.) [nm]	474 - 640 × 3.5 - 9.9
Beam Power per beam [Mw]	11
Total AC Power consumption [MW]	230
RMS bunch length [μm]	200 - 500
Fractional beamstrahlung energy loss δ_E	0.017 - 0.055
Linac length (1 arm) [km]	8

Table 4.4: Basic design parameters for the International Linear Collider (ILC) at a centre of mass energy of 500 GeV, taken from tables 1.1-1 and 1.3-1 in [5]. The given values do not represent consistent parameter sets, but only indicate the span of the design range for each parameter. Also note that damping rings are necessary to reach the beam sizes at the interaction point (IP) and in turn the given luminosity.

Interim Conclusion

Due to the very short bunch lengths inherent to LWFA, they suffer from high emission rates for beamstrahlung photons and a large beamstrahlung induced energy spread. Therefore, even if there is no induced energy spread due to the acceleration process, the maximal achievable beam quality is noticeably better for conventional accelerators. However, as their much longer main linac length and the need for damping rings may make them prohibitory expensive it is worth studying plasma based accelerators operating in the quantum beamstrahlung regime. This in turn may make the development of new detectors necessary.

4.7.4   LWFA Electron-Positron Collider, Quantum Beamstrahlung Regime

As shown in the previous section, if one wants to achieve the highest possible beam quality, the use of conventional accelerator is beneficial for this energy range. In this chapter, we will assume that beamstrahlung does not pose a hard limit, either due the development of detectors that can cope with much higher beamstrahlung or due to the compensation of beamstrahlung by some other mechanism.

Several methods to reduce beamstrahlung have been suggested in the literature. In [173], it has been suggested to have a plasma at the IP, the return currents of which would mitigate the strong fields of the colliding bunches. However, for the plasma densities required, it is estimated that this would lead to other types of detrimental background due to the interaction of the beams with the plasma ions. In [174, 175], it has been suggested to consider the overlapping of identical beams of opposite charge. Colliding these e^+e^- pairs would provide full neutralization of beam charges and current. However, the requirements for alignment, synchronization and charge compensation are very stringent, given by the dimensions of the colliding bunches. If not met exactly, the mismatch will again result in dipole fields and therefore in the creation of beamstrahlung.

Based on the parameters and scalings in [21], I have performed parameter scans for beam energies sufficient to produce Z and H bosons. The results are given in tables 4.5 and 4.6. The beamstrahlung properties have been calculated using equations 4.4 to 4.6, page 49. Note that for $\Upsilon \gg 1$, the number of generated beamstrahlung photons n_γ and the beamstrahlung induced energy spread δ_E scale as $n_\gamma \propto \delta_E \propto \gamma^{-1/3}$. Since $N \propto n_0^{-1/2}$, this means that $n_\gamma \propto \delta_E \propto N^{2/3} \propto n_0^{-1/3}$.

Discussion

Assuming that

i) beamstrahlung does not pose a limit;

ii) laser systems providing the desired pulse energy and repetition rate and

iii) plasma cells of the required length were available for all parameter sets;

the scalings would dictate that for a Z / H facility, one would like to operate at plasma densities of $n_0 = 2.2 \cdot 10^{16}\,\mathrm{cm}^{-3}$ and $n_0 = 7.6 \cdot 10^{15}\,\mathrm{cm}^{-3}$ respectively. This would minimize the facility footprint and power consumption and remove the need for staging.

As reaching these three assumptions, if ever possible, will require serious research and development efforts I have considered how one could arrive at an operational facility at an earlier point in time. Ideally, one would like to start with a Z facility with the option to upgrade to a higher energy H facility later. Setting a maximal tolerable amount of beamstrahlung for the Z facility, this sets a lower limit to the plasma density, as $n_\gamma \propto \delta_E \propto \gamma^{-1/3} n_0^{-1/3}$.

If one now assumes that the fibre-based laser systems researched within ICAN will be the first technology to reach high average powers with decent wall-plug to optical efficiency, this puts a mid-term limit on the repetition frequency. Luminosity considerations for the H facility then limit the usable plasma density to $n_0 \lesssim 1 \cdot 10^{18}\,\mathrm{cm}^{-3}$. For my preliminary study, a plasma density of $n_0 \approx 5 \cdot 10^{17}\,\mathrm{cm}^{-3}$ limits the beamstrahlung induced energy spread to $40\,\%$ for the Z facility, reducing the challenge of detector development. Operation at $10\,\mathrm{kHz}$ could then deliver a luminosity of $\mathcal{L} \approx 3 \cdot 10^{33}\,\mathrm{cm}^{-2}\mathrm{s}^{-1}$. For the H-facility, this results in a total wall plug power consumption for both linac arms of about $12\,\mathrm{MW}$ (assuming a wall-plug to beam efficiency of $6\,\%$) and a footprint of about $700\,\mathrm{m}$ (assuming a coupling distance between plasma stages of $5\,\mathrm{m}$).

For this parameter set, I have compared the results concerning beam-beam interaction at the IP obtained by theoretical estimates (cf. table 4.6 for $n_0 \approx 5 \cdot 10^{17}\,\mathrm{cm}^{-3}$) to simulations [176] (comparison also published in [112]). They are in good agreement for the beamstrahlung induced energy spread δ_E and the number of emitted beamstrahlung photons n_γ. However, the simulations predict the number of generated coherent pairs $n_b \approx 0.1$ to be two orders of magnitude higher than the (already very high) theoretical estimate. It is also worth pointing out that, according to the simulations, the number of particles that keeps an energy higher than $99\,\%$ of the design energy is reduced by a factor of 3 due to beamstrahlung. This means a reduction of the effective luminosity.

4.7.5   Photon-Photon Collider, PWFA in the Bubble Regime

During the course of this thesis, I have investigated the possibility to build a Higgs facility based on the photon-photon ($\gamma\gamma$)-collider concept introduced in section 4.5. This has the advantage that, unlike e^+e^--colliders, $\gamma\gamma$-colliders can produce a single Higgs [172], reducing the required centre of mass energy by a factor of two and the required electron beam energy by about $35\,\%$.

As positrons are not required for a $\gamma\gamma$- or γe^--collider, this allows operation in the blowout regime, making use of its higher accelerating gradient and its beneficial focusing properties discussed in chapters 2.1.2 and 2.8.

For a laser driver, the phase velocity of the plasma wake is approximately the group velocity of the driving laser pulse, normally with an associated γ-factor between 10 and 100. This rather low phase velocity allows for the trapping of background electrons, reducing the acceleration gradient and increasing the energy spread of the witness beam [21]. For my straw-man design, I have therefore chosen to employ a beam driver, for which the phase velocity of the wake is approximately given by the velocity of the beam [12]. The much higher associated γ-factor effectively prevents trapping of background plasma electrons.

Plasma electron density n_0 [cm^{-3}]	2.2e16	4.35E+016	7.5e16	1.0e17	2.5e17	5.0e17	7.5e17	1.0e18	2.5e18	5.0e18	1.0e19
Particles per bunch N_{bunch} [1e9]	8.5	6.1	4.6	4.0	2.5	1.8	1.5	1.3	0.8	0.6	0.4
Energy gain per stage W_{stage} [GeV]	45.5	23.0	13.3	10.0	4.0	2.0	1.3	1.0	0.4	0.2	0.1
Number of stages N_{stages}	1	2	4	5	12	23	34	45	113	225	450
Laser energy per stage U_L [J]	310.1	111.5	49.3	32.0	8.1	2.9	1.6	1.0	0.3	0.1	0.03
Avg laser power per stage P_{avg} [kW]	1023.4	727.8	554.3	480.0	303.6	214.7	175.3	151.8	96.0	67.9	48.0
Collision frequency f [kHz]	3.3	6.525	11.25	15	37.5	75	112.5	150	375	750	1500
Min. collision frequency f_{min} [kHz]	0.027	0.053	0.091	0.12	0.30	0.61	0.91	1.2	3.0	6.1	12.2
Total wall-plug power P_{wall} [MW]	6.8	9.5	12.5	14.4	22.8	32.2	39.4	45.5	72.0	101.8	144.0
Laser pulse duration τ_{laser} [fs]	119.4	84.9	64.7	56.0	35.4	25.0	20.4	17.7	11.2	7.9	5.6
Beam power P_{beam} [MW]	0.2	0.3	0.4	0.4	0.7	1.0	1.2	1.4	2.2	3.1	4.3
Beamstrahlung parameter Υ	34.5	24.6	18.7	16.2	10.2	7.2	5.9	5.1	3.2	2.3	1.6
No. of Beamstrahlung photons n_γ	5.2	4.1	3.4	3.1	2.2	1.7	1.5	1.3	0.9	0.7	0.5
Beamstrahlung energy spread δ_E	1.44	1.11	0.90	0.80	0.55	0.40	0.34	0.29	0.19	0.13	0.09
Coherent Beamstrahlung pairs n_b	1.42e-1	7.20e-2	4.17e-2	3.13e-2	1.25e-2	6.26e-3	4.17e-3	3.13e-3	1.25e-3	6.26e-4	3.13e-4
Trident Cascade pairs n_ν	1.19e-1	8.48e-2	6.46e-2	5.59e-2	3.54e-2	2.50e-2	2.04e-2	1.77e-2	1.12e-2	7.91e-3	5.59e-3
Length of single stage L_{stage} [m]	9.7	3.5	1.5	1.0	0.3	0.1	0.049	0.032	0.008	0.003	0.001
Total linac length (1 arm) [m]											
L_{stage} for coupling	19.4	13.9	12.3	10.0	6.1	4.1	3.3	2.8	1.8	1.3	0.9
0 m for coupling	9.7	7.0	6.2	5.0	3.0	2.1	1.7	1.4	0.9	0.6	0.5
5 m for coupling	14.7	17.0	26.2	30.0	63.0	117.1	171.7	226.4	565.9	1125.6	2250.5
10 m for coupling	19.7	27.0	46.2	55.0	123.0	232.1	341.7	451.4	1130.9	2250.6	4500.5
25 m for coupling	34.7	57.0	106.2	130.0	303.0	577.1	851.7	1126.4	2825.9	5625.6	11250.5

Table 4.5: Parameter scan for a possible Z-factory, based on the parameters and scalings in [21]. The final energy per arm is $E_b \approx 45\,\text{GeV}$ ($m_Z \approx 91.2\,\text{GeV/c}^2$, $m_W \approx 80.4\,\text{GeV/c}^2$). The initial scaling assumes a luminosity $\mathcal{L} = 2 \cdot 10^{34}\,\text{cm}^{-2}\text{s}^{-1}$, for a beam size at the IP $\sigma_x^* = \sigma_y^* = 10\,\text{nm}$ and a bunch length $\sigma_z = 1\,\mu\text{m}$. The assumed laser wavelength is $1\,\mu\text{m}$. Following the scaling [64] $\mathcal{L}[10^{34}\,\text{cm}^{-2}\text{s}^{-1}] \approx E[\text{TeV}]^2$, the minimal useful collision frequency f_{min} for a Z-facility could be reduced by a factor $(1000/90)^2 \approx 125$, resulting in a reduction in beam power by the same amount. Parameters related to beam-beam interaction have been calculated using the equations given in chapter 4.1.2, under the pessimistic approximation that $\Xi(\Upsilon) = \Omega(\Upsilon) = 10^{-1}$. Note that an average energy loss due to beamstrahlung $\delta_E > 1$ is of course not physical. It means that for the parameter range investigated here, the assumptions made in the derivation of Υ, n_γ and δ_E are not valid any more. None the less, one can conclude that beamstrahlung will be severe.

Plasma electron density n_0 [cm^{-3}]	7.6e15	2.3e16	5.0e16	7.5e16	1.0e17	2.5e17	5.0e17	7.5e17	1.0e18	2.5e18	5.0e18	1.0e19
Particles per bunch N_{bunch} [1e9]	14.5	8.3	5.7	4.6	4.0	2.5	1.8	1.5	1.3	0.8	0.6	0.4
Energy gain per stage W_{stage} [GeV]	131.6	43.5	20.0	13.3	10.0	4.0	2.0	1.3	1.0	0.4	0.2	0.1
Number of stages N_{stages}	1	3	7	10	13	33	65	98	130	325	650	1300
Laser energy per stage U_L [J]	1527.3	290.1	90.5	49.3	32.0	8.1	2.9	1.6	1.0	0.3	0.1	0.03
Avg laser power per stage P_{avg} [kW]	1741.1	1000.9	678.8	554.3	480.0	303.6	214.7	175.3	151.8	96.0	67.9	48.0
Collision frequency f [kHz]	1.14	3.45	7.5	11.25	15	37.5	75	112.5	150	375	750	1500
Min. collision frequency f_{min} [kHz]	0.077	0.23	0.50	0.76	1.0	2.5	5.1	7.6	10	25	51	100
Total wall-plug power P_{wall} [MW]	11.5	20.0	29.4	36.0	41.6	65.8	93.0	113.9	131.6	208.0	294.2	416.0
Laser pulse duration τ_{laser} [fs]	203.1	116.8	79.2	64.7	56.0	35.4	25.0	20.4	17.7	11.2	7.9	5.6
Beam power P_{beam} [MW]	0.3	0.6	0.9	1.1	1.2	2.0	2.8	3.4	3.9	6.2	8.8	12.5
Beamstrahlung parameter Υ	169.8	97.6	66.2	54.0	46.8	29.6	20.9	17.1	14.8	9.4	6.6	4.7
No. of Beamstrahlung photons n_γ	5.4	3.7	2.8	2.5	2.2	1.6	1.3	1.1	1.0	0.7	0.6	0.4
Beamstrahlung energy spread δ_E	1.58	1.07	0.81	0.70	0.63	0.44	0.34	0.29	0.26	0.17	0.13	0.09
Coherent Beamstrahlung pairs n_b	4.12e-1	1.36e-1	6.26e-2	4.17e-2	3.13e-2	1.25e-2	6.26e-3	4.17e-3	3.13e-3	1.25e-3	6.26e-4	3.13e-4
Trident Cascade pairs n_ν	2.03e-1	1.17e-1	7.91e-2	6.46e-2	5.59e-2	3.54e-2	2.50e-2	2.04e-2	1.77e-2	1.12e-2	7.91e-3	5.59e-3
Length of single stage L_{stage} [m]	47.7	9.1	2.8	1.5	1.0	0.3	0.1	0.049	0.032	0.008	0.003	0.001
Total linac length (1 arm) [m]												
$\quad L_{stage}$ for coupling	95.5	54.4	39.6	30.8	26.0	16.7	11.6	9.5	8.2	5.2	3.7	2.6
$\quad$0 m for coupling	47.7	27.2	19.8	15.4	13.0	8.3	5.8	4.8	4.1	2.6	1.8	1.3
$\quad$5 m for coupling	52.7	42.2	54.8	65.4	78.0	173.3	330.8	494.8	654.1	1627.6	3251.8	6501.3
$\quad$10 m for coupling	57.7	57.2	89.8	115.4	143.0	338.3	655.8	984.8	1304.1	3252.6	6501.8	13001.3
$\quad$25 m for coupling	72.7	102.2	194.8	265.4	338.0	833.3	1630.8	2454.8	3254.1	8127.6	16251.8	32501.3

Table 4.6: Parameter scan for a possible *H-factory*, based on the parameters and scalings in [21]. The final energy per arm is $E_b \approx 130\,\text{GeV}$ ($m_H \approx 125\,\text{GeV}/c^2$). The initial scaling assumes a luminosity $\mathcal{L} = 2 \cdot 10^{34}\,\text{cm}^{-2}\text{s}^{-1}$, for a beam size at the IP $\sigma_x^* = \sigma_y^* = 10\,\text{nm}$ and a bunch length $\sigma_z = 1\,\mu\text{m}$. The assumed laser wavelength is $1\,\mu\text{m}$. Following the scaling [64] $\mathcal{L}[10^{34}\,\text{cm}^{-2}\text{s}^{-1}] \approx E[\text{TeV}]^2$, the minimal useful collision frequency f_{min} for a *H-facility* could be reduced by a factor $(1000/260)^2 \approx 15$, resulting in a reduction in beam power by the same amount. Parameters related to beam-beam interaction have been calculated using the equations given in chapter 4.1.2, under the pessimistic approximation that $\Xi(\Upsilon) = \Omega(\Upsilon) = 10^{-1}$. Note that an average energy loss due to beamstrahlung $\delta_E > 1$ is of course not physical. It means that for the parameter range investigated here, the assumptions made in the derivation of Υ, n_γ and δ_E are not valid any more. Non the less, one can conclude that beamstrahlung will be severe.

As the production rates for W-bosons pairs are about 10-20 times higher than in comparable e^+e^--colliders [169], a centre of mass energy slightly above 160 GeV has been chosen. As the energy spectrum of the created photons peaks at about 80 % of the driving electron beam energy [168, 171, 172], this requires an electron beam energy of $E_b \approx 100$ GeV per beam. This could be achieved with four 25 GeV stages as described in [109, 140], for which high beam quality has been shown in simulations. There, a plasma electron density $n_0 = 5.66 \cdot 10^{16}$ cm^{-3} has been chosen, based on the capabilities of current day state of the art injectors and the condition that the separation between drive and witness bunch should be less then one plasma wave length in order to have both bunches at the appropriate phase of the wake.

Let us consider a witness bunch population of $N = 1.73 \cdot 10^{10}$ electrons as used in the simulations in [140], a geometric luminosity $\mathcal{L} = 1 \cdot 10^{34}$ cm^{-2}s^{-1} and a spot size at the IP comparable to those considered for ILC [5] (the generated photons are scattered in the direction of electron propagation, therefore focusing the photons means focusing the electron beams). This leads to a required collision frequency $f \approx 7$ kHz and a power per beam $P_b = E_b N f \approx 2.3$ MW, corresponding to a stored energy per bunch of $W_b = E_b N \approx 330$ J. Assuming a energy transfer efficiency from the wall plug to the drive beam of 45 % [147] using a heavily loaded linac and a transfer efficiency of 51 % from the drive to the witness bunch [140], this leads to a total power consumption per main linac of approximately 12 MW. (Note that the simulations in [140] assume a wedge shaped density profile for both drive and witness bunch. For Gaussian beams, a lower transfer efficiency of about 35 % has been estimated in [147], resulting in a total power consumption of about 15 MW.)

As discussed in chapter 4.5 (page 60), the required wavelength of the scattering laser would be λ_L [μm] $\approx 4 E_b$ [TeV] $\approx 4 * 0.1 \approx 0.4$ μm. This can for example be achieved by frequency doubling a 800 nm infrared laser. Assuming a scattering angle $\theta \ll 1$ ($\cos^2 \theta \simeq 1$) and $E_b = 100$ GeV, one gets $x \approx (4 E_b \hbar \omega_L / (m_e^2 c^4)) \cos^2(\theta/2) \approx 4.8$, resulting in $a_0 < 2/x \approx 0.4$ and a required laser power at $\lambda_L = 400$ nm of $U_{L, blue} \approx (2/a_L^2) E_b$ [TeV] ≈ 1.1 J. Given a conversion efficiency for the frequency doubler of about 50 % [33, 177], this results in a IR laser power of $U_{L, IR} \approx 2.2$ J. This would result in a maximal photon energy of $\hbar \omega = E_b x / (1 + x + a_L^2) \approx 80$ GeV, enough to create a possible Higgs boson with a mass of about 125 GeV/c^2, as well as W boson pairs.

For comparison, the status of current-day high-power laser systems is given in chapter 3.1.2. The top level parameters of the collider proposal developed above are summarized in table 4.7.

Discussion

I have derived the straw-man collider above to make best use of the intriguing properties of acceleration in the bubble regime. A challenge that is not discussed is the longitudinal polarization of the electron beam, which is practically mandatory for a useful photon collider, as the $\gamma\gamma$ luminosity would decrease by a factor of four for unpolarized beams [168, 171]. Whilst simulations predict fairly low depolarization rates for acceleration in the bubble regime [178], the generation of said beams would require the use of a conventional electron gun and the use of damping rings, which would in turn increase the size, cost and power

Geometrical e^-e^- luminosity $\mathcal{L}$ in cm^{-2}s^{-1}	$1 \cdot 10^{34}$
Hor. e^--beam size at IP σ_x^* in nm	474
Vert. e^--beam size at IP σ_y^* in nm	3.5
Highest photon energy in GeV	80
Final electron beam energy E_b in GeV	100
Number of acceleration stages per beam	4
Energy gain per stage in GeV	25
Plasma length per stage in m	0.6
Plasma electron density n_0 in 10^{16} cm^{-3}	5.6
Number electrons drive beam in 10^{10}	4.4
Bunch length drive beam in μm	58
Bunch length witness beam in μm	22
Number electrons witness beam in 10^{10}	1.7
Collision frequency f in kHz	7
Beam power witness beam in MW	2.8
Energy scattering laser per shot in J	2.2
Energy transfer efficiency wall plug to e^--beam in %	23
Total wall-plug power both linacs in MW	24.4

Table 4.7: Example parameters for a 160 GeV centre of mass $\gamma\gamma$-collider based on PWFA in the blowout regime. Parameters of the acceleration stages are based on simulation results in [140]. The geometrical luminosity and the beam size at the interaction point (IP) give the values that would be reached if no laser pulse would be scattered at the electron beams. The generated photons are scattered in the propagation direction of the electron beam, therefore focusing the photons means focusing the electrons, as discussed in chapter 4.5, page 60. The total footprint of the facility depends on the distance needed between the stages for coupling in the witness bunch and the new drive beam. It can be estimated to be a few 100 m. Compare to tables 4.4 and 4.6 for collider estimated based on ILC / LWFA technology.

consumption of the facility significantly. In addition, note that the e^--beam sizes at the IP are sizes envisaged for the ILC and very challenging. Not reaching these parameters would result in a reduction in luminosity (or an increase in beam power to keep up the luminosity). Also, the simulations in [140] assume a triangular charge density modulation of both the drive and witness bunch to reduce the beam loading induced energy spread, which might be challenging to achieve for the bunch lengths discussed.

The most important drawback of this design however, is that it would delay the start of a e^+e^- collider by several years. Since such a 250 GeV collider would have a stronger physics case at an increased cost of about 30 %, support from the High Energy Physics community is doubtable (The idea of a Higgs factory $\gamma\gamma$ collider based on ILC technology has been discarded for the afore mentioned reasons [168]). If the collider were to operate in the linear regime to accelerate positrons, the achievable bunch lengths of drive and witness bunch would make it necessary to operate at a comparably low plasma density. This in turn would result in an even higher charge per bunch than for the laser-based collider discussed in the previous section and even higher beamstrahlung losses.

4.7.6 Evaluation

In the previous sections, I have developed and studied several ideas for building a Higgs facility based on novel acceleration methods. One question common to all these proposals, which has been excluded in the scope of this work, is the availability of a suitable injector. Among others, questions to be addressed here are i) Polarization of beams ii) Beam emittance (to allow to focus to the required spot sizes at the IP) iii) Bunch shaping and iV) Charge and bunch length requirements. The last of these questions is addressed in chapter 3.1.1. For conventional accelerators, meeting the before mentioned challenges requires large damping rings to decrease the beam emittance and large beam energies to allow for the compression to small bunch lengths (See, e.g. [5, 6, 168]).

Normalizing to the same luminosity and beam energy, very comparable total power consumptions are calculated for both the beam and the laser driven technology. Assuming that the total power consumption scales linearly with beam energy and luminosity (which is not exactly true if damping rings are required), it is also very similar to the power consumption estimated for ILC technology.

Obviously, the discussed proposals are just rough estimates and far from a finished design. But they do illustrate how novel acceleration methods could be used to reduce the footprint of a Higgs facility to a few kilometres (including the final focus system and still to be developed injectors). Many of the key issues for the development of a working linear collider are actively researched and will be investigated in the coming years at facilities like BELLA and FACET [109, 160].

5. Possible Mid-Term Applications

The technology necessary for the Linerar Collider proposals discussed in chapter 4 will still take decades to mature. Therefore, this chapter investigates possibilities for an earlier technical application of plasma-based acceleration methods, in particular the application to synchrotron light sources.

In chapter 5.1, the achieved LWFA beam parameters described in more detail in chapter 3.1.1 are compared to the requirements of so-called Free Electron Lasers (FEL) - synchrotron radiation sources based on linear accelerators.

As the repetition rates of current-day high-power laser systems are still too low to drive an FEL with high average photon flux, chapter 5.2, investigates LWFA as injectors for light sources based on storage rings. This would allow to combine the interesting radiation properties resulting from the short bunch length customary to LWFA with the high repetition rate of electron bunches stored in a ring.

5.1 Free Electron Laser

Many practical application from material and environmental science to biology and medical treatments utilize Synchrotron radiation. Free Electron Laser (FEL) complement storage ring based light sources by offering highest peak powers and shortest pulse durations. The emitted radiation normally has a very narrow bandwidth and is tunable over a wide parameter range. (E.g. FERMI@Elettra can produce radiation with a wavelength between 10 nm and 100 nm [179]). The beam energy and source size of the generated radiation depend strongly on the electron beam energy and emittance. An additional figure of merit for a FEL is a high peak current at the undulator, determining the amount of radiation generated. Top level parameters of exemplary FEL are given in table 5.1.

Plasma based acceleration techniques, with their intrinsically short bunch lengths, achieve peak currents very comparable to those of the conventional accelerators listed in table 5.1, cf. chapter 3.1.1. It is hoped that they will allow the construction of much smaller and cheaper facilities, as compared to the kilometre scales of current day FEL.

Facility	FERMI	SwissFEL	XFEL	LCLS
Beam Energy [GeV]	1.2-1.7	2.1-5.8	17.5-20.0	14.4
Energy Spread [keV]	100 - 250	250-350	1000	2900
Charge per Pulse [nC]	0.8-1.0	0.2	1.0	1.0
Bunch length [fs]	400	6-30	70	70
Repetition Rate [Hz]	10-50	200	10	120
Normalized beam emittance [μm $\cdot$ rad]	0.8-2	0.18-0.43	1.4	1.2

Table 5.1: Design parameters of exemplary linac based Free Electron Lasers (FEL): Free Electron Laser for Multidisciplinary Investigations (FERMI@Elettra) at Elettra, Italy [111, 179]; SwissFEL at PSI, Switzerland [108, 180, 181]; Linac Coherent Light Source (LCLS) at SLAC, USA [106]; and the European X-Ray Free Electron Laser (XFEL) at DESY, Germany [110, 182]. The power consumption of the facilities mentioned above is in the order of a few MW. For SwissFEL, a shortening of the bunch length to 0.6 fs is foreseen in the upgrade plans.

5.1.1 Choice of Driver Technology

For FEL applications, electron beam energies in the GeV range are required. This makes protons inappropriate as drivers, as for these energies their relativistic gamma factor is in the order of $\mathcal{O}(1)$. This leads to significant dephasing with the ultra relativistic electrons, as explained in more detail in chapter 4.7.2.

For electrons, dephasing would not be a problem, due to the much higher γ-factor of the driver. However, due to the transformer ratio described in chapter 2.6.2, an electron driver would need to have about half the desired final energy and a bunch charge similar to the witness bunch to avoid the necessity for staging.

Laser driven acceleration methods are therefore regarded as most beneficial for this application, as fs drive laser pulses allow for ultra short electron pulses with very high peak currents, which is desirable for the radiation characteristics of the bunch (cf. e.g. [7]). They have the added benefit that parts of the laser could be uncoupled to use in pump-probe experiments, with comparably easy synchronization.

Within the coming decades, lasers capable of accelerating sufficient numbers of electrons to the interesting energy scale with high enough repetition rates should become available [11, 117, 120, 128, 129]. Given the energy envisaged, this points towards a single acceleration stage with high charge per bunch. As neither staging nor positrons are required, this points to acceleration in the blowout regime.

5.1.2 Possible LWFA Parameters

An introduction to achieved LWFA beam parameters can be found in chapter 3.1.1. In particular, cf. table 3.1 and figure 3.1, pages 35 and 34 respectively. Three of the parameter sets closest to the requirements for FEL application are repeated in table 5.2.

It is important to point out that these parameters often refer to the quasi mono energetic peak of the particle distribution. Complete energy distributions are illustrated in figures 3.4 and 5.2, pages 42 and 79 respectively. This means that a large number of

Electron Mean Energy [MeV]	170	1000	198
Bunch Charge [pC]	500	30	10
Laser Pulse Energy [J]	1.0	1.7	0.85
Laser Pulse Length [fs]	13	16	18

Table 5.2: Achieved LWFA beam parameters [10, 42, 100], subset of table 3.1, page 35. The pulse length was not measured for all experiments, but can be expected to be comparable to the laser pulse length.

particles with the wrong energy would have to be energy collimated, which could lead to radiation protection issues. However, it is also important to point out that huge efforts are undertaken to reduce the energy spread of LWFA generated beams. In particular, several injection control methods are investigated, which could stop the continuous injection of background electrons into the bubble (thereby removing the unwanted low energetic part of the energy spectrum), cf. e.g. [94, 183–187]

As the bunch charges and bunch energies required for FEL application have not yet been achieved experimentally, table 5.3 list possible beam parameters observed in simulations for acceleration in the bubble regime [32].

Beam energy $\gamma m_e c^2$ [GeV]	0.99	1.06	9.9	10.2
Plasma density n_0 [$10^{17}\,\mathrm{cm}^{-3}$]	10	20	1	3
Charge per bunch [nC]	0.18	0.40	0.57	1.8
Laser energy U_L [J]	0.6	3.2	21	212
Laser pulse duration τ_L [fs]	30	30	100	100
Stage length [m]	0.016	0.009	0.52	0.18

Table 5.3: Example parameters for $\sim$1 GeV / $\sim$10 GeV energy LWFA operating in the blowout regime, as simulated in [32] (cf. table 5.2 therein). The first parameter set for a given beam energy assume external injection and external guiding, matching the laser power and the plasma density to that $P_L/P_c = 1$, cf. chapter 2.5.4. The second parameter set assumes self injection and self guiding, resulting in a significantly higher required laser energy.

For comparison, acceleration in the linear regime has also been studied by scaling the example parameters in [21]. The main accelerator parameters are given in table 5.4. Note that the used scalings and parameters assume a transverse and longitudinal plasma density shaping to minimize the evolution of the laser pulse as well as a triangular charge density distribution of the electron bunch to minimize its energy spread due to beam loading (cf. chapter 2.9.1)! This beam and plasma shaping could be circumvented by accelerating a higher than necessary charge and then energy collimating the beam. Also, undulators capable of handling the larger energy spread typical for LWFA are actively being researched [188, 189].

Beam energy $\gamma m_e c^2$ [GeV]	1.7	5	20
Plasma density n_0 [10^{17} cm^{-3}]	6	2	0.5
Charge per bunch [nC]	0.3	0.5	0.9
Repetition rate f [Hz]	50	200	10
Laser energy U_L [J]	2	11	91
Laser pulse duration τ_L [fs]	23	40	79
Average laser power P_{avg} [W]	100	220	910
Stage length [m]	0.1	0.4	2.8

Table 5.4: Example parameters for LWFA FEL linacs operating in the linear regime. Parameters are based on the example parameters and scalings in [21] (Cf. tables 4.1 and 4.2, page 53). The bunch length $\sigma_z = 1\,\mu$m is independent of the plasma density for this density range. For the calculation of the required average laser power P_{avg}, the repetition rates have been chosen to match those of the corresponding facility of the same beam energy (cf. table 5.1). The necessary laser parameters are not far beyond the current state of the art, and could become available within the next decade (cf. chapter 3.1.2). However, the necessary stability has still to be demonstrated. Note that the used scalings and parameters assume a transverse and longitudinal plasma density shaping to minimize the evolution of the laser pulse as well as a triangular charge density distribution of the electron bunch to minimize its energy spread due to beam loading (cf. chapter 2.9.1)! Also, note that with operation in the linear regime, one still needs a conventional or laser based electron injector, capable of supplying electron bunches with sufficiently high charge and sufficiently low emittance. Demonstration of a 10 GeV stage operating in the linear regime is a stated goal of the recently commissioned BELLA facility [121, 160].

5.1.3 Discussion

Up until now, LWFA have not yet reached the beam energy and bunch charge requirements of current day FEL. However, with more powerful laser systems like the recently completed BELLA facility [121, 160] and the funded ELI project [117, 190], this is likely to change in the near future. On the other hand, reaching the required beam quality and reproducibility still requires serious research and development [11]. To allow for an earlier application, a lower energy LWFA as injector for a storage ring based Synchrotron light source is discussed in chapter 5.2.

5.2   LWFA as Injector for ANKA

As discussed in section 5.1, LWFA are not yet ready to drive Free Electron Laser. To allow for an earlier technical application, I have studied to possibility to use LWFA as injectors for rings-based light sources. As illustrated in figure 5.1, this would allow to drastically increase the frequency of radiation production - from the repetition frequency of the laser system to the revolution frequency of the ring.
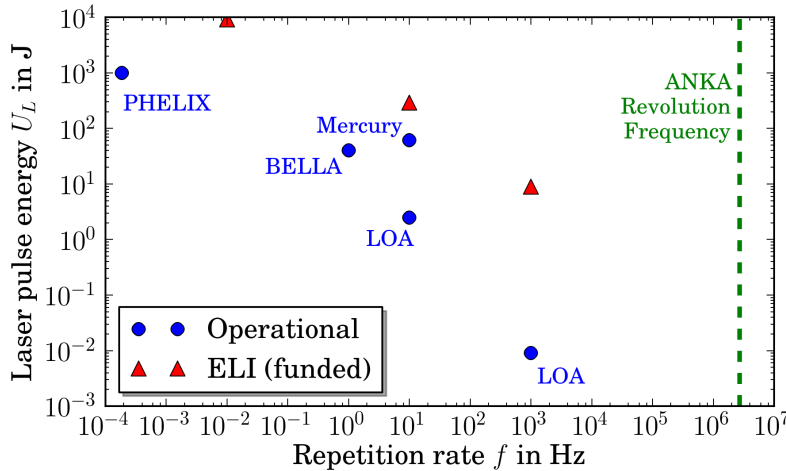
Figure 5.1: Laser pulse energy over repetition rate for several of the laser systems introduces in chapter 3.1.2. Storing the LWFA-generated electron bunches in a ring would allow to produce radiation with the revolution frequency of the ring, 2.3 MHz for ANKA. For the following study, a laser comparable to the 2.5 J, 10 Hz LOA laser is assumed. For this case, storing the electron beam in a ring would increase the frequency of radiation production by 6 orders of magnitude.

In addition to their high beam energies and small facility footprint, Laser Wakefield Accelerators (LWFA) have two more properties that would make them very interesting as injectors for synchrotron light sources:

- The length of the generated synchrotron radiation pulse is directly proportional to the length of the emitting electron bunch. LWFA beams would therefore allow the reduction of the length of the radiation pulses by several orders of magnitude, allowing studies of processes on a much faster time scale.

- Many important questions from solid state physics to biological applications demand an analysis within a wide spectral range from THz to infrared. Despite the importance of this spectral range, there is a lack of sources that can cover it with high intensity. A conceptually simple idea is to compress the length of an electron bunch to below the wavelength of the desired radiation. For these wavelengths, this results in coherent amplification of the emitted synchrotron radiation in a magnetic field [191]. Unfortunately, pushing the radiation spectrum of this Coherent Synchrotron Radiation (CSR) far into the THz region requires bunch lengths in the order of a few fs, much shorter than what is achievable with current day Synchrotrons and conventional injectors.

Furthermore, electron storage rings have the added benefit that due to radiative damping, the bunches converge towards the equilibrium energy spread. For the ANKA Synchrotron light source [191], the typical time scale for this process is a few tens of ms, depending on the beam energy and the optics used. As the initial energy spread becomes irrelevant for the stored electrons, this could serve as a first technical application of LWFA.

Using ANKA as an example, I have studied the possibility of injecting and storing LWFA generated bunches in an electron storage ring. The work is based on 3D particle in cell simulations by Oliver Jansen, using VLPL [192]. The input parameters are given in Table 5.5. They are comparable to the parameters of current day laser systems discussed in chapter 3.1.2. The resulting longitudinal electron energy distribution is shown in Fig. 5.2.

Plasma density n_0 in cm^{-3}	9×10^{18}
Laser wavelength λ_L in nm	800
RMS Laser pulse duration τ_L in fs	13
RMS Laser radius at focus r_L in nm	720
Laser pulse energy E_L in J	4.6

Table 5.5: VLPL [192] input parameters

The ANKA lattice used for this study has an energy acceptance $\Delta E/E_0 \approx \pm 1\,\%$, indicated by the solid area. Discarding all particles outside this energy window, the resulting beam parameters are given in Table 5.6, calculated via equations 7.2 to 7.8 (see appendix C.1). The resulting bunch charge for different energy windows is given in Table 5.7. Note that despite the small emittance, the very small beam size leads to very large divergence angles. To ensure that these large angles are not due to some conversion error, they have also been confirmed using hdfview [193] - a program dedicated to the treatment of hdf files.
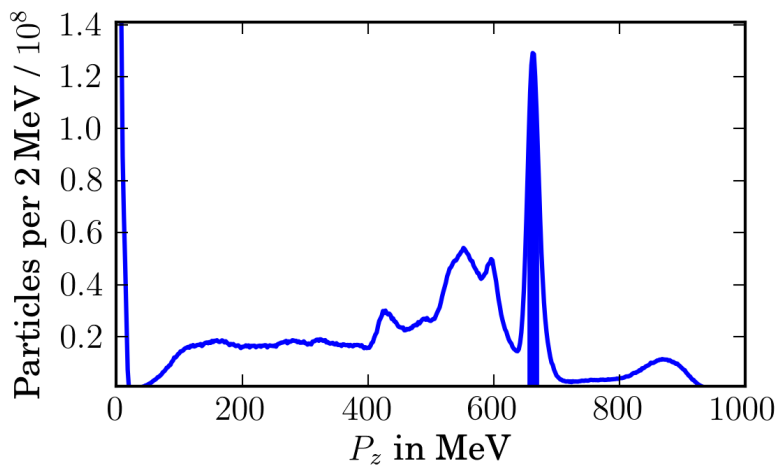
Figure 5.2: Longitudinal energy distribution of LWFA generated electrons. The energy acceptance of the ANKA lattice used is indicated by the solid area. Also published in [194, 195].

Central energy p_0 in MeV	662
Applied energy cut in MeV	655 - 669
RMS energy spread δ in %	0.5
Bunch charge q in pC	160
Number of particles N	1.0×10^9
Geometric emittance ϵ_{geo} in m $\times$ rad	$1.8 \cdot 10^{-8}$
Normalized emittance ϵ_{norm} in m $\times$ rad	$2.3 \cdot 10^{-5}$
RMS Bunch length σ_z in μm	1.1
RMS Bunch length σ_z in fs	3.7
RMS Bunch radius σ_r in μm	1.6
RMS Divergence in rad	0.01
Twiss $\alpha_x = \alpha_y$	0.0
Twiss $\beta_x = \beta_y$ in m	1.4×10^{-4}

Table 5.6: LWFA e^--beam parameters after discarding all particles with longitudinal momentum outside the range $662\,\text{MeV} \pm 1\,\%$. For up to a few percent, a larger allowed deviation in energy leads to a larger bunch charge, whilst the influence on the other beam parameters is negligible. However, particles outside the energy acceptance of the ANKA storage ring will get lost within only a few turns. The resulting bunch charge for different energy windows is given in Table 5.7.

Max. energy deviation	100 %	10 %	5 %	3 %	0.25 %
Bunch charge q in pC	24000	370	270	240	61
Number of particles N	$1.5 \cdot 10^{11}$	$2.3 \cdot 10^9$	$1.7 \cdot 10^9$	$1.5 \cdot 10^9$	$3.8 \cdot 10^8$

Table 5.7: The resulting bunch charge for different energy windows, cf. fig. 5.2. Note that for an allowed energy deviation of over $1\,\%$, most particles get lost within only a few turns, cf. fig. 5.4.

5.2.1 Transfer Line to ANKA

The initially round beam beam described in Table 5.6 has to be matched to the flat beam parameters accepted by the ANKA storage ring, listed in Table 5.8. Using MAD-X [196], a solution has been found using pulsed quadrupoles [197]. These quadrupoles offer a field strength of about $1400\,\text{T/m}$, significantly higher than conventional quadrupoles. However, due to their pulsed nature, the injection would be limited to 1 pulse every few seconds. The exemplary transfer line is shown in Fig. 5.3. It has not been studied in detail yet, as the main focus of this work is the behaviour of these short bunches in a storage ring. The challenges associated with the coupling of LWFA beams with conventional accelerators have been studied in more detail e.g. by [189, 198]. For now we will assume that a suitable transfer solution can be found. Note that in our exemplary transfer line, the chromaticity has not been corrected. This means that particles with different energies get focused differently and therefore travel on different trajectories This leads to a significant lengthening of the initially ultra short bunch, observable in the first plot in figures 5.4 and 5.5. For $\Delta p_{max}/p_0 = 0.01$, the bunch length increases to $\sigma_z \approx 4.7\,\text{mm}$ during the passage through the transfer line, i.e. by 3 orders of magnitude! The effect is even stronger for a higher initial energy spread.

Horizontal beta β_x in m	16.6
Vertical beta β_y in m	6.5
Horizontal alpha α_x	-0.03
Vertical alpha α_y	-0.07

Table 5.8: ANKA Twiss Parameters at injection point

5.2.2 Behaviour in Synchrotron - Longitudinal

Naively, one might assume that the lengthening of the initially short LWFA bunch happens on a time scale given by the radiative damping time. For the ANKA lattice at $662\,\text{MeV}$ studied here, this would correspond to approximately $80\,\text{ms}$ (approximately $200\,000$ turns). If a LWFA would be used as a full energy injector (for this energy), this could have been sufficient for dedicated user operation. Unfortunately, simulations using the Accelerator Toolbox for Matlab [200] show that the initially short bunch lengthens much faster, to a bunch length of a few cm within only a few turns. This can be understood by looking at the momentum compaction factor

$$\alpha_c = \frac{1}{L} \times \oint \frac{D(s)}{\rho(s)} ds, \tag{5.1}$$

the integral over the dispersion D along the ring. Via the relation

$$\alpha_c \frac{\Delta p}{p_0} = \frac{\Delta L}{L} \tag{5.2}$$

it gives the path length difference ΔL per revolution for a particle of energy deviation Δp [191]. ANKA has a circumference $L = 110.4\,\text{m}$. Depending on the optic used, the momentum compaction factor is in the order of $10^{-4} < \alpha_c < 10^{-2}$. Due to its larger
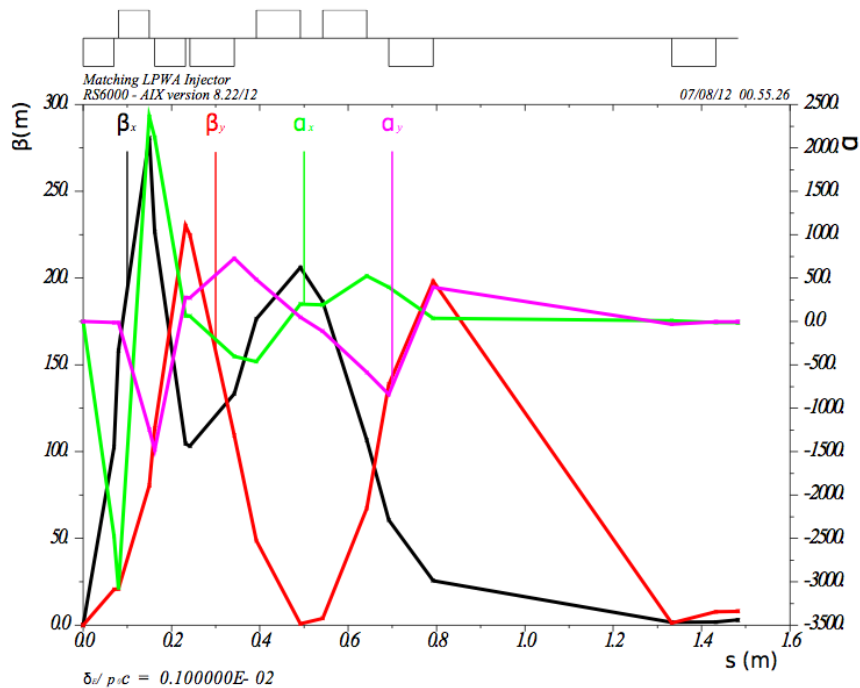
Figure 5.3: Exemplary transfer line, matching the LWFA generated bunches to the ANKA storage ring [199]. Note that the chromaticity has not been corrected, leading to a significant lengthening of the ultra-short bunches. Also published in [194, 195].

momentum acceptance, I used the ANKA injection optics for my studies, resulting in a larger α_c. For the particles with the maximal investigated energy deviation $\Delta p/p_0 = 0.01$, this results in a path length difference of $1\,\text{cm} \lesssim \Delta L \lesssim 100\,\mu\text{m}$ or $30\,\text{ps} \lesssim \Delta L/c_0 \lesssim 300\,\text{fs}$ respectively - much more than the initial $1.1\,\mu\text{m}$! The bunch quickly expands to the maximal acceptance of the RF system, reaching it after about 25 turns. Then, it starts to converge back towards the equilibrium bunch length of the lattice. The process is illustrated in Fig. 5.4 and Fig. 5.5. The parameters of the ANKA lattice used are given in Table 5.9. It is important to point out that for the short bunches studied here, this lengthening is basically independent of the initial bunch length. This is due to the fact that the energy dependent path length difference (about $1\,\text{cm}$ per revolution) calculated via equation 5.2 exceeds the initial bunch length of $1.1\,\mu\text{m}$ from the LWFA by three orders of magnitude.

AT does not take the effects of space charge and radiative interaction within the beam into account. Both of them should result in an even faster lengthening of the bunch.

For a non-Gaussian charge density distribution along the bunch, sharp features can also lead to coherent emission of radiation. Figure 5.6 illustrated the evolution of the longitudinal charge density corresponding to the phase space evolution displayed in fig. 5.4. Sharp features are apparent. However, to be useful for practical application, the evolution of the longitudinal charge density has to be reproducible. This would have to be investigated further, including CSR effects.
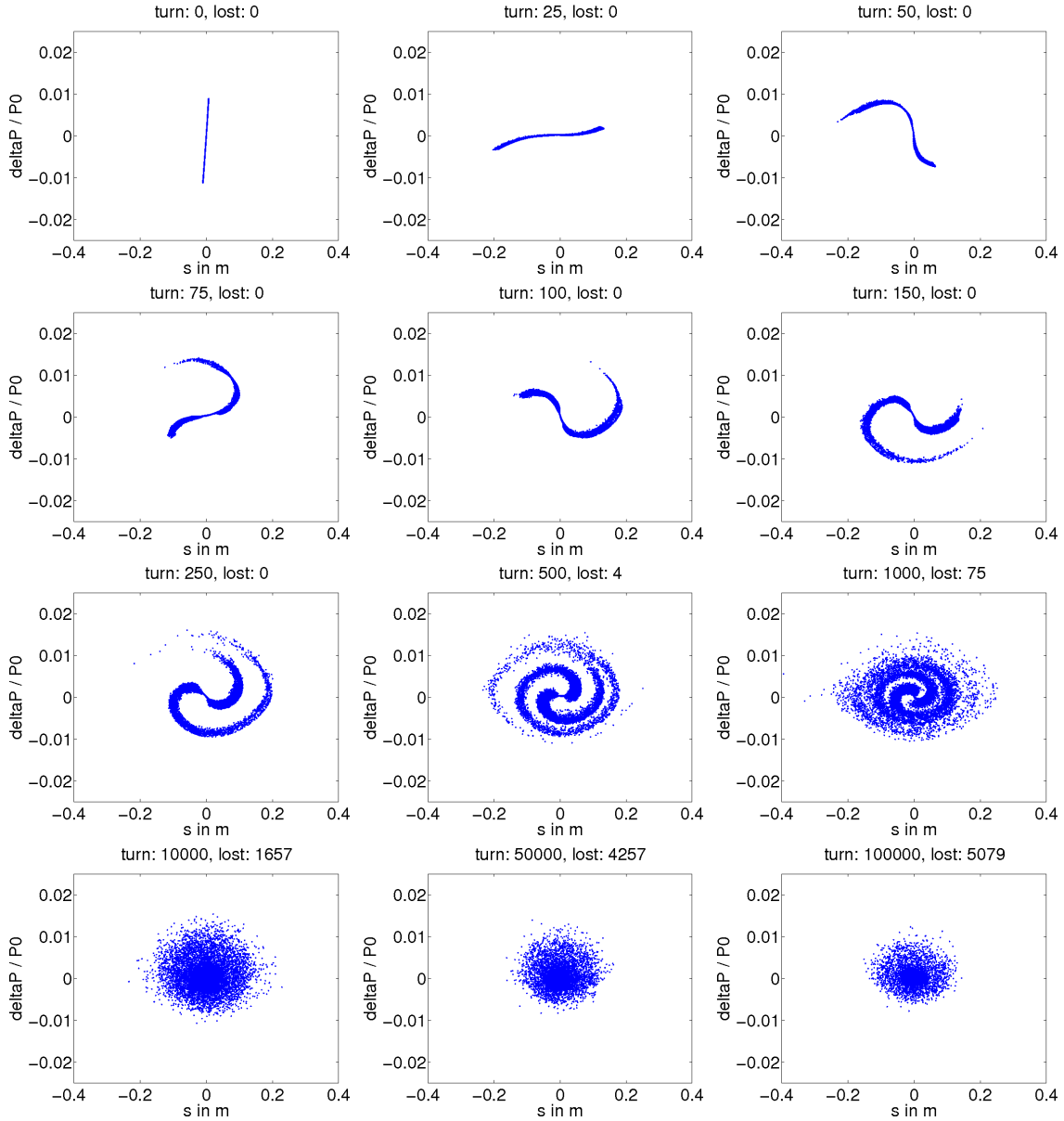
Figure 5.4: Top left to bottom right: Evolution of longitudinal phase space (normalized deviation from reference energy over position along bunch) for a maximal initial energy deviation $\Delta p_{max}/p_0 = 0.01$ and 10^4 simulated particles. The change in longitudinal position is consistent with Synchrotron oscillations. Transverse losses to the beam pipe have been neglected for this study. Also published in [194, 195].
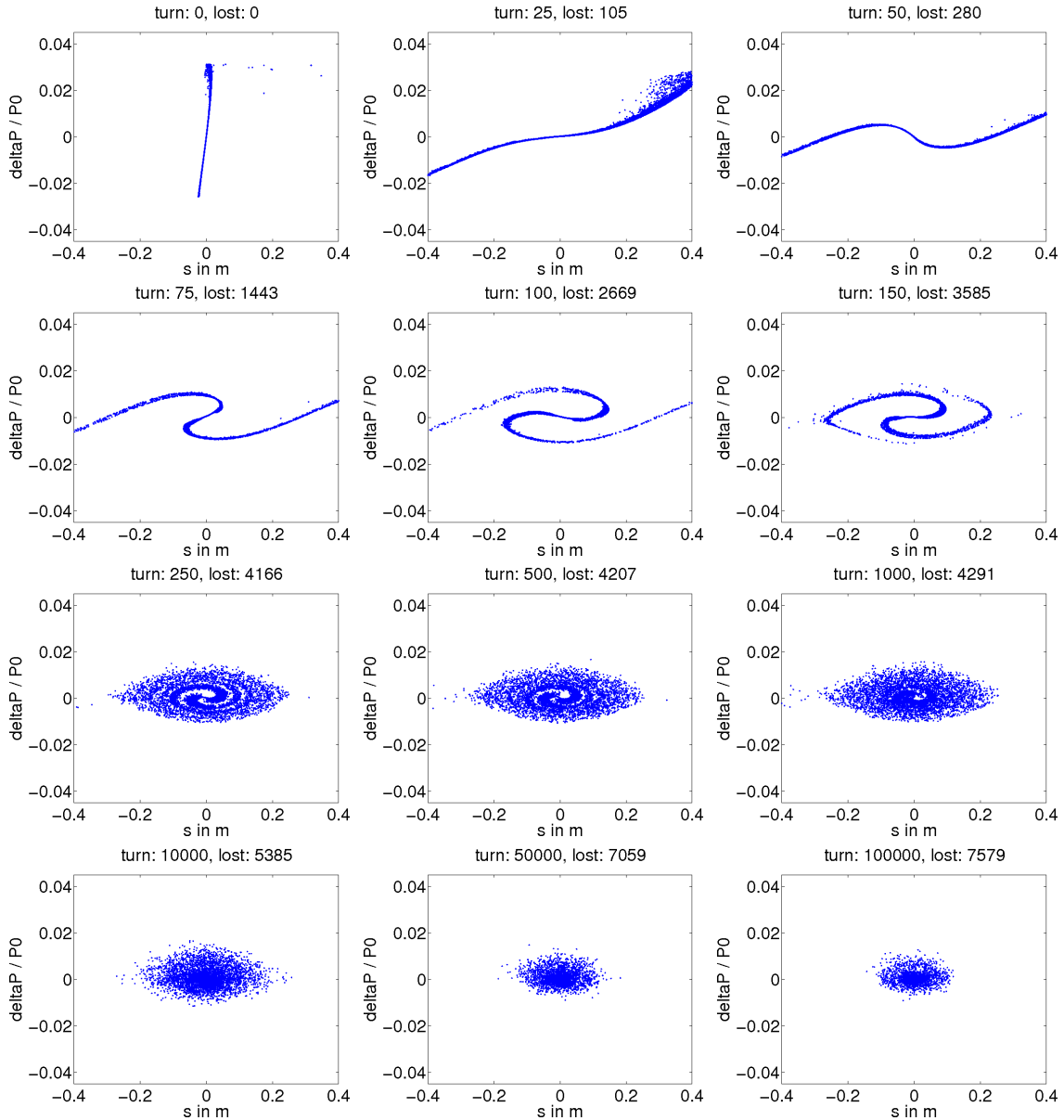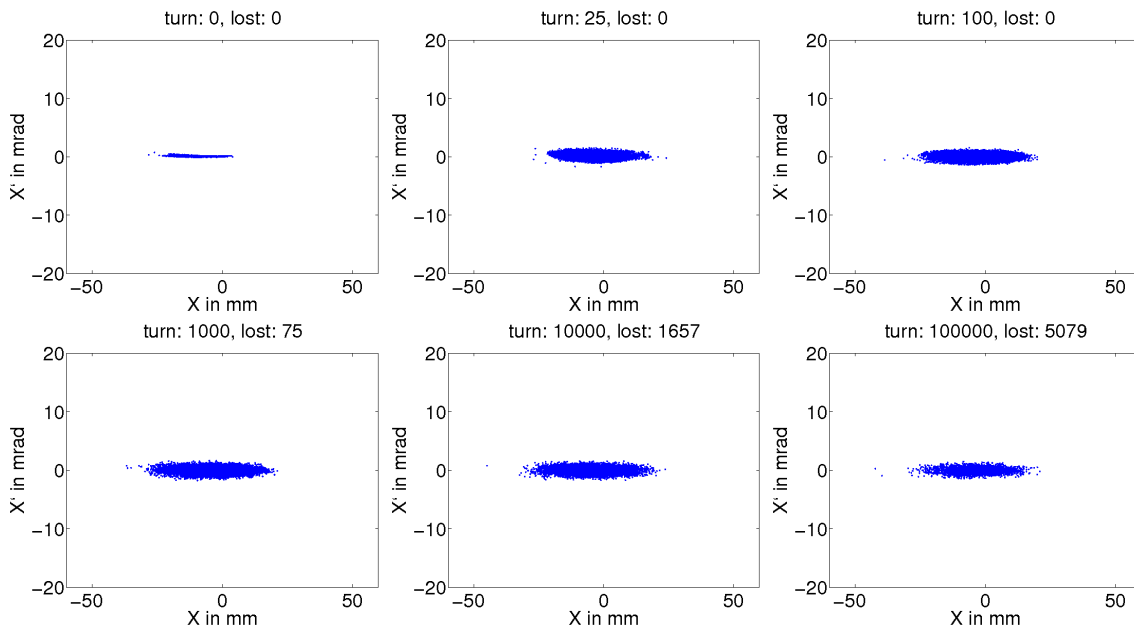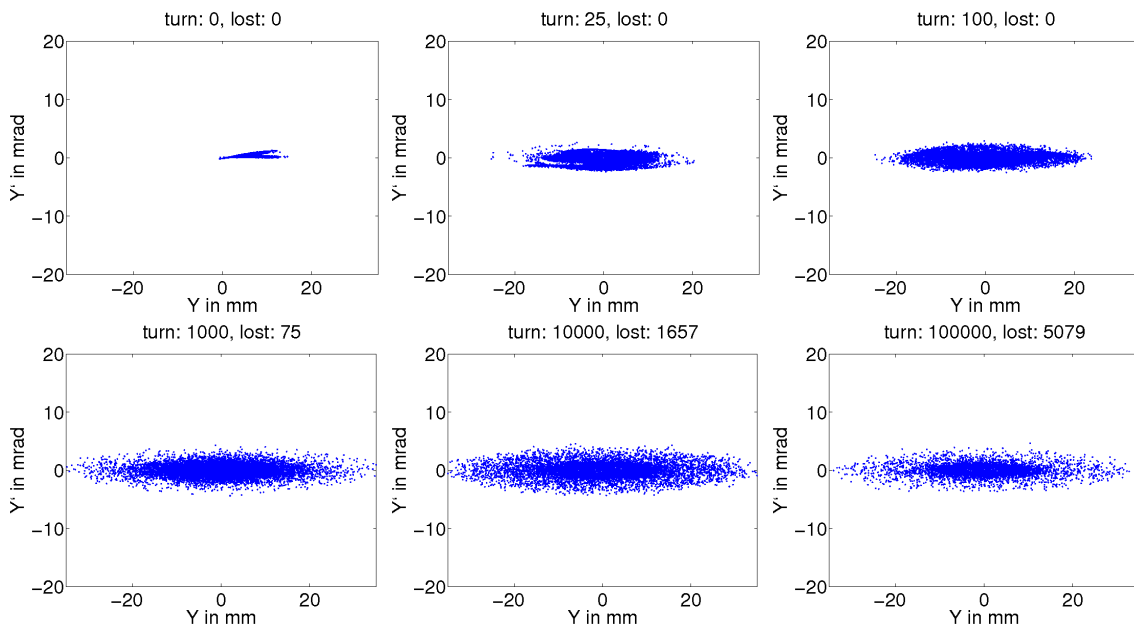
Figure 5.5: Top left to bottom right: Evolution of longitudinal phase space for a maximal initial energy deviation $\Delta p_{max}/p_0 = 0.03$, exceeding the energy acceptance of the ANKA lattice used. Note how the face space evolves much faster compared to Fig. 5.4. Also, note that significant fraction of the initial 10^4 simulated particles gets lost by moving out of the acceptance of the RF system. Transverse losses to the beam pipe have been neglected for this study. Also partially published in [194, 195].

Central energy p_0 in MeV	662
Cavity voltage in kV	200
Cavity frequency in MHz	499
Circumference in m	110.4
Revolution time in ns	368
Momentum compaction factor	0.008
Natural RMS energy spread	2.4×10^{-4}
Natural geometric emittance in m×rad	$6.8 \cdot 10^{-9}$
Radiation energy damping time in ms	79
Linear energy acceptance in %	1.1
Synchrotron tune in kHz	22.7
Synchrotron tune in turns	119.5
Bunch length in mm	4.0
Bunch length in ps	13.4

Table 5.9: ANKA Lattice Parameters at 662 MeV
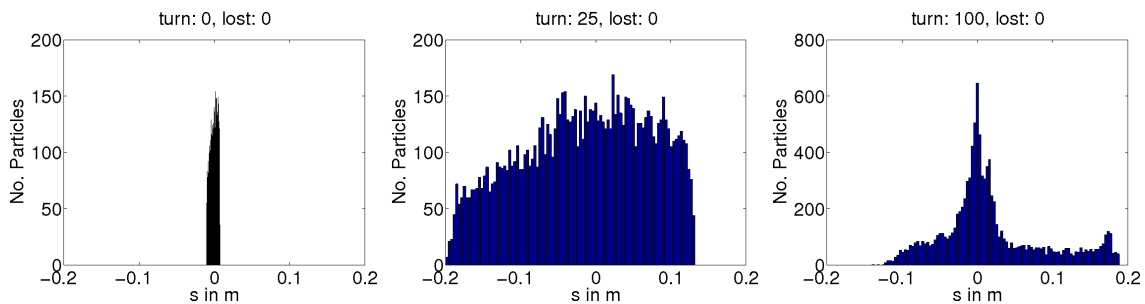
Figure 5.6: Left to right: Evolution of longitudinal charge density, for a maximal initial energy deviation $\Delta p_{max}/p_0 = 0.01$, cf. fig. 5.4. The narrow features could lead to increased CSR production. 10^4 particles were used for the simulation.

5.2.3 Behaviour in Synchrotron - Transversal

In the previous section, the focus was on the lengthening of LWFA bunches in a synchrotron. The transverse behaviour of the bunches has therefore been ignored. In practice, the transverse expansion of the beam would result in significant losses to the beam pipe, as illustrated in figures 5.7 and 5.8. In particular for the vertical plane, the bunch reaches the dimensions of the beam pipe after only a few turns (cf. second plot in fig. 5.8). It is also worth pointing out the before mentioned phase space plots always give the beam size at the injection point - the beam size can be much larger at other position along the ring.

Figure 5.7: Top left to bottom right: Evolution of horizontal phase space for a maximal initial energy deviation $\Delta p_{max}/p_0 = 0.01$. Losses to the beam pipe have not been considered. The ANKA beam pipe is $73\,\text{mm}$ wide.

Figure 5.8: Top left to bottom right: Evolution of vertical phase space for a maximal initial energy deviation $\Delta p_{max}/p_0 = 0.01$. Losses to the beam pipe have not been considered. The ANKA beam pipe is $32\,\text{mm}$ high.

5.2.4 Discussion

The work presented here investigated fundamental principles, it has not been optimized to the fullest extend possible. In particular:

i) LWFA simulations have been performed to the point of depletion of the driving laser pulse. Effects at the plasma exit have not been considered. The decrease of plasma density at the boundary should result in an increase of beam size and a decrease in beam divergence. This would mitigate the constraints on the transfer line.

ii) For our exemplary study, ANKA has not been optimized for maximal energy acceptance. It seems reasonable to increase the maximal energy acceptance to a few percent. In our case, this would allow to store about 50% more charge from the initial LWFA bunch.

In contrast, preserving the ultra-short bunch length seems challenging. With a dedicated low-α_c optic, the momentum compaction factor α_c can be reduced by two orders of magnitude compared to the one of the lattice used in our studies. Applying a stricter energy cut of e.g. $\Delta p_{max}/p_0 = 10^{-3}$ could reduce the path length difference per revolution by another order of magnitude (at the cost of a factor of $\sim$5 in charge). Neglecting all effects in the transfer line, a back of the envelope calculation using Eq. 5.2 yields that the bunch should lengthen to the ps bunch length, customary for state of the art light sources with dedicated low-α optic, within a few 100 turns.

For an operational facility, the transfer line would have to be studied in more detail, in particular the tolerance for fluctuations of energy and pointing. If ultra-short bunches were to be injected into the ANKA Synchrotron, the chromaticity of the transfer line would have to be corrected. Depending on the desired repetition rate, radiation protection might become a serious issue.

The evolution of the transverse phase space was not the main focus of this work, and losses to the beam pipe have therefore not yet been considered. In this regard, it is worth pointing out that:

a) This work is based upon LWFA simulations for the simplest possible setup: a laser pulse generating a plasma bubble in a uniform plasma, accelerating self injected electrons. Methods to control the injection process and to reduce the beam emittance are of great interest, and are very actively researched by many groups, cf. e.g. [94, 183–187].

b) If a synchrotron with the aim of producing CSR from ultra short LWFA bunches were to be build, the wavelength of the generated radiation might make the use of larger beam pipes necessary to avoid cut-offs. This in turn would again help to avoid transverse losses.

6. Studies for the AWAKE Experiment at CERN

This chapter describes my work performed for the AWAKE experiment at CERN, aiming to demonstrate proton-driven electron acceleration starting in 2015. As an early member of the collaboration, I have been involved in the experimental planing leading to the submission of the Letter of Intent (LoI) [18], in particular in the coordination between the different CERN groups and the choice of the experimental area.

Section 6.1 gives a short introduction to the CERN accelerator complex and the planning of the experiment in the initial stages until the submission of the LoI. In section 6.2, I evaluate the results of existing beam-plasma simulations with respect to accelerator physics requirements. My studies for a possible proton/electron energy spectrometer are described in section 6.3.

For the AWAKE Design Report [19], several aspects have changed in comparison to the initial planning. A short summary of these changes is given in section 6.5.

An introduction to the physics of plasma based acceleration is given in chapter 2. The peculiarities of long proton drive bunches are discussed in section 2.7.

Several collider proposals based on proton-driven acceleration found in the literature are discussed in chapter 4.4. My studies of a Higgs-facility based on proton-driven acceleration are described in chapter 4.7.2, page 62.

6.1 Experiment Description

6.1.1 CERN Accelerators, Choice of Experimental Area

Several proton accelerators are present at CERN. The accelerator chain is shown in figure 6.1. The acceleration starts at the LINear ACelerator LINAC2, increasing the beam energy through the PS-Booster (up to 1.4 GeV), the PS (Proton Synchrotron, up to 25 GeV) and the SPS (Super Proton Synchrotron, up to 450 GeV) before injecting into the LHC (Large Hadron Collider, up to 14 TeV nominal). At the start of the planning of the ex-
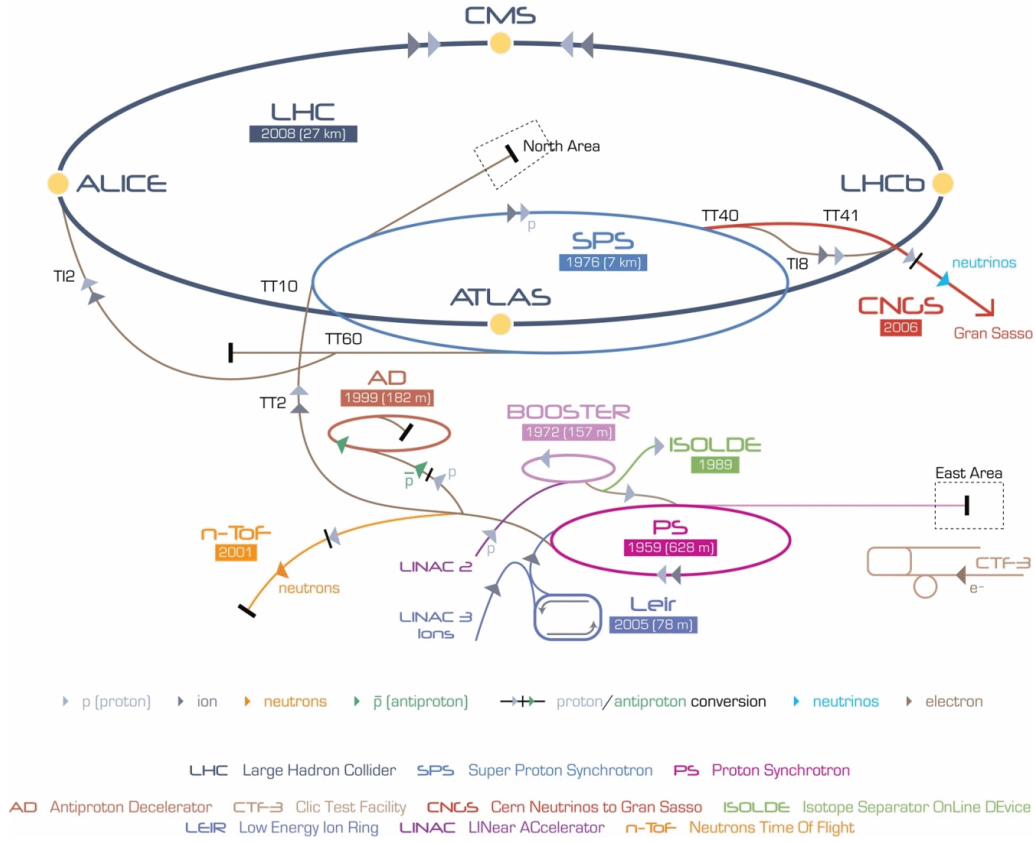
Figure 6.1: The CERN accelerator chain [201]. The AWAKE experiment will be situated either near the TT60 tunnel area south west of the SPS; or in the area currently used for CNGS (CERN Neutrinos to Gran Sasso). It will receive protons from the SPS.

periment, free experimental areas where available at both the PS and the SPS. The SPS beam was chosen for two reasons:

1. Due to the lower geometric emittance of the SPS beam, the transverse electric fields within the plasma are strong enough to focus the beam. This is not the case for the PS beam [70].

2. The larger experimental areas at the SPS are better suited to host all the equipment needed for the experiment.

Initially, it was planned to have the experiment in the TT61 tunnel (close to TT60, cf. figure 6.1). But due to the strong slope of about 7 % and the small width of only 4 m it was decided that the experiment had to move to one of the surface areas, which would also make access much easier. The schematic layout of the experimental planning at the time of the LoI is illustrated in figure 6.2. Due to radiation protection considerations and a possibly earlier availability, the CNGS area became the preferred option for the ADR. The integration of the technical components into the CNGS target area is illustrated in figure 6.3. The general layout and the following discussion are independent of the experimental area chosen.
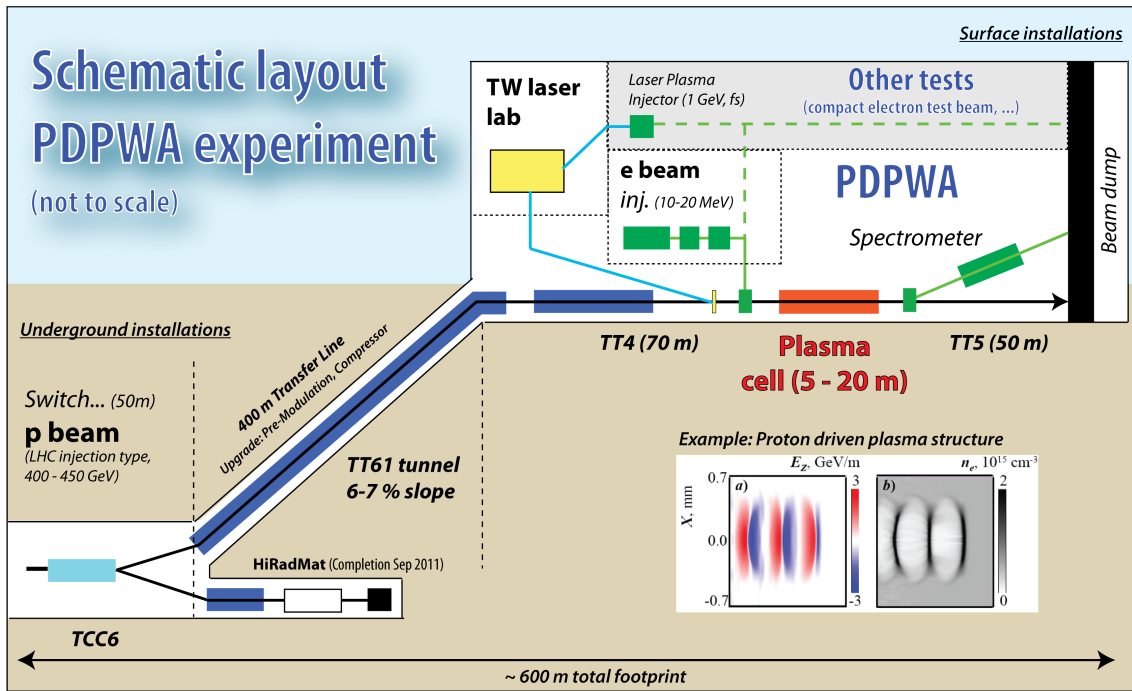
Figure 6.2: Schematic layout of the experimental areas, as conceived for the Letter of Intent [18].

6.1.2 Proton Beam Parameters

For the driving proton bunch, two parameter sets were used, cf. table 6.1. The parameter set labelled SPS-LHC describes the parameters of the SPS beam, as it was used for LHC injection at the time of the LoI. If not mentioned otherwise, this parameter set was used. The parameter set labelled SPS-Opt, short for SPS-Optimized, is a parameter set which would be beneficial for our experiment. At the time of the LoI, it was only used in single bunch operation for machine studies in the SPS. Due to improvements on the injector chain, it is now routinely used for LHC operation and will be standard by the starting time of the AWAKE experiment. The two parameter sets only differ in the bunch charge and the bunch length. (The longer bunch length in the SPS-Opt case is only due to a safety margin, as the required new SPS optics were not thoroughly tested at the time of the simulations.)

For our experiment, a small beam size at the plasma entrance (small β^*) is beneficial, since the strength of the generated wakefield depends linearly on the drive beam density, which increases quadratically when reducing the beam radius (cf. eq. 2.41, page 20). We have therefore assumed a round beam size at focus of $\sigma_x = \sigma_y = 200 \, \mu$m, as achieved at HiRadMat, the High Radiation on Materials test facility recently completed [202].

As explained in chapter 2.7.2, a long, self-modulated proton bunch will be used to drive the wake fields for our experiment. For this self modulation to occur in a stable and reproducible manner, it is necessary to seed the self-modulation instability. For the beam-plasma simulations, this is achieved by using a so-called hard cut beam. This means that the first half of the beam is supposed to be cut off, resulting in a steep increase in charge density, cf. figure 6.5, page 96. In the experiment, this could be realized e.g. via an alkali metal vapour cell and a co-propagating laser. The laser pulse would ionize the metal vapour of the plasma cell in the middle of the proton bunch. Thus, the plasma would see
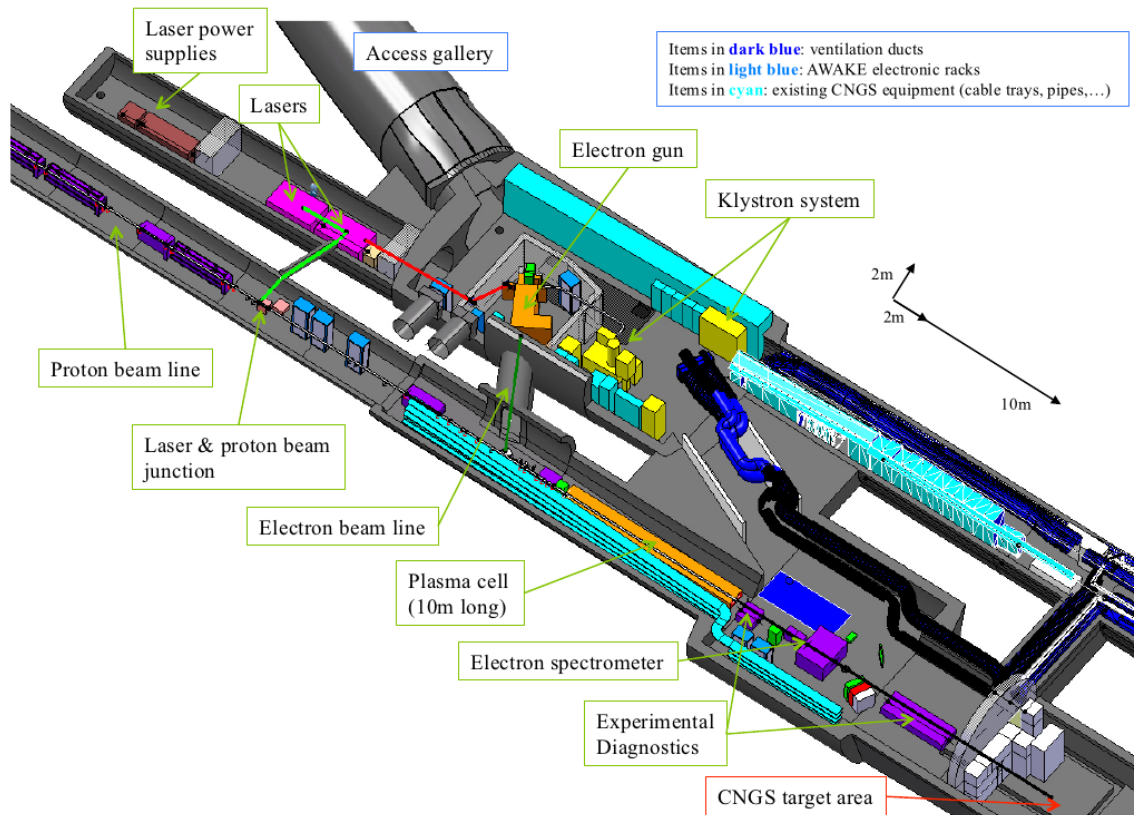
Figure 6.3: Integration of the AWAKE experiment into the CNGS tunnel [19].

the only the second half of the bunch, starting with maximum charge density. The space charge force of the proton beam is not high enough to field ionize the metal vapour itself.

Proton Beam Delivery

For the beam delivery system a final focus similar to the one used at the HiRadMat facility is planned. Figure 6.4 shows the beamline design used there.

6.1.3 Electron Beam Parameters

For the witness electron bunch, a short and a long test case have been defined, cf. table 6.2. The parameters of the short bunch are parameters for the former LEP electron gun. It has been argued that with a very diluted bunch, a much smaller beam size should be reachable. Therefore, the long bunch case has been defined.

6.1.4 The Plasma Cell

Many current day LWFA experiments use gas jets as plasma source, the gas being ionized by the driving laser. For the PWFA experiments carried out at SLAC, a metal vapour source was used. For these experiments, the electron bunch served both to ionize the vapour via its Coulomb field and to drive the plasma wake. Neither is possible for the AWAKE experiment, as the Coulomb field of the SPS proton bunch is not strong enough for ionization.

For our experiment, three conceptually different cell types are being investigated in parallel by different groups. The baseline cell is a laser-ionized Rubidium heat-pipe oven, as seeding

Parameter	SPS-LHC	SPS-Opt
Reference energy E_P in GeV	450	450
Number of protons N_P (10^{10})	11.5	30.0
RMS energy spread σ_P in MeV	135	135
RMS bunch length σ_z in cm	12.0	12.4
RMS beam radius σ_r in μm	200	200
Corresponding β^* in m	5	5
RMS divergence θ in mrad	0.04	0.04
Geometric emittance in nm $\cdot$ rad	7.3	7.3
Normalized emittance in μm $\cdot$ rad	3.5	3.5

Table 6.1: Proton beam parameter sets used for simulations. The beam energy used for the experiment will be 400 GeV. This will allow to re-use the existing CNGS beamlines [19].

Parameter	short	long
Reference Energy E_P in MeV	10	10
Number of Electrons $N_e/10^6$	1000	1
RMS bunch length σ_z in mm	5	100
RMS beam radius σ_r in mm	2	0.2
RMS divergence θ in mrad	1.7	0.1
Normalized emittance in μm $\cdot$ rad	70	not defined
Geometric emittance in μm $\cdot$ rad	3.4	not defined

Table 6.2: Electron beam parameters used for plasma wakefield simulations. For the ADR [19], they have changed slightly.

is easiest with this option. However, as it requires an ionizing laser, its maximal length is limited. In contrast, seeding is more difficult for the other cell types studied, but they allow for easier scaling to arbitrary lengths. The different plasma cell technologies are discussed in more detail in [18, 19].

Plasma Parameters

For the baseline plan of the experiment, the plasma cell properties given in table 6.3 have been assumed. For the plasma density, one would like to maximize $k_p\sigma_z$, so that the plasma wave length is much shorter than the bunch length. That way, the modulation would develop close to the centre of the bunch, where most of the protons reside. However, we need the plasma skin depth to be at minimum the transverse size of the bunch for the modulation to be effectively produced, i.e. $k_p\sigma_r \leq 1$ [203]. This limits the maximum plasma density n_0, as $k_p = \frac{\omega_p}{c} = \frac{1}{c}\sqrt{\frac{n_0 e^2}{\epsilon_0 m_e}}$. Furthermore, we want the proton beam to be about 100 plasma wavelengths long, $\lambda_p/\sigma_z \approx 100$. The inverse of this number gives an estimate of the acceptable level of plasma density fluctuations, about 1 % [70].
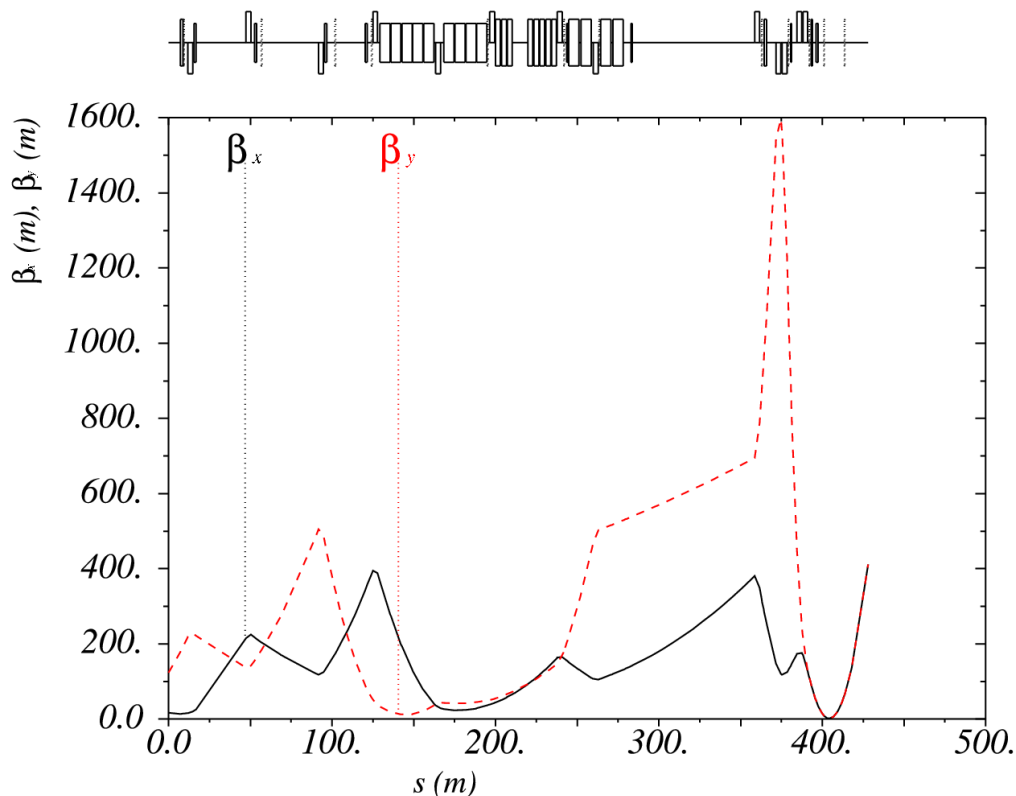
Figure 6.4: Beamline optics of the HiRadMat test facility with β functions calculated for a spot
size at the focus of $0.1\,\text{mm}\times0.1\,\text{mm}$, reproduced from [202]. On the x-axis is the
distance along the line in m, on the y-axis the horizontal and vertical β functions.
Above is a schematic view of the beam line, including the β-matching section. The
rectangles above (below) the solid line represent horizontally (vertically) focusing
quadrupoles, the rectangles centered around the solid line represent dipole magnets.

6.2 Interface from Plasma to Beam Simulations

Several beam-plasma simulations have been carried out for the AWAKE experiment, and
are still going on [18, 19]. Within this section, I have evaluated these existing simula-
tions with respect to accelerator physics requirements and measurable signals. Particular
emphasis is put on the consequences for the initially planed proton energy spectrometer
which will be discussed in section 6.3.

6.2.1 Proton Bunch Simulations, 10 m Plasma Cell

Default Bunch Charge - SPS-LHC Parameter Set

This section presents the results of beam-plasma simulations by K. Lotov, for the SPS-
LHC parameter set (cf. table 6.1) and the consequences thereof. LCODE was used for
these simulations, see [204, 205] and appendix C.1 for more information.

For the beam-plasma simulations a so called hard cut beam is used. This means that
the first half of the beam is supposed to be cut off, resulting in a steep increase in charge
density. (For more information, see chapters 2.7.2 and 6.1.2.) Figure 6.5 shows the current
distribution along the bunch, as well as the resulting energy modulation after a 10 m plasma
cell. Several results can be drawn from this figure:

1. The longitudinal charge distribution does not change noticeably due to the interaction with the plasma.

2. The energy modulation is strongest at the tail of the bunch, where the current is relatively low.

3. The period of the energy modulation is given by the plasma wavelength.

4. The energy modulation is very small compared to the initial energy of approximately 450 GeV.

Figure 6.6 shows a histogram of the longitudinal momentum before and after the 10 m plasma cell. The RMS energy spread increases from 135 MeV to 149 MeV, at an average energy of 450 GeV. To have a good signal to noise ratio, one would like the number of particles above/below a certain cut-off energy to triple. If one looks at the particles gaining energy, this results in a cut-off energy of 450.15 GeV and the number of particles above this energy changing from $2.9 \cdot 10^7$ to $8.8 \cdot 10^7$ protons, once the plasma is turned on. For the particles loosing energy the cutoff energy is 449.35 GeV, and the number of particles below this energy changes from $8.6 \cdot 10^8$ to $27.3 \cdot 10^8$ protons, once the plasma is turned on. The total number of protons is $1.15 \cdot 10^{11}/2$ protons in the hard cut beam. This means that: i) it is easier to measure the energy loss, rather than the energy gain, ii) one has to measure a relatively low percentage of particles.

In addition to the longitudinal momentum, the plasma also influences the transverse properties of the beam. Figure 6.7 shows the change of the transverse beam size and the transverse momentum distribution before and after a 10 m plasma cell. They are also modulated with the plasma wave length and increase dramatically. This can not be suppressed, since it is exactly this modulation of the transverse charge density that creates the electric fields which cause the longitudinal energy modulation. Figure 6.8 shows histograms of the transverse beam size and the transverse momentum distribution before and after a 10 m plasma cell. As a result of the transverse modulation, the geometric (normalized) transverse emittance increases from $\epsilon_x = 8.0$ nm ($\epsilon_{N,x} = 3.8$ μm) to $\epsilon_x = 41.0$ nm ($\epsilon_{N,x} = 19.7$ μm). This is problematic, as the emittance is a conserved quantity in accelerator physics (assuming there are only conservative forces acting on the beam).

Type of cell	Heat-pipe oven,
	laser-ionized
Type of plasma	Lithium vapour
Plasma Electron density n_e	$7 \cdot 10^{14}$ cm^{-3}
Plasma density fluctuations	$\leq 1\%$
laser beam power	$2.2 \cdot 10^{10}$ Wcm^{-2}s^{-1}
laser beam energy	3.4 J in 5 ns
Plasma length	5-10 m

Table 6.3: Plasma cell parameters assumed for the simulations this work is based upon. For the ADR, values have changed slightly. In particular, Rubidium has been chosen over Lithium [19].
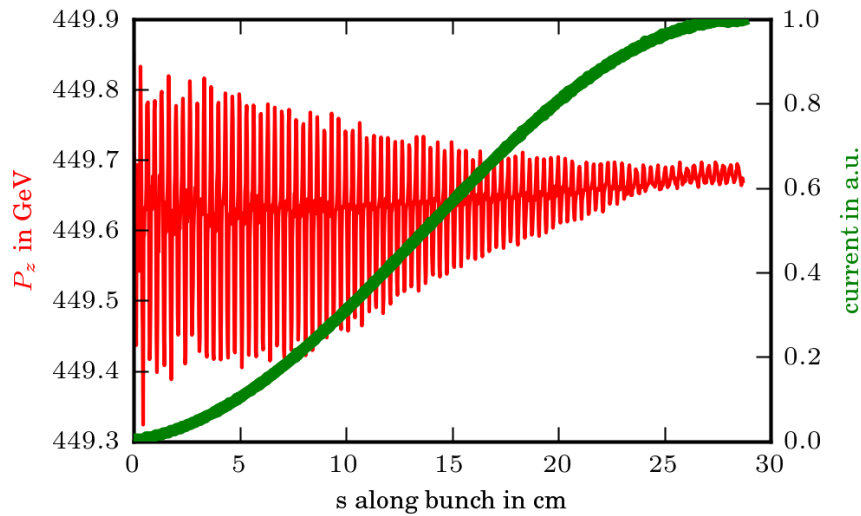
Figure 6.5: Current and energy distribution along a proton bunch after 10 m of propagation in a plasma cell. The x-axis gives the position along the bunch, with propagation direction towards higher s values. The red curve shows the average energy per bin in GeV, the green curve the hard cut current distribution along the bunch. The longitudinal current distribution does not change due to the interaction with the plasma. The energy modulation is strongest at the very tail of the bunch. Published in [206].
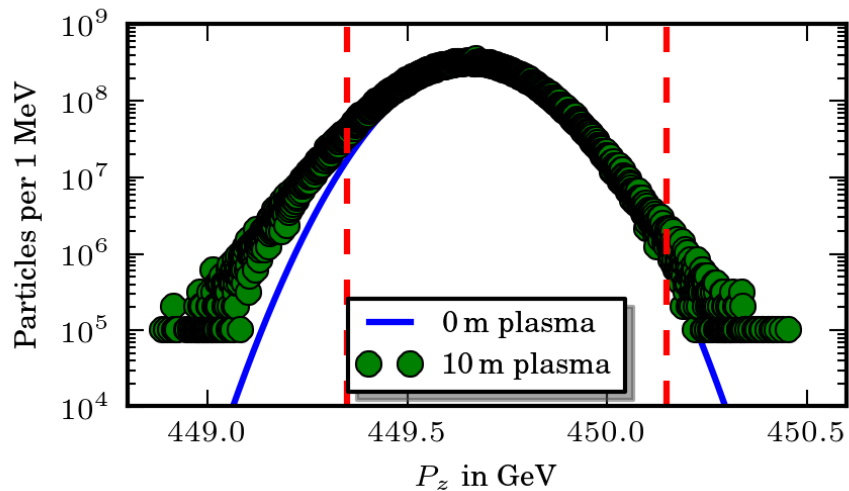
Figure 6.6: Histogram of the longitudinal momentum before and after a 10 m plasma cell. The blue solid line shows the initial energy distribution, the green dots show the energy distribution after the plasma. One macro particle corresponds to roughly 10^5 protons, therefore there are no entries below that value. The dashed red lines indicate the cut-off energy below/over which the number of particles triples once the plasma is turned on. The total number of protons is $1.15 \cdot 10^{11}/2$ protons in the hard cut beam (SPS-LHC parameter set, see table 6.1).
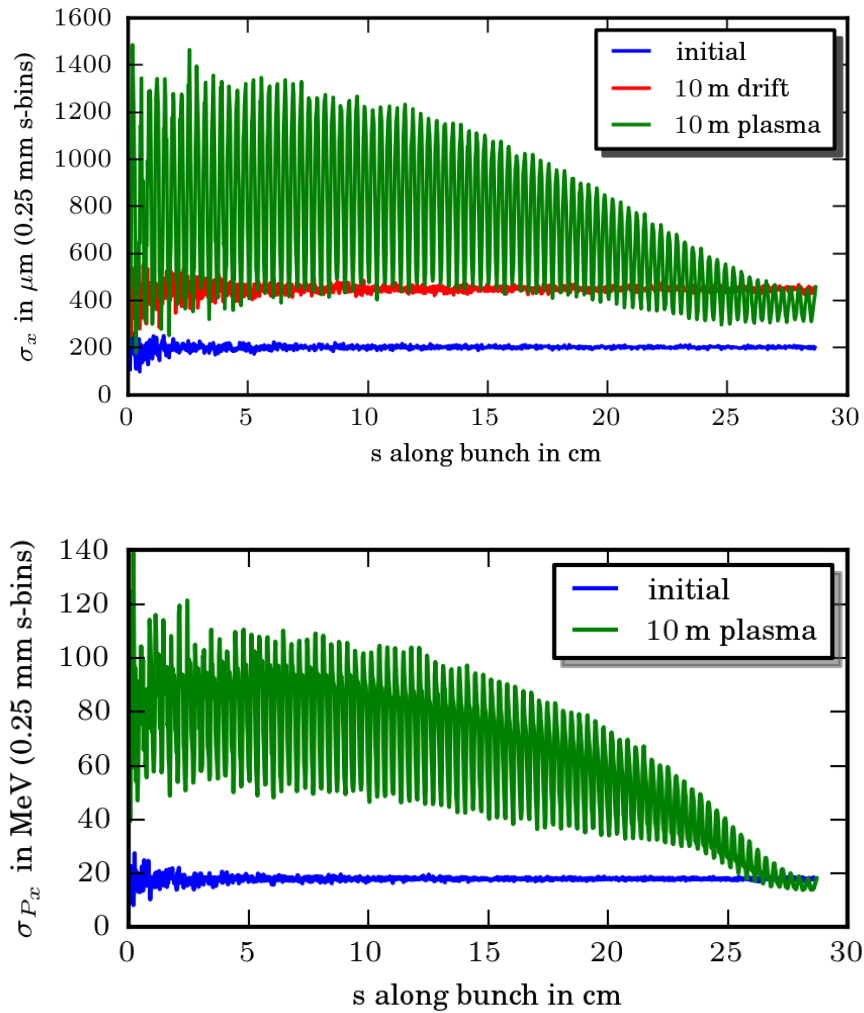
Figure 6.7: RMS beam size (top) and RMS transverse momentum (bottom) along the beam. For both beam radius and momentum, the modulation length is given by the plasma wavelength. The 10 m drift case is generated by propagating the initial particle distribution ballistically. The momentum distribution remains constant in a drift and is therefore only compared to the initial case. Partly published in [206].
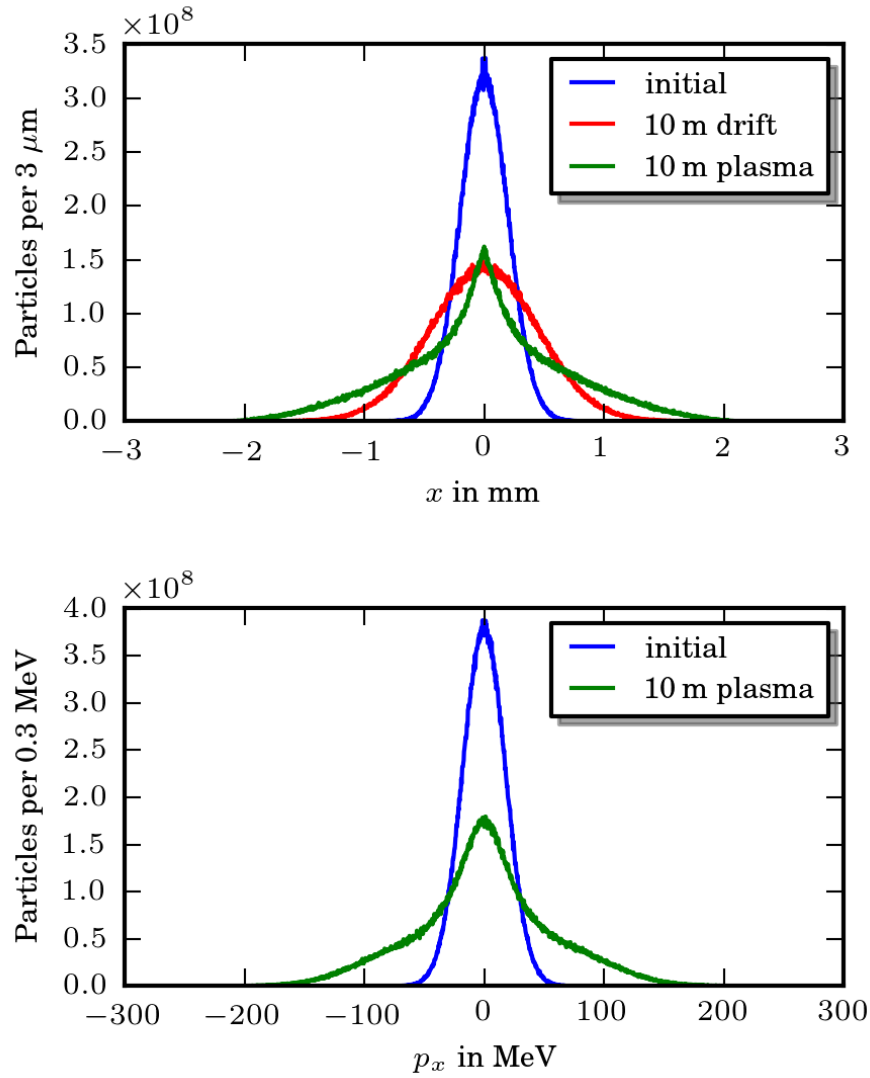
Figure 6.8: Transverse particle density distribution and the transverse momentum distribution before and after the plasma cell. They both increase significantly due to the plasma. The momentum distribution remains constant in a drift and is therefore only compared to the initial case. The change in shape of the histogram can be understood, as half of the beam gets focused by plasma wakefield whereas the other half sits in the defocusing phase. One simulation particle corresponds to roughly 10^5 protons, therefore there are no entries below that value.

As a consequence, the beam has to be focussed stronger to keep the initial beam size, or the aperture after the plasma cell has to be increased to transport the blown up beam. With respect to the planed experiment this is even more problematic, as the effect of the increased emittance has to be distinguished from the energy dependent dispersive effect one would like to see in a spectrometer.

From this result, one can already see the necessity of a focusing system, if a proton energy spectrometer were to be build. For a proton with a relativistic factor γ_0, the radius of curvature in a magnetic field B is $\rho = \frac{\gamma_0 m_p \beta c}{Bq}$. Along a dipole magnet of length l with a uniform magnetic field, the deflection angle is $\theta \simeq \sin(\theta) = \frac{l}{\rho} = \frac{lBq}{\gamma_0 m_p \beta c}$. For a bunch with a spread in energy, there is a difference in deflection angle between protons with energies γ_0 and $\gamma_0 + \delta\gamma$ of $\delta\theta \cong \theta \frac{\delta\gamma}{\gamma_0}$. For protons with an energy of $450\,\text{GeV}$ ($\gamma_0 \approx 480$, $\beta \cong 1$), a magnet of length $l = 10\,\text{m}$ and uniform field of $1.5\,\text{T}$, this results in $\rho \approx 1002\,\text{m}$ and $\theta \approx 0.010\,\text{rad}$. Assuming an energy change of $1\,\text{GeV}$ ($\approx \pm 0.22\,\%$), the opening angle of the beam exiting the magnet is $\delta\theta \cong \pm 2.2 \times 10^{-5}\,\text{rad}$. We assume that the beam exiting the plasma has the same transverse size as at the plasma entrance, i.e. $\sigma_r = 200\,\mu\text{m}$. Then the beam has to have a divergence angle much smaller than the one given by the magnet energy dependent bending, i.e. have a geometric emittance smaller than $\epsilon = \sigma_r \delta\theta \cong 4.4 \times 10^{-9}\text{m} \times \text{rad}$. The corresponding condition for the normalized emittance is $\epsilon_N = \gamma\epsilon \ll 2.1 \times 10^{-6}\text{m} \times \text{rad}$ [207]. This is after the plasma has focused and defocused the protons. This means that even for an assumed energy gain much higher than the one observed for $10\,\text{m}$ of plasma, one would need an emittance much lower than the one observed.

Alternatively, one can also get this result via the transverse momentum. For $10\,\text{m}$ of plasma, the maximum transverse momentum observed in the simulations is approximately $230\,\text{MeV}$, corresponding to an angle $x' = p_x/p_z$ of about $500\,\mu\text{rad}$. The highest energy gain in the simulations was about $160\,\text{MeV}$, corresponding to a change in γ of about 0.17. If one requires that the angle between particles with average and particles with maximal momentum is greater than the maximal angle due to transverse momentum (i.e. $\delta\theta \gg x'$), this leads to $Bl \gg \frac{x' m_p c}{(1/\gamma_{max} - 1/\gamma_{avg}) \cdot q} \approx 2100\,\text{Tm}$. Given a maximal field strength of normal conducting magnets $B \lesssim 2\,\text{T}$, this is completely unrealistic for a demonstration experiment.

It is nonetheless worth noting that the particles that gain most energy are in the centre of the bunch, while the defocused particles at high radii do not gain/loose much energy. This can be seen from figure 6.9, which shows the longitudinal energy plotted over the longitudinal and transverse position.

High Bunch Charge - SPS-Opt Parameter Set

For the SPS-Opt parameter set (cf. table 6.1), beam-plasma simulations have been performed by Alexander Pukhov using VLPL, cf. [192] and appendix C.2 for more information. The longitudinal energy modulation is larger than for the SPS-LHC parameter set, as illustrated in figure 6.10. However, it was decided that the energy modulation is still not strong enough to make for a convincing experiment by itself. It has therefore been decided to aim for electron acceleration already in the early phases of the experiment. Simulation results regarding electrons will be discussed in section 6.2.3.
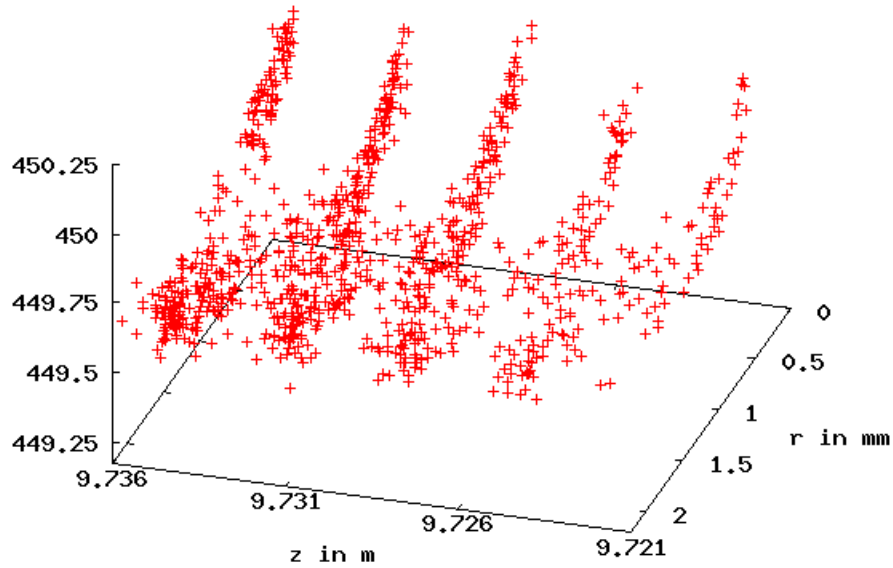
Figure 6.9: Longitudinal momentum in GeV over radius and position along bunch. Zoom on the
tail of bunch after about 9.7 m of propagation in plasma. One can clearly see the
longitudinal modulation along z with the plasma period. One can also see that the
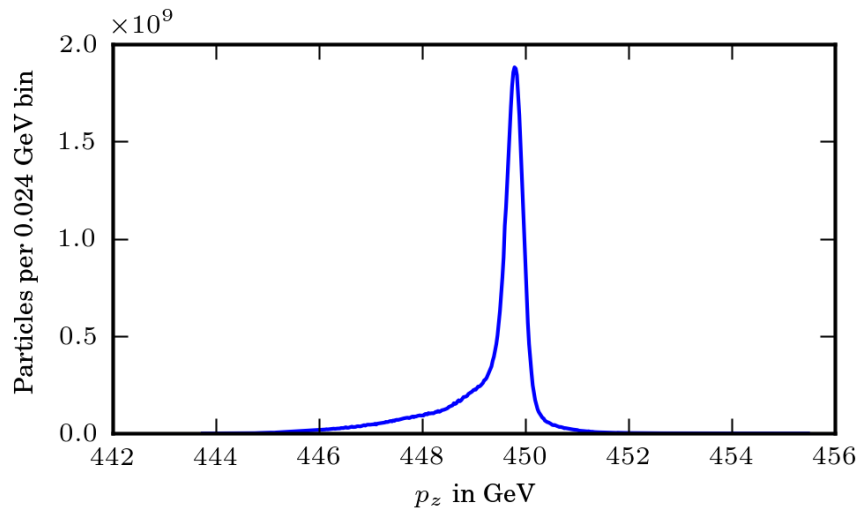particles with the highest energy are in the centre of the bunch ($r \simeq 0$).

Figure 6.10: Histogram of the longitudinal momentum after a 10 m plasma cell for the SPS-
Opt parameter set, cf. table 6.1. The energy modulation is stronger than for the
SPS-LHC case, cf. figure 6.6.

6.2.2   Proton Bunch Simulations, Different Cell Lengths

Several lengths for the plasma cell have been studied. Figure 6.11 compares the longitudinal momentum distribution after 10 m and 30 m of plasma. Whilst an increase in maximum energy is apparent, the emittance increases as well, which in the end does not make it easier to observe an energy gain. Also, with today's technology, it is not clear how to generate a 30 m long cell with the required plasma homogeneity. Therefore, it has been agreed to not consider plasmas of more then 10 m length for the first phases of the experiment [19].

On the other hand, as explained in chapter 2.7.3, the self-modulation instability needs about 5 m to develop (for the parameters chosen for the experiment). Due to the reduced phase velocity of the wake during the self-modulation process, injecting electrons from the beginning would result in rapid dephasing and a loss of said electrons. In the current planning of the experiment, it is foreseen to inject electrons after the proton beam has already travelled approximately 5 m in plasma [19]. Plasma cells significantly shorter than 10 m have therefore not been considered.
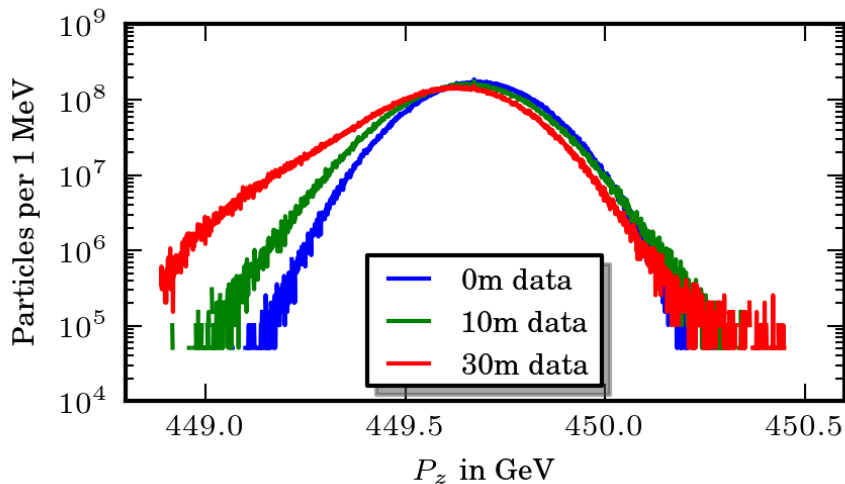
Figure 6.11: Shown are the simulated longitudinal momentum distributions before the plasma cell as well as after 10 m and 30 m of plasma. The x-axis gives the momentum p_z in GeV, the y-axis the number of particles per energy bin. The energy spread increased from 135 MeV at the plasma entrance to 149 MeV after 10 m and 175 MeV after 30 m of plasma.

6.2.3   Electron Bunch Simulations

Beam-plasma simulations including injected electrons have been performed by Alexander Pukhov using VLPL (cf. [192] and appendix C.2 for more information).

Figure 6.12 shows the resulting energy distribution of an 10 MeV electron beam which has been injected along with the driving proton bunch into a 7 m plasma cell. Electron energies of over 100 MeV are reached, but the energy spectrum is very broad. This is due to the fact that for this simulation, the injected electron bunch was much longer than one plasma wavelength. As a result, the bunch sampled all phases of the field distribution generated

by the proton bunch. Furthermore, for a low energy electron bunch the changes in energy are strong enough to lead to velocity differences and therefore a phase slippage along the propagation distance. As for the protons, the transverse momentum and size increase as well (the electrons do not only sample the accelerating and decelerating longitudinal fields but also the focusing ans defocusing transverse fields). For the later phases of the project, a laser-plasma based electron source could provide ultra-short pulses, leading to quasi mono-energetic bunches.

As explained in chapter 2.7.3 (page 22), the self-modulation of the proton bunch takes a few meters to develop. During this modulation process, the phase velocity of the plasma wake is significantly reduced. For a highly relativistic electron witness bunch, this can lead to rapid dephasing. Therefore, injecting the electron bunch in parallel with the proton bunch is not optimal. This problem can be solved by injecting electrons under a small angle, a few meters upstream of the beginning of the plasma cell.

The exact angle and position for the injection are still subject to optimization [19, 72]. The expected electron spectra are therefore still bound to change, depending on the final findings. Depending on the proton bunch density and the acceleration length, an energy gain between a few hundred MeV and a few GeV is expected for the experiment [19]. Detection of high energy electrons will be a clear experimental signal.
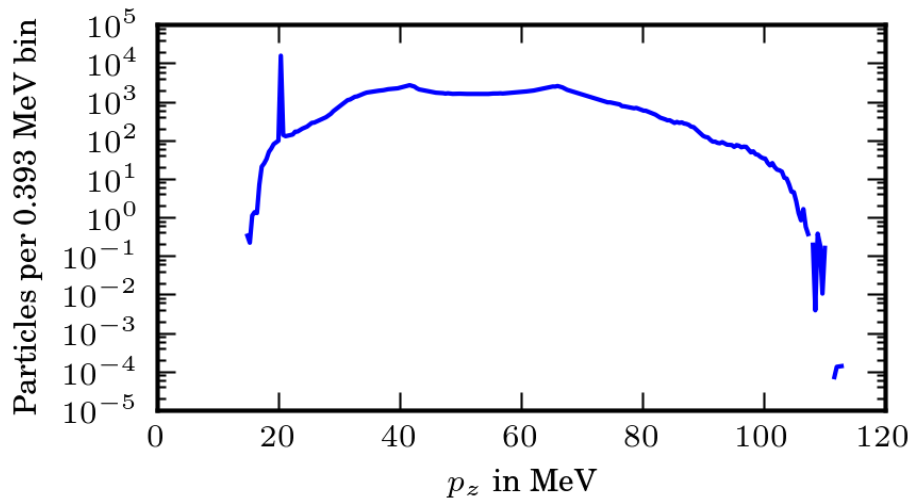

Figure 6.12: Energy spectrum of an electron bunch (particles per energy interval over particle energy) which copropagated with the driving proton bunch for $7\,\mathrm{m}$, $N_P = 1.15 \cdot 10^{11}$, $n_0 = 1 \cdot 10^{14}\,\mathrm{cm}^{-3}$. The initial electron energy was $10\,\mathrm{MeV}$. ($5.6 \cdot 10^6$ particles were used in the simulation, corresponding to $2.5 \cdot 10^5$ electrons. The non-integer numerical weights result in bins with only a fraction of a particle.) Published in [206].

6.3 Detection of Energy Gain

This section deals with the general workings of an energy spectrometer, its implementation in the code and the results thereof.

6.3.1 General Principle

Charged particles are bend in a magnetic or electric field due to the Lorentz force F_L [27],

$$\vec{F}_L = q[\vec{E} + (\vec{v} \times \vec{B})] = q[\vec{E} + (\vec{\beta}c_0 \times \vec{B})], \tag{6.1}$$

where $\vec{E}$ and $\vec{B}$ are the electric and magnetic fields, q is the charge of the particle and $\vec{v} = \vec{\beta}c_0$ it's velocity. The general idea of an energy spectrometer is to use the energy (velocity) dependence of this force in a magnetic field to sort particles by their energy. Combining with the centripetal force F_c [27]

$$F_c = \frac{mv^2}{\rho}, \tag{6.2}$$

one gets an energy dependent bending radius ρ:

$$\rho = \frac{\gamma m_0 \beta c}{Bq}. \tag{6.3}$$

For a dipole magnet of length l this gives an bending angle of

$$\sin(\theta) = \frac{l}{\rho}. \tag{6.4}$$

Due to this energy dependent deflection angle particles with different energies end up at different positions on a screen downstream of the bending magnet. The working principle is illustrated in figure 6.13.
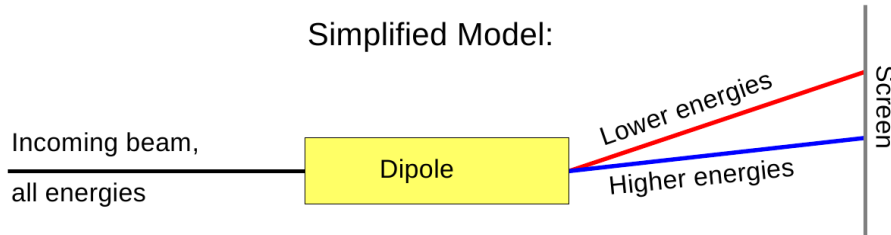

Figure 6.13: General principle of an energy spectrometer. Particles with lower energies get deflected stronger in the dipole magnet. This way, their position on a screen gives information about their energy.

6.3.2 Implementation

To simulate possible spectrometer images, the dipole magnet was treated as a so-called point-kick. This means letting its length go to zero while keeping the product $B \cdot l$ constant. For each particle the position x_{fin} on a spectrometer screen is then given by

$$x_{fin,i} = \left(\frac{p_{x,i}}{p_{z,i}} + \theta_i \right) \cdot s + x_{in,i}, \quad \theta_i \approx \frac{lBe}{\gamma_i mc}. \tag{6.5}$$

Here, p_x/p_z is the angle the particles have with the initial reference trajectory due to their transverse momentum, θ is the energy dependent kick of the magnet, s is the length of the drift space between the magnet and the spectrometer screen and x_{in} is the initial transverse position. The approximation $\beta = 1$ is made in the calculation of the angle. (Note that for $B = 0$, equation 6.5 simplifies to the formula for ballistic propagation.) In this treatment, $x = 0$ is the initial reference trajectory. The spectrometer screen is assumed to be orthogonal to the initial beam trajectory. The spectrometer images created this way were compared to the ideal case were $x_i = 0$ and $p_x = 0$, i.e.

$$x_{fin} = \theta \cdot s. \tag{6.6}$$

They were also compared to the case achievable with a focusing system, which eliminates the dependence on the transverse momentum p_x, i.e.

$$x_{fin} = \theta \cdot s + x_{in}. \tag{6.7}$$

The angle θ is again calculated as in equation 6.5.

In principle, a telescopic system could be used to reduce the dependence on the initial beam size by a demagnification factor m to $x_{fin} = \theta \cdot s + x_{in}/m$ [29]. However, as the initial beam size is already very small and the SPS proton beam has a very high energy, this option was discarded.

6.3.3   Proton Spectrometer without Focussing

The spectrometer images calculated in this section are based on beam-plasma simulations by Konstantin Lotov, cf. section 6.2.1.

For the simulations shown an integrated field strength $\int B dl = 22.5\,\mathrm{Tm}$ has been assumed, as well as a drift between the dipole and the screen of $100\,\mathrm{m}$. (To achieve an integrated field of $22.5\,\mathrm{Tm}$ one would need two dipoles of $7.5\,\mathrm{m}$ length and $1.5\,\mathrm{T}$ field strength, or three of the $6.6\,\mathrm{m}$ dipoles currently used in the SPS. Going to a higher integrated field strength did not seam reasonable.) Figure 6.14 shows the comparison of an ideal spectrometer image as calculated via equation 6.6 and a more realistic image as calculated via equation 6.5. Both times the particle distribution after $10\,\mathrm{m}$ of plasma is compared to a particle distribution which has been obtained from the initial beam data (at the entrance of the plasma) by propagating the particles ballistically for the length off the plasma cell.

Note that for the ideal case the centre of the distribution shifts to the right, i.e. towards lower energies. This is due to the fact that the average energy of the proton beam decreases by approximately $27\,\mathrm{MeV}$ during the interaction with the $10\,\mathrm{m}$ of plasma.

6.3.4   Proton Spectrometer with Focusing

As shown in sections 6.2.1 and 6.3.3, the energy modulation of the proton beam can not be measured without a focusing system. Figure 6.15 shows how a spectrometer image could look like if focusing was used.

To image the change in the particle distribution to the screen, the beam transport system has to fulfil certain requirements:
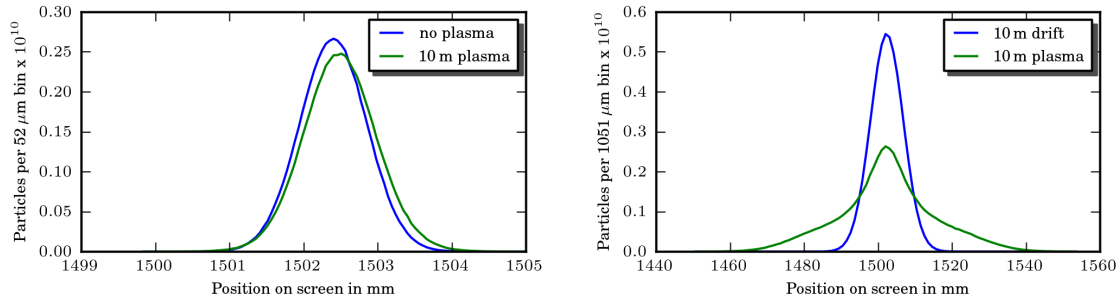
Figure 6.14: Both: The x-axis is the position on a screen in the beam path, x=0 is the initial beam trajectory before the spectrometer dipole. The y-axis gives the number of particles at this position. The number of bins is identical in both plots, which results in different bin widths.
Left: Ideal case, for which the position on the screen depends *only* on the longitudinal momentum.
Right: Spectrometer image as it would result from a spectrometer without focusing, as calculated via equation 6.5.
The effect of the longitudinal momentum modulation is completely overshadowed by the increase of transverse momentum and position.

1. The phase advance μ between the entrance of the plasma cell and the screen must be an integer multiple of π in both planes. Otherwise the focusing system changes the properties of the beam with respect to the initial distribution. As a result, the β-functions at the plasma entrance and at the spectrometer screen have to be identical [29].

2. The dispersion D in the spectrometer plane should be as big as possible to see a strong effect of the energy dependence.

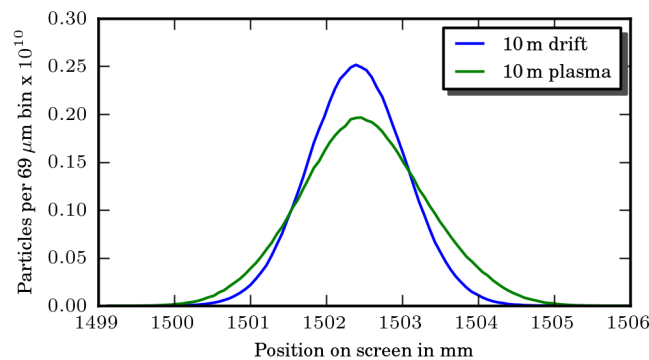3. The dispersion in the other plane should be as small as possible, preferably zero.

Figure 6.15: A spectrometer image as it could be obtained with focusing. It is still difficult to distinguish the effect of the energy modulation from the influence of the transverse particle position, cf. figure 6.14.

Furthermore,

4. the distance from the first image point to the beginning of the first quadrupole must be at least 15 m to offer enough space for the plasma cell, vacuum equipment and diagnostics.

5. the system should be short and simple to save costs.

To fulfil these requirements, a focusing system of two quadrupole triplets with dipoles in between has been chosen. This layout is symmetric around it's centre and reaches the same minimum β values in x and y, given symmetric input values. Among the simple schemes it is the one that achieves the smallest maximal beam size [29, 208, 209]. For the design of the conceptual layout the program MAD-X [196] has been used. The result is shown in figure 6.16. The focusing system has a length of 100 m, with quadrupole lengths of 4.1 m/7.5 m for the inner/outer quadrupoles of the triplets respectively. This length can hardly be reduced, since it is mainly given by the focusing strength of the quadrupoles. For the estimation of the magnet strength, a beam pipe diameter of 100 mm has been assumed. This corresponds to 3σ of the beam radius after the plasma.
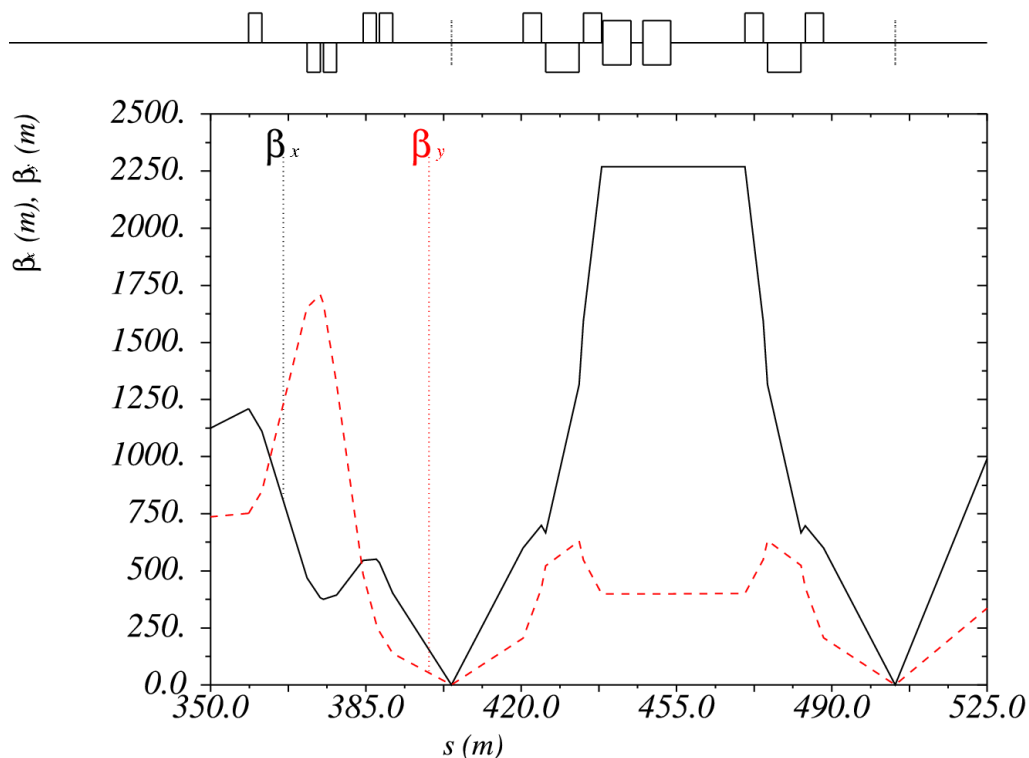

Figure 6.16: The conceptual design of the proton energy spectrometer.
On the x-axis is the distance from the beginning of the β-matching section in m, on the y-axis the horizontal and vertical β functions.
Above is a schematic view of the beam line. The rectangles above (below) the solid line represent horizontally (vertically) focusing quadrupoles, the rectangles centred around the solid line represent dipole magnets. The two dotted lines indicate the position of the two image points. The quadrupoles upstream of the first image point form the final focus system, illustrated in full in figure 6.4.

For this pipe diameter a magnet strength of $30\,\mathrm{T/m}$, corresponding to a peak field of $1.5\,\mathrm{T}$, can be achieved. This still leaves a good margin with respect to iron saturation, so a priori there is no issue for non-superconducting quadrupoles. (Iron quadrupoles can reach up to $2\,\mathrm{T}$ field at the pole face [210].) Ideally, one would like to operate with a larger beam pipe diameter, corresponding to several σ. However, as the availability of significantly stronger magnets seemed questionable, this diameter has been chosen as a starting point.

The effect of the so-called β-beating has been studied to ensure that the condition

$$\frac{D_x \sigma_\delta}{\sqrt{\epsilon\beta}\sqrt{1 + \frac{\Delta\beta(\delta)}{\beta}}} \gg 1 \tag{6.8}$$

is fulfilled, meaning that change in beam size due to dispersion D_x and energy spread σ_δ is much bigger than the change in beam size due to a β-mismatch resulting from an momentum deviating from the reference energy. For that, the quadrupole strength k_{in} of the spectrometer magnets obtained by previous matching has been substituted for $k_{new} = \frac{k_{in}}{1+\delta_{aux}}$ and the energy parameter δ_{aux} has been varied. Studies showed that for the energy deviations expected from results of the plasma simulations, the changes in β are only a few percent. In initial discussions, this effect was not considered to be severe [210]. However, based on the findings described in this chapter, the proton spectrometer was cancelled from the experiment planning for the submission of the LoI. The effect has therefore not been studied in depth.

6.3.5 Proton Spectrometer - Further Comments

1. In general, the resolution of an energy spectrometer can be improved by increasing the length of the drift space s, cf. eq. 6.5. However, this requires that the energy dependent change in trajectory is large in comparison to the beam divergence. As discussed in chapter 6.2.1, this condition is difficult to fulfil for the parameters estimated for the AWAKE experiment.

2. In all the spectrometer images above, only the second half of the proton beam has been used, as explained in section 6.1.2. For a real spectrometer, the first half of the beam would also contribute to the final image. Whilst the emittance of the part of the beam propagating through neutral gas should not deteriorate as badly as the emittance of the beam propagating through plasma, it still produces a background signal.

6.3.6 Electron Spectrometer

Initial studies for an electron energy spectrometer have been performed. Figure 6.17 shows an estimated spectrometer image corresponding to the data described in section 6.2.3. As for the proton bunch, the plasma also modulates the transverse phase space of the electron bunch. However, since the relative energy gain is much stronger, a clear experimental signal is expected.

To also allow low energy electrons to pass the spectrometer dipole, a weak magnetic field has been assumed for the initial studies performed during the course of this work. For the

AWAKE design report, it has been decided to use a much stronger spectrometer dipole magnet. This means that low energy electrons will be lost to the magnet walls due to the strong deflection, but will allow for a much better energy resolution for the high energy particles.
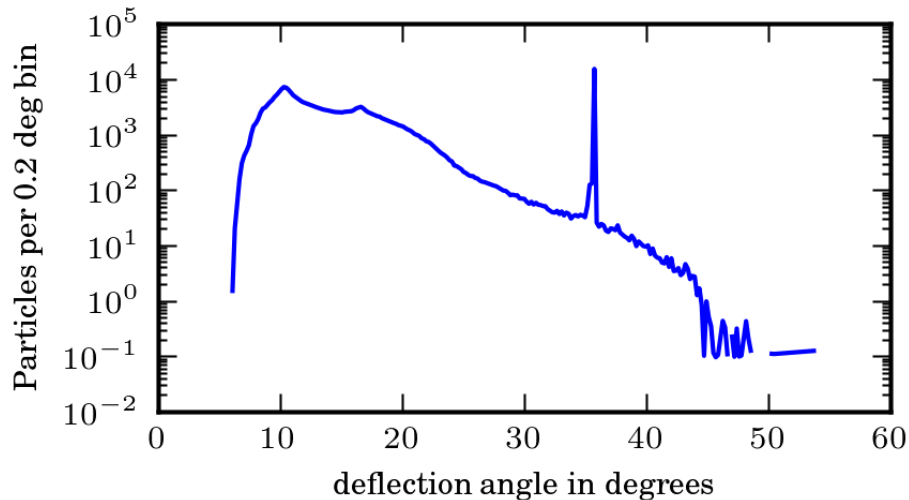

Figure 6.17: A possible electron spectrometer image as generated via equation 6.5 (page 103), for electrons that co-propagated with the driving proton bunch for $7\,\text{m}$, $N_P = 1.15\cdot10^{11}$, and $n_0 = 1\cdot10^{14}\,\text{cm}^{fl3}$. An integrated field strength of $0.04\,\text{Tm}$ is assumed. The peak at $\approx 37°$ corresponds to the initial electron energy of $10\,\text{MeV}$. Published in [206]. ($5.6\cdot10^6$ particles were used in the simulation, corresponding to $2.5\cdot10^5$ electrons. The non-integer numerical weights result in bins with only a fraction of a particle.)

6.4   Summary

For the planned AWAKE experiment, I have evaluated existing beam-plasma simulations with respect to accelerator physics requirements. In particular, I have studied the possibility to diagnose the self-modulation of the proton bunch via a magnetic energy spectrometer. These studies showed that for the given constraints on magnet strength, the effect of the energy modulation is completely overshadowed by the emittance increase of the proton bunch. As a result of my studies, the proton spectrometer has been cancelled from the experiment planning.

Now, it is planned to inject and accelerate electrons already in the early phases of the experiment. My initial studies show that an electron energy spectrometer should give a clear signal of the electron energy gain.

6.5 Status of Experiment Planing

Several aspects of the experimental planning have changed noticeably during the course of this work.

Most obviously, as discussed in more detail in chapter 6.3 (and in particular sections 6.3.3 and 6.3.4), the proton energy spectrometer disappeared from the experimental planning. Initially, it was planned to diagnose the proton beam via a spectrometer as the first phase of the experiment. However, the massive space requirement of at least 100 m; and the very faint signal of the energy modulation lead to the conclusion that a proton spectrometer as main diagnostics would not make for a convincing experiment.

The current experimental planning foresees to inject and accelerate electrons already in the first phase of the experiment. The initial studies carried out in section 6.3.6 indicate that a clear signal should be observable. For the work presented in this thesis, the idea was to use a comparably weak magnet, both to save costs and to allow the detection of all electron energies. This was changed for the AWAKE Design Report (ADR) [19]. The new plan is to use a much stronger, existing magnet. This allows for a much better energy resolution for high electron energies. On the downside, it will not be possible to observe low energy gains and energy loss of electrons, as they will be lost to the magnet walls.

In addition, the upgrade work on the LHC injector chain lead to a noticeable increase in bunch current. The parameters which have been described as *optimal* within this work and the LoI [18] have become the standard case for the ADR. The observations in this work still serve to illustrate the dependence of the energy gain on the charge of the driving bunch.

Furthermore, the location of the envisaged experimental area has changed to the former CNGS area (CERN Neutrinos to Gran Sasso) due to radiation protection considerations. This choice has no influence on the physics described in this chapter.

7. Summary

The highest energy particle accelerator built to date is the LHC, the Large Hadron Collider. To study its findings with higher precision, a high energy lepton collider is desired. However, for the required beam energies, the construction of electron/positron storage rings is impractical, as the amount of energy lost to synchrotron radiation becomes excessive for all practical bending radii. The next generation of lepton colliders will, therefore, consist of linear accelerators. Given the currently achievable acceleration gradients, this will result in facilities with a length of a few tens of kilometres. The hope is that plasma-based acceleration techniques with their significantly higher acceleration gradients will allow to considerably reduce the size and cost of these colliders.

Within this thesis, systematic studies regarding the applicability of plasma based acceleration techniques for technical applications have been performed. These studies included both theoretical investigations and the participation to and planing of experiments.

In particular, possible scenarios for a high energy lepton collider based on plasma wakefield acceleration have been studied. As the technology necessary for the construction of a high energy collider will still take decades to mature, possible earlier applications have been investigated. Specifically, laser-driven plasma wakefield accelerators have been investigated as injectors. Finally, studies for AWAKE, the experiment on proton-driven plasma wakefield acceleration planned at CERN, have been performed. The results regarding these three topics will be summarized separately.

High-Energy Lepton Collider

Recently, the long sought Higgs boson has been discovered at the LHC. To study this discovery with higher precision, a lepton collider is desirable. In this work, three proposals for lepton colliders of the required energy have been developed. In particular, laser pulses, electron bunches and proton bunches have been compared as different driver technologies. For both the electron-driven and the laser-driven scenario, the total wall plug power consumption has been estimated for the parameter range considered most suitable. It has been found to be in the order of a few tens of Megawatts. This is very similar to the power consumption of a facility based on the technology foreseen for ILC or CLIC, the

two most advanced proposals based on conventional accelerator technology (International Linear Collider, Compact LInear Collider).

For the proton driven case, it was shown that for this energy, efficient acceleration in a single stage is not possible. This is due to the fact that to reach a high wall plug efficiency, the drive beam energy should be comparable to the desired energy of the witness bunch. For this energy region, there is still a significant velocity difference between the driving proton bunch and the witness bunch. As a result, rapid phase slippage with the electron witness bunch occurs, stopping the acceleration process.

It is important to point out that, resulting from the short bunch lengths inherent to plasma-based acceleration, the bunch density has to be much higher compared to ILC /CLIC type colliders to achieve the required luminosity. This leads to much stronger detrimental beam-beam interaction at the collision point, resulting in a much higher background signal in the detector and a much higher uncertainty in the initial beam energy. This is even true if no energy spread is acquired during the acceleration process.

Laser Wakefield Accelerator as Injectors for Synchrotron Light Sources

Whilst synchrotron radiation is a detrimental effect in circular high energy colliders, said radiation is used for a multitude of experiments at so-called synchrotron light sources. The short bunch lengths and high bunch charge of laser wakefield accelerators (LWFA) make them very interesting as injectors for said facilities for two reasons: i) The duration of the emitted radiation pulse is proportional to the electron bunch length. The short LWFA bunches would, therefore, allow for a better time resolution. ii) For wavelengths larger than the length of the emitting bunch, coherent amplification occurs. LWFA bunches would, therefore, allow to extend the radiation spectrum far into the THz, a spectral range currently difficult to access with high intensity.

During the course of this work, the injection of LWFA bunches into an electron storage ring has been studied in simulations, using the ANKA synchrotron at KIT as an example. It was shown that the bunch length increases much faster than one would naively assume based on the typical time constants of equilibrium processes. It was shown that this behaviour is caused by the still relatively high energy spread of the LWFA bunches, which leads to differences in revolution time for particles of different energy and in turn a lengthening of the bunch.

It is important to point out that during the lengthening of the bunch, interesting sub-structures in the longitudinal bunch density have been observed. These sub-structures could still lead to very interesting radiation properties. However, the question of reproducibility has to be investigated further.

Energy Spectrometer Studies for the AWAKE Experiment

For AWAKE, the planned proton-driven plasma wakefield experiment at CERN, existing simulations have been investigated with respect to accelerator physics requirements during the course of this thesis. Initially, it was planned to only diagnose the proton beam after the plasma cell, without accelerating any electrons. However, evaluation of the simulation data revealed that the expected energy modulation of the proton beam due to the passage through the plasma is very small compared to the average beam energy. This means that

one would have to diagnose an effect in the tails of the energy distribution, with a low number of particles.

Furthermore, the passage through the plasma cell also influences the transverse properties of the proton beam. This leads to an increase of the beam emittance, its transverse phase space volume. For the initially planed proton energy spectrometer, this emittance increase completely overshadows the effect of the energy modulation. as confirmed by simulations. My results lead to a change of the experiment planing. The proton spectrometer has been cancelled, and it is now planed to already inject and accelerate electrons in the early phase of the experiment. The corresponding simulations have again been evaluated, and here a clear spectrometer signal is expected.

A   List of Acronyms

A list of used acronyms is given in table 7.1.

Acronym	Meaning	Cf. Page
CPA	Chirped Pulse Amplification	13
IP	Interaction Point	9, 49
LWFA	Laser WakeField Accelerator	6, 14
PBWA	Plasma Beat Wave Accelerator	15
PWFA	Plasma Wakefield Accelerator	6, 19
RLPA	Resonant Laser Plasma Accelerator	15
SMLWFA	Self-modulated LWFA	16

Table 7.1: List of Acronyms

B   List of Variables

The variables used in this thesis are summarized. Table 7.2 gives an overview of the variables using Latin characters, Table 7.3 gives an overview of the variables using Greek characters. If not mentioned otherwise, SI units are used.

C   Plasma Simulation Codes

This chapter gives an overview of the different input data files produced by the beam plasma simulations.

Description of Input Beam

For all beam-plasma simulations, the bunches were initialized with the density distribution

$$n_b = \frac{N_p}{2\sigma_r^2 \sigma_z (2\pi)^{3/2}} e^{-\frac{r^2}{2\sigma_r^2}} \cdot \left[1 + \cos\left(\sqrt{\frac{\pi}{2}} \frac{z}{\sigma_z}\right)\right], \quad |z| < \sigma_z\sqrt{2\pi}, \qquad (7.1)$$

with the number of particles N_p and the RMS beam radius σ_r and RMS bunch length σ_z. This is very close to a Gaussian distribution but vanishes at the boundaries of the interval, which is beneficial for simulations.

Symbol	Meaning	Cf. Page
a_0	Laser strength parameter	12
B	Magnetic flux density	
c	Speed of light	
$D(s)$	Dispersion at point s	9
E_0	Cold non-relativistic wave breaking field	11
E_b	Particle beam energy	
E_r	Electric field strength in radial direction	
E_z	Electric field strength in longitudinal direction	
f	Repetition / collision frequency	
F_p	Ponderomotive force	17
k	Normalized quadrupole magnet strength *or* photon wave number	8, 14
k_p	Plasma collision-less skin depth	10
$\mathcal{L}$	Luminosity	48
L_d	Laser dephasing length	19
L_p	Length of plasma	
L_{pd}	Laser pump depletion length	19
L_{stage}	Length of a plasma stage in a multi-stage linear collider	53
L_{stage}	Total length of a linear collider	53
$m_{e/p}$	Electron /proton mass	
n_0	Average plasma electron density	
n_γ	Number of generated beamstrahlung photons per incident particle	49
n_b	Number of generated beamstrahlung coherent pairs per incident particle	50
n_ν	Number of generated beamstrahlung trident pairs per incident particle	51
N, N_b	Number of particles in bunch	
N_{stage}	Number of stages in a multi-stage linear collider	53
P_0	Relativistic power unit, $P_0 = m^2 c^5 / e^2 \simeq 8.7\,\text{GW}$	
P_{avg}	Average laser power	
P_b	Particle beam power $P_b = E_b * N_b * f$	
P_{crit}	Critical laser power, over which self focusing occurs	18
P_{peak}	Laser peak power	
P_{wall}	Wall-plug power consumption	
r_L	RMS laser radius	
s	Distance along beam trajectory	
U_L	Laser pulse energy	
$v_{p/g}$	Phase /group velocity	14
W_{stage}	Energy gain per stage in a multi-stage linear collider	53
z_R	Laser Rayleigh length	13

Table 7.2: List of variables using Latin characters.

Symbol	Meaning	Cf. Page
α_c	Momentum compaction factor	81
β	Beta-function or $\beta = v/c$	8
γ	Photon or Lorentz factor	
δ	Relative energy deviation or phase slippage	9, 22
δ_B	Beamstrahlung generated energy spread	49
ϵ_0, ϵ_r	Permittivity	
$\epsilon_{geo/N}$	Geometric / Normalized emittance	8
η	Conversion efficiency	
λ / λ_L	Photon / Laser wavelength	
λ_p	Plasma wavelength	10
ξ	$\xi = 1$ for linear polarization, $\xi = 2$ for circular polarization	12
ρ	Bending radius in a dipole magnet	103
$\sigma_{r/z}$	RMS bunch radius /length	
τ_L	RMS laser pulse length	
Υ	Average beamstrahlung parameter	49
ω	Photon angular frequency	
ω_p	Plasma angular frequency, $\omega_p = \sqrt{\omega_{pe}^2 + \omega_{pi}^2} \simeq \omega_{pe}$	10
ω_{pe}, ω_{pi}	Plasma electron / ion angular frequency	10

Table 7.3: List of variables using Greek characters.

Calculation of Beam Parameters

The parameters of the initial and final beams were calculated from the particle distributions used in the simulations following the method described in [211]:

$$\epsilon = \left[\sigma_{xx}\sigma_{x'x'} - \sigma_{xx'}^2\right]^{\frac{1}{2}} \tag{7.2}$$

$$\sigma_{xx} = \frac{1}{Q}\sum_{i=1}^{N} q_i\left[(x_i - \bar{x})^2\right] \tag{7.3}$$

$$\sigma_{xx'} = \frac{1}{Q}\sum_{i=1}^{N} q_i\left[(x_i - \bar{x})(x'_i - \bar{x}')\right] \tag{7.4}$$

$$\sigma_{x'x'} = \frac{1}{Q}\sum_{i=1}^{N} q_i\left[(x'_i - \bar{x}')^2\right] \tag{7.5}$$

$$\bar{x} = \frac{1}{Q}\sum_{i=1}^{N} q_i x_i \tag{7.6}$$

$$\bar{x}' = \frac{1}{Q}\sum_{i=1}^{N} q_i x'_i \tag{7.7}$$

$$Q = \sum_{i=1}^{N} q_i \tag{7.8}$$

With x_i, x'_i the transverse position and angle of (macro) particle i and q_i its numerical weight, if applicable.

Note that $\sigma_{xx}, \sigma_{xx'}$, and $\sigma_{x'x'}$ are not standard deviations but covariances. For a Gaussian beam, the density distribution can be expressed with the Twiss parameters α, β as

$$\rho(x, x') = \frac{\beta}{2\pi\sigma_x^2}\exp\left\{-\frac{x^2 + (\alpha x + \beta x')^2}{2\sigma_x^2}\right\}, \quad \int\int \rho(x, x')dxdx' = 1. \tag{7.9}$$

Here, $\sigma_x = \sqrt{\beta\varepsilon}$ is the RMS beam size. If one calculates the covariances

$$\sigma_{xx} = \int\int x^2\rho(x, x')dxdx' \tag{7.10}$$

$$\sigma_{xx'} = \int\int xx'\rho(x, x')dxdx' \tag{7.11}$$

and compares the coefficients, one gets the Twiss parameters

$$\alpha_x = -\frac{\sigma_{xx'}}{\varepsilon_x}, \tag{7.12}$$

$$\beta_x = \frac{\sigma_{xx}}{\varepsilon_x}, \tag{7.13}$$

$$\gamma_x = \frac{1 + \alpha_x^2}{\beta_x}. \tag{7.14}$$

C.1   LCODE

This Section describes the data files created by LCODE [204, 205], which is a radial symmetric hybrid code. This means that the particles are not represented by their 6D phase space coordinates $x, p_x, y, p_y, z, \delta$, as is common in accelerator physics, but by the coordinates z, r, p_z, p_r, M. Here z and p_z are the longitudinal position and momentum, r

and p_r are the radial position and momentum and $M = r \cdot p_\phi$ is the angular momentum, with p_ϕ the momentum in ϕ direction in cylindrical coordinates. A typical distribution of r and p_r is shown in figure C.1. Note that the initial radial distributions does *not* have the shape of a half Gaussian, as one could naively expect. Instead, it peaks at a value $r > 0$. This is due to the fact that for a transversely Gaussian distribution, the number of particles $n(r)$ at a certain radius is given by
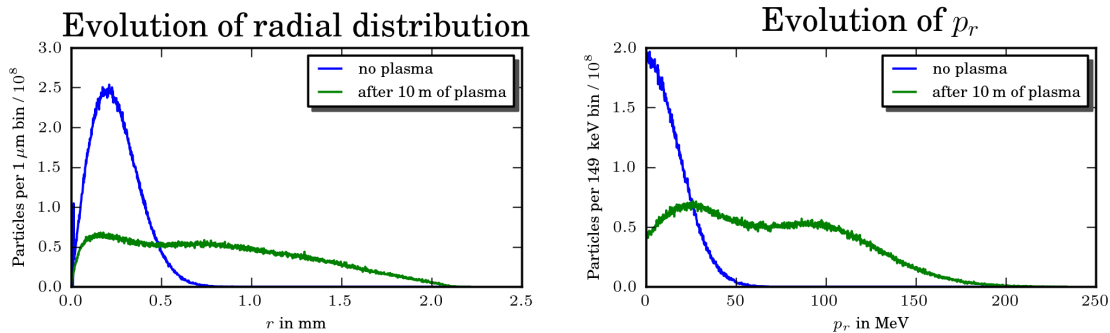
Figure C.1: Left: Shown is the radial particle density. The x-axis gives the distance from the beam centre, the y-axis the number of particles at this radius.
Right: Shown is the distribution of the transverse momentum. The x-axis now gives the transverse momentum instead of the radius.

$$n(r) = 2\pi r \rho, \qquad \rho \propto e^{-\frac{r^2}{2\sigma_r^2}} \tag{7.15}$$

where ρ is the Gaussian density distribution and σ_r is the transverse RMS beam size. From this radial symmetric data, 6D coordinates can be generated via

$$x = r \cdot \cos(\phi), \qquad\qquad\qquad y = r \cdot \sin(\phi), \tag{7.16}$$

$$p_x = p_r \cdot \cos(\phi) - M/r \cdot \sin(\phi), \qquad p_y = p_r \cdot \sin(\phi) + M/r \cdot \cos(\phi) \tag{7.17}$$

with ϕ a random angle in the interval $[0, 2\pi)$. The particle distribution generated this way is Gaussian in the $x-$ and p_x-plane, cf. e.g. figure 6.7, page 97. By construction, the same is true in the $y-$ and p_y-plane respectively.

C.2   VLPL

In VLPL (Virtual Laser Plasma Lab [192]), particles are represented by 8 parameters, $x, y, z, \beta_x, \beta_y, p_z, E, w$, where x, y, z are their position, β_x, β_y are the relativistic $\beta = v/c_0$, p_z is the longitudinal momentum, $E = M_0 c_0^2 (\gamma - 1)$ is the total kinetic energy and w is the numerical weight of the particle. VLPL only tracks particles in a simulation window of approximately $2 \times 2 \, \text{mm}^2$ transverse size. Particles that leave this window are propagated balistically.

D   Hosing

When an electron beam propagates through an underdense plasma, it is subject to a transverse instability called hosing [82–84]. The instability is caused by the coupling of the beam centroid to the electrons at the edge of the ion channel. It is similar to the transverse two-stream instability occurring for lower driver densities and the beam breakup observed in classical linear accelerators. Similarly, it can lead to a degradation of beam brightness and to total beam disruption. The growth of the instability can limit the useful acceleration length and make it difficult to aim the beam [85].

When the beam head propagates through an underdense plasma ($n_b \gg n_0$), it expels *all* the plasma electrons from the beam volume on the time scale of the plasma frequency, $\omega_p \ll \tau_r$, where τ_r is the current rise time. The plasma electrons are expelled up to the charge neutralisation radius $r_n = (n_b/n_0)^{1/2}r_b > r_b$, where r_b is the RMS beam radius [82, 84]. Within this plasma channel, the beam will be strongly focused and undergo betatron oscillations at a well defined frequency. If now a slice of the beam is displaced transversely with respect to the beam head, it will induce a displacement of the electrons in the plasma channel wall at $r = r_n$, which then respond as a simple harmonic oscillator and deflect following portions of the beam. The oscillation frequency along the length of bunch is given by $\omega_0 = \omega_p/(\sqrt{2}c)$ and the beam tail oscillates transversely with $k_\beta = \omega_p/(\sqrt{2\gamma_b}c)$, where γ_b is the relativistic factor of the beam electrons [83]. Under certain conditions, this oscillation can grow exponentially. Assuming $\gamma_b \gg 1$ and linear focusing forces within the plasma channel, the number of e-foldings N_e at a position $\xi = ct - z$ within a beam at a time $\tau = t$ is given by [84, 212]

$$N_e = \pi(3/2)^{3/2}(1/\gamma_b)^{1/6}[(c\tau - \xi)/\lambda_p]^{1/3}(\xi/\lambda_p)^{2/3}. \qquad (7.18)$$

Each e-fold N_e corresponds to a growth of the instability by a factor $e \approx 2.718$. Note that this growth rate is independent of beam density and fluctuations thereof.

It is important to point out that both experiments performed at SLAC [13, 213, 214] and simulations performed in [83] show little or no growth. In [83], this is explained by the fact that at the front of the beam $n_b < n_0$. This results in incomplete blowout and therefore in non-uniform focusing forces, which in turn result in phase mixing at the front of the pulse and reduce the growth rate of the hosing instability.

In the work described above, the positive feedback that causes the instability is between the oscillations of the beam centroid and the plasma electrons that are kept out by its space charge. In [215], hosing has been studied for the case of an electron beam creating the plasma through field ionization. Here, the positive feedback is between the oscillations of the beam centroid and the displaced ion column it creates through ionization. The initially tilted beam creates an ion column which is not symmetric about the beam, there is an offset between the central axis of the beam and the axis of the ion column. Therefore, the ion column creates a deflecting force on the later parts of the beam. The behaviour of the beam has been studied through 3D particle in cell simulations for four different regimes: i) For the preformed plasma, the results from [82] have been reproduced. ii) For the case of a gas with a high ionization potential, i.e. the beam field being near to the ionization threshold. Here, the ionization width is less than the blowout radius and hosing

is strongly suppressed. This is because in this case there are not enough ions created to prevent the created electrons from escaping transversely. They are blown out by the beam field into the neutral gas and do not return, a surrounding electron channel does not form. iii) For the case of a gas with a low ionization potential, where the ionization region is a little wider than the blowout radius. Here some electrons return, leading to to traditional hosing, while the ones that are blown out to the point where they do not return lead to the ionization hosing described above. The result is even worse than for the preformed plasma in case i). iv) The beam field is far above the ionization potential. In this case, the response is similar to case i).

Bibliography

[1] The Official Website of the Nobel Prize. All nobel prizes in physics. http://www.nobelprize.org/nobel_prizes/physics/laureates/, Oct. 2013.

[2] The Official Website of the Nobel Prize. The nobel prize in physics 1905. http://www.nobelprize.org/nobel_prizes/physics/laureates/1905/press.html, Oct. 2013.

[3] LEP design report. Technical Report CERN-LEP-84-01, CERN, Geneva, 1984.

[4] LHC design report. Technical Report CERN-2004-003-V-1, CERN, Geneva, 2004.

[5] Nan Phinney, Nobukasu Toge, and Nicholas Walker. International linear collider reference design report, volume 3: Accelerator, Aug 2007.

[6] Conceptual design report of a multi-TeV linear collider based on CLIC technology, draft, Oct 2011.

[7] James A. Clarke. *The Science and Technology of Undulators and Wigglers (Oxford Series on Synchrotron Radiation)*. Oxford University Press, USA, 2004. ISBN 0198508557.

[8] T. Tajima and J. M. Dawson. Laser electron accelerator. *Phys. Rev. Lett.*, 43(4): 267–270, Jul 1979. doi: 10.1103/PhysRevLett.43.267.

[9] Donna Strickland and Gerard Mourou. Compression of amplified chirped optical pulses. *Optics Communications*, 56(3):219 – 221, 1985. ISSN 0030-4018. doi: 10.1016/0030-4018(85)90120-8. URL http://www.sciencedirect.com/science/article/pii/0030401885901208.

[10] W. P. Leemans, B. Nagler, A. J. Gonsalves, Cs. Toth, K. Nakamura, C. G. R. Geddes, E. Esarey, C. B. Schroeder, and S. M. Hooker. GeV electron beams from a centimetre-scale accelerator. *Nature Physics*, 2(10):696, Oct 2006. doi: 10.1038/nphys418.

[11] Editors: W. Chou, W. Leemans, and M. Uesaka. ICFA beam dynamics newsletter no. 56. http://www-bd.fnal.gov/icfabd/Newsletter56.pdf, Dec 2011.

[12] E. Esarey, P. Sprangle, J. Krall, and A. Ting. Overview of plasma-based accelerator concepts. *Plasma Science, IEEE Transactions on*, 24(2):252 –288, Apr 1996. ISSN 0093-3813. doi: 10.1109/27.509991.

[13] Ian Blumenfeld, Christopher E. Clayton, Franz-Josef Decker, Mark J. Hogan, Chengkun Huang, Rasmus Ischebeck, Richard Iverson, Chandrashekhar Joshi, Thomas Katsouleas, Neil Kirby1, Wei Lu, Kenneth A. Marsh, Warren B. Mori, Patric Muggli, Erdem Oz, Robert H. Siemann, Dieter Walz, and Miaomiao Zhou. Energy doubling of 42 GeV electrons in a metre-scale plasma wakefield accelerator. *Nature*, 445, Feb 2007. doi: 10.1038/nature05538.

[14] R. D. Ruth, A. W. Chao, P. L. Morton, and P. B. Wilson. A plasma wake field accelerator. *Part. Accel.*, 17:171 – 189, Jul 1984. SLAC-PUB-3374.

[15] Allen Caldwell, Konstantin Lotov, Alexander Pukhov, and Frank Simon. Proton-driven plasma-wakefield acceleration. *Nature Physics*, 5, Apr 2009. doi: 10.1038/nphys1248.

[16] CMS Collaboration. Observation of a new boson at a mass of 125 GeV with the CMS experiment at the LHC. *Physics Letters B*, 716(1):30 – 61, 2012. ISSN 0370-2693. doi: 10.1016/j.physletb.2012.08.021. URL http://www.sciencedirect.com/science/article/pii/S0370269312008581.

[17] ATLAS Collaboration. Observation of a new particle in the search for the standard model higgs boson with the ATLAS detector at the LHC. *Physics Letters B*, 716 (1):1 – 29, 2012. ISSN 0370-2693. doi: 10.1016/j.physletb.2012.08.020. URL http://www.sciencedirect.com/science/article/pii/S037026931200857X.

[18] Allen Caldwell et al. Letter of intent for a demonstration experiment in proton-driven plasma wakefield acceleration. Technical Report CERN-SPSC-2011-020. SPSC-I-240, CERN, Geneva, Jun 2011.

[19] A Caldwell, E Gschwendtner, K Lotov, P Muggli, and M Wing. AWAKE design report a proton-driven plasmawakefield acceleration experiment at CERN. Technical Report CERN-SPSC-2013-013. SPSC-TDR-003, CERN, Geneva, Apr 2013.

[20] E. Esarey, C. B. Schroeder, and W. P. Leemans. Physics of laser-driven plasma-based electron accelerators. *Rev. Mod. Phys.*, 81(3):1229–1285, Aug 2009. doi: 10.1103/RevModPhys.81.1229.

[21] C. B. Schroeder, E. Esarey, C. G. R. Geddes, C. Benedetti, and W. P. Leemans. Physics considerations for laser-plasma linear colliders. *Phys. Rev. ST Accel. Beams*, 13(10):101301, Oct 2010. doi: 10.1103/PhysRevSTAB.13.101301.

[22] C. B. Schroeder, C. Benedetti, E. Esarey, F. J. Grüner, and W. P. Leemans. Growth and phase velocity of self-modulated beam-driven plasma waves. *Phys. Rev. Lett.*, 107:145002, Sep 2011. doi: 10.1103/PhysRevLett.107.145002. URL http://link.aps.org/doi/10.1103/PhysRevLett.107.145002.

[23] T. C. Katsouleas, S. Wilks, P. Chen, J. M. Dawson, and J. J. Su. Beam loading efficiency in plasma accelerators. *Part. Accel.*, 22:81–99, 1987.

[24] C. B. Schroeder, E. Esarey, C. Benedetti, Cs, C. G. R. Geddes, and W. P. Leemans. Design Considerations for Plasma Accelerators Driven by Lasers or Particle Beams. *AIP Conference Proceedings*, 1299(1):60–66, 2010. doi: 10.1063/1.3520397. URL http://dx.doi.org/10.1063/1.3520397.

[25] Klaus Wille. *Physik der Teilchenbeschleuniger und Synchrotronstrahlungsquellen: eine Einführung.* Teubner-Studienbücher: Physik. Teubner, Stuttgart, 1992. ISBN 3-519-03087-X.

[26] Helmut Wiedemann. *Particle accelerator physics*, volume 1: Basic principles and linear beam dynamics. Springer, Berlin, 2. ed. edition, 1999. ISBN 3-540-64671-X.

[27] Horst Stöcker. *Taschenbuch der Physik : Formeln, Tabellen, Übersichten.* Harri Deutsch, Frankfurt am Main, 2007. ISBN 3-8171-1720-5 ; 3-8171-1721-3 ; 978-3-8171-1720-8 ; 978-3-8171-1721-5. Nachdr. der 5., korr. Aufl.

[28] Chao. *Handbook of Accelerator Physics and Engineering.* World Scientific Publishing Company, 1999. ISBN 9810235003.

[29] B. Autin, editor. *BeamOptics A Programm for Analytical Beam Optics.* CERN, Geneva, 1998.

[30] J. D. Lawson. *The Physics of Charged-Particle Beams*, chapter 6.2. Internat. Ser. Mono. Phys. Clarendon Press, Oxford, 2 edition, 1988.

[31] John M. Dawson. Nonlinear electron oscillations in a cold plasma. *Phys. Rev.*, 113 (2):383–387, Jan 1959. doi: 10.1103/PhysRev.113.383.

[32] Wei Lu. *Nonlinear Plasma Wakefield Theory and Optimum Scaling for Laser Wakefield Acceleration in the Blowout Regime.* PhD thesis, University of California, Los Angeles, USA, 2006.

[33] Rüdiger Paschotta, editor. *Encyclopedia of Laser Physics and Technology.* Wiley-VCH, 1 edition, 2008. ISBN 3527408282.

[34] Kay-Uwe Amthor. *Laser plasma accelerators for charged particles.* PhD thesis, Friedrich-Schiller-Universität, Jena, Germany, 2006.

[35] J. Meyer-ter-Vehn and A. Pukhov. Relativistic laser plasma interaction: I. analytical tools. Lecture Notes.

[36] Hans-Peter Schlenvoigt, Oliver Jäckel, Sebastian M. Pfotenhauer, and Malte C. Kaluza. Laser-based particle acceleration. In Mikhail Grishin, editor, *Advances in Solid State Lasers Development and Applications.* InTech, 2010. ISBN 978-953-7619-80-0. URL http://www.intechopen.com/articles/show/title/laser-based-particle-acceleration.

[37] P. M. Woodward. A method of calculating the field over a plane aperture required to produce a given polar diagram. *J. Inst. Elect. Eng.*, 93:1554, 1947.

[38] J. D. Lawson. Lasers and accelerators. *Nuclear Science, IEEE Transactions on*, 26 (3):4217 –4219, Jun 1979. ISSN 0018-9499. doi: 10.1109/TNS.1979.4330749.

[39] Robert B. Palmer. A laser driven grating linac. *Part. Accel.*, 11(Print-80-0475): 81–90. 28 p, May 1980.

[40] K. Nakajima, D. Fisher, T. Kawakubo, H. Nakanishi, A. Ogata, Y. Kato, Y. Kitagawa, R. Kodama, K. Mima, H. Shiraga, K. Suzuki, K. Yamakawa, T. Zhang, Y. Sakawa, T. Shoji, Y. Nishida, N. Yugami, M. Downer, and T. Tajima. Observation of ultrahigh gradient electron acceleration by a self-modulated intense short laser pulse. *Phys. Rev. Lett.*, 74:4428–4431, May 1995. doi: 10.1103/PhysRevLett.74.4428. URL http://link.aps.org/doi/10.1103/PhysRevLett.74.4428.

[41] D. Umstadter, S.-Y. Chen, A. Maksimchuk, G. Mourou, and R. Wagner. Nonlinear optics in relativistic plasmas and laser wake field acceleration of electrons. *Science*, 273(5274):472–475, 1996. doi: 10.1126/science.273.5274.472. URL http://www.sciencemag.org/content/273/5274/472.abstract.

[42] J. Faure, Y. Glinec, A. Pukhov, S. Kiselev, S. Gordienko, E. Lefebvre, J.-P. Rousseau, F. Burgy, and V. Malka. A laser-plasma accelerator producing monoenergetic electron beams. *Nature*, 431(7008):541, Sep 2004. doi: 10.1038/nature02963.

[43] C. G. R. Geddes, Cs. Toth, J. van Tilborg, E. Esarey, C. B. Schroeder, D. Bruhwiler, C. Nieter, J. Cary, and W. P. Leemans. High-quality electron beams from a laser wakefield accelerator using plasma-channel guiding. *Nature*, 431(7008):538, Sep 2004. doi: 10.1038/nature02963.

[44] S. P. D. Mangles, C. D. Murphy, Z. Najmudin, A. G. R. Thomas, J. L. Collier, A. E. Dangor, E. J. Divall, P. S. Foster, J. G. Gallacher, C. J. Hooker, D. A. Jaroszynski, A. J. Langley, W. B. Mori, P. A. Norreys, F. S. Tsung, R. Viskup, B. R. Walton, and K. Krushelnick. Monoenergetic beams of relativistic electrons from intense laser-plasma interactions. *Nature*, 431(7008):535, Sep 2004. doi: doi:10.1038/nature02939.

[45] Naveen Kumar, Alexander Pukhov, and Konstantin Lotov. Self-modulation instability of a long proton bunch in plasmas. *arXiv:1003.5816v1*, Mar 2010.

[46] M. N. Rosenbluth and C. S. Liu. Excitation of plasma waves by two laser beams. *Phys. Rev. Lett.*, 29:701–705, Sep 1972. doi: 10.1103/PhysRevLett.29.701. URL http://link.aps.org/doi/10.1103/PhysRevLett.29.701.

[47] C. M. Tang, P. Sprangle, and R. N. Sudan. Dynamics of space-charge waves in the laser beat wave accelerator. *Physics of Fluids*, 28(6):1974–1983, 1985. ISSN 00319171. doi: DOI:10.1063/1.865375. URL http://dx.doi.org/10.1063/1.865375.

[48] V. I. Berezhiani and I. G. Murusidze. Interaction of highly relativistic short laser pulses with plasmas and nonlinear wake-field generation. *Physica Scripta*, 45(2):87, 1992. URL http://stacks.iop.org/1402-4896/45/i=2/a=007.

[49] D. Umstadter, E. Esarey, and J. Kim. Nonlinear plasma waves resonantly driven by optimized laser pulse trains. *Phys. Rev. Lett.*, 72:1224–1227, Feb 1994. doi: 10.1103/ PhysRevLett.72.1224. URL http://link.aps.org/doi/10.1103/PhysRevLett.72.1224.

[50] C. Joshi, T. Tajima, J. M. Dawson, H. A. Baldis, and N. A. Ebrahim. Forward raman instability and electron acceleration. *Phys. Rev. Lett.*, 47:1285–1288, Nov 1981. doi: 10.1103/PhysRevLett.47.1285. URL http://link.aps.org/doi/10.1103/PhysRevLett. 47.1285.

[51] E. Esarey and A. Ting. Comment on "cascade focusing in the beat-wave accelerator". *Phys. Rev. Lett.*, 65:1961–1961, Oct 1990. doi: 10.1103/PhysRevLett.65.1961. URL http://link.aps.org/doi/10.1103/PhysRevLett.65.1961.

[52] C. B. Schroeder, E. Esarey, C. G. R. Geddes, Cs. Toth, B. A. Shadwick, J. van Tilborg, J. Faure, and W. P. Leemans. Frequency chirp and pulse shape effects in self-modulated laser wakefield accelerators. *Physics of Plasmas*, 10(5):2039–2046, 2003. ISSN 1070664X. doi: DOI:10.1063/1.1560614. URL http://dx.doi.org/10. 1063/1.1560614.

[53] W. P. Leemans, P. Catravas, E. Esarey, C. G. R. Geddes, C. Toth, R. Trines, C. B. Schroeder, B. A. Shadwick, J. van Tilborg, and J. Faure. Electron-yield enhancement in a laser-wakefield accelerator driven by asymmetric laser pulses. *Phys. Rev. Lett.*, 89:174802, Oct 2002. doi: 10.1103/PhysRevLett.89.174802. URL http://link.aps. org/doi/10.1103/PhysRevLett.89.174802.

[54] W.P. Leemans, C.W. Siders, E. Esarey, N.E. Andreev, G. Shvets, and W.B. Mori. Plasma guiding and wakefield generation for second-generation experiments. *Plasma Science, IEEE Transactions on*, 24(2):331 –342, apr 1996. ISSN 0093-3813. doi: 10.1109/27.509997.

[55] Paul Gibbon. *Short Pulse Laser Interactions with Matter: An Introduction*. Imperial Coll., London, 2005.

[56] W.B. Mori. The physics of the nonlinear optics of plasmas at relativistic intensities for short-pulse lasers. *Quantum Electronics, IEEE Journal of*, 33(11):1942 –1953, Nov 1997. ISSN 0018-9197. doi: 10.1109/3.641309.

[57] P. Sprangle, Cha-Mei Tang, and E. Esarey. Relativistic self-focusing of short-pulse radiation beams in plasmas. *Plasma Science, IEEE Transactions on*, 15(2):145 –153, april 1987. ISSN 0093-3813. doi: 10.1109/TPS.1987.4316677.

[58] B. A. Shadwick, C. B. Schroeder, and E. Esarey. Nonlinear laser energy depletion in laser-plasma accelerators. *Physics of Plasmas*, 16(5):056704, 2009. doi: 10.1063/ 1.3124185. URL http://link.aip.org/link/?PHP/16/056704/1.

[59] Pisin Chen, J. M. Dawson, Robert W. Huff, and T. Katsouleas. Acceleration of electrons by the interaction of a bunched electron beam with a plasma. *Phys. Rev. Lett.*, 54:693–696, Feb 1985. doi: 10.1103/PhysRevLett.54.693. URL http://link. aps.org/doi/10.1103/PhysRevLett.54.693.

[60] Pisin Chen, J. M. Dawson, Robert W. Huff, and T. Katsouleas. Acceleration of electrons by the interaction of a bunched electron beam with a plasma. *Phys. Rev. Lett.*, 55:1537–1537, Sep 1985. doi: 10.1103/PhysRevLett.55.1537. URL http://link.aps.org/doi/10.1103/PhysRevLett.55.1537.

[61] J. B. Rosenzweig, D. B. Cline, B. Cole, H. Figueroa, W. Gai, R. Konecny, J. Norem, P. Schoessow, and J. Simpson. Experimental observation of plasma wake-field acceleration. *Phys. Rev. Lett.*, 61(1):98, Jul 1988. doi: 10.1103/PhysRevLett.61.98.

[62] S. Lee, T. Katsouleas, R. G. Hemker, E. S. Dodd, and W. B. Mori. Plasma-wakefield acceleration of a positron beam. *Phys. Rev. E*, 64(4):045501, Sep 2001. doi: 10.1103/PhysRevE.64.045501.

[63] Pisin Chen, J. J. Su, J. M. Dawson, K. L. F. Bane, and P. B. Wilson. Energy transfer in the plasma wake-field accelerator. *Phys. Rev. Lett.*, 56(12):1252–1255, Mar 1986. doi: 10.1103/PhysRevLett.56.1252.

[64] G. Dugan. Advanced accelerator system requirements for future linear colliders. *AIP Conference Proceedings*, 737(1):29–60, 2004. doi: 10.1063/1.1842533. URL http://link.aip.org/link/?APC/737/29/1.

[65] J. P. Delahaye, G. Guignard, T. Raubenheimer, and I. Wilson. Scaling laws for e$^+$/e$^-$ linear colliders. *Nuclear Instruments and Methods in Physics Research A*, 421:369–405, February 1999. doi: 10.1016/S0168-9002(98)01132-2.

[66] Alain Blondel, Alex Chao, Weiren Chou, Jie Gao, Daniel Schulte, and Kaoru Yokoya. Report of the ICFA beam dynamics workshop 'accelerators for a higgs factory: linear vs. circular' (hf2012). *arXiv:1302.3318*, Feb 2013. URL http://arxiv.org/abs/1302.3318.

[67] K. V. Lotov. Simulation of proton driven plasma wakefield acceleration. *Phys. Rev. ST Accel. Beams*, 13(4):041301, Apr 2010. doi: 10.1103/PhysRevSTAB.13.041301.

[68] G. Xia, A. Caldwell, K. Lotov, A. Pukhov, and R. Assmann. Preliminary study of proton driven plasma wakefield accleration. *Proceedings of PAC09*, 2009.

[69] A. Pukhov, N. Kumar, T. Tückmantel, A. Upadhyay, K. Lotov, P. Muggli, V. Khudik, C. Siemon, and G. Shvets. Phase velocity and particle injection in a self-modulated proton-driven plasma wakefield accelerator. *Phys. Rev. Lett.*, 107: 145003, Sep 2011. doi: 10.1103/PhysRevLett.107.145003. URL http://link.aps.org/doi/10.1103/PhysRevLett.107.145003.

[70] K. V. Lotov. Current understanding of PWA perspectives at PS and SPS. *Internal Note*, Mar 2010.

[71] G. Xia, A. Caldwell, and P. Muggli. Some considerations in realizing a TeV linear collider based on PDPWA scheme. *Proceedings of IPAC11*, 2011.

[72] Konstantin V. Lotov. Optimum angle for side injection of electrons into linear plasma wakefields. *arXiv:1108.6081v1*, 2011. URL http://arxiv.org/abs/1109.6081v1.

[73] J. B. Rosenzweig, B. Breizman, T. Katsouleas, and J. J. Su. Acceleration and focusing of electrons in two-dimensional nonlinear plasma wake fields. *Phys. Rev. A*, 44(10):R6189–R6192, Nov 1991. doi: 10.1103/PhysRevA.44.R6189.

[74] A. Pukhov and J. Meyer-ter Vehn. Laser wake field acceleration: the highly non-linear broken-wave regime. *Applied Physics B*, 74(4-5):355–361, 2002. ISSN 0946-2171. doi: 10.1007/s003400200795. URL http://dx.doi.org/10.1007/s003400200795.

[75] S. Gordienko and A. Pukhof. Scalings for ultrarelativistic laser plasmas and quasi-monoenergetic electrons. *Phys. Plasmas*, 12(4):043109, Apr 2005. doi: 10.1063/1.1884126.

[76] D. A. Jaroszynski, R. Bingham, and R. A. Cairns, editors. *Laser-Plasma Interactions*. Scottish Graduate Series. CRC Press, 1 edition, 2009.

[77] K. A. Marsh et al. Beam matching to a plasma wake field accelerator using a ramped density profile at the plasma boundary. *Proceedings of PAC05*, 2005.

[78] P. Muggli, B. E. Blue, C. E. Clayton, S. Deng, F.-J. Decker, M. J. Hogan, C. Huang, R. Iverson, C. Joshi, T. C. Katsouleas, S. Lee, W. Lu, K. A. Marsh, W. B. Mori, C. L. O'Connell, P. Raimondi, R. Siemann, and D. Walz. Meter-scale plasma-wakefield accelerator driven by a matched electron beam. *Phys. Rev. Lett.*, 93(1):014802, Jun 2004. doi: 10.1103/PhysRevLett.93.014802.

[79] C. E. Clayton, B. E. Blue, E. S. Dodd, C. Joshi, K. A. Marsh, W. B. Mori, S. Wang, P. Catravas, S. Chattopadhyay, E. Esarey, W. P. Leemans, R. Assmann, F. J. Decker, M. J. Hogan, R. Iverson, P. Raimondi, R. H. Siemann, D. Walz, T. Katsouleas, S. Lee, and P. Muggli. Transverse envelope dynamics of a 28.5-GeV electron beam in a long plasma. *Phys. Rev. Lett.*, 88(15):154801, Apr 2002. doi: 10.1103/PhysRevLett.88.154801.

[80] N. Barov and J. B. Rosenzweig. Propagation of short electron pulses in underdense plasmas. *Phys. Rev. E*, 49:4407–4416, May 1994. doi: 10.1103/PhysRevE.49.4407. URL http://link.aps.org/doi/10.1103/PhysRevE.49.4407.

[81] N. Kirby et al. Emittance growth from multiple coulomb scattering in a plasma wakefield accelerator. *Proceedings of PAC07*, 2007.

[82] David H. Whittum, William M. Sharp, Simon S. Yu, Martin Lampe, and Glenn Joyce. Electron-hose instability in the ion-focused regime. *Phys. Rev. Lett.*, 67:991–994, Aug 1991. doi: 10.1103/PhysRevLett.67.991. URL http://link.aps.org/doi/10.1103/PhysRevLett.67.991.

[83] E. S. Dodd, R. G. Hemker, C.-K. Huang, S. Wang, C. Ren, W. B. Mori, S. Lee, and T. Katsouleas. Hosing and sloshing of short-pulse GeV-class wakefield drivers. *Phys. Rev. Lett.*, 88:125001, Mar 2002. doi: 10.1103/PhysRevLett.88.125001. URL http://link.aps.org/doi/10.1103/PhysRevLett.88.125001.

[84] J. Krall and G. Joyce. Transverse equilibrium and stability of the primary beam in the plasma wake-field accelerator. *Physics of Plasmas*, 2(4):1326–1331, Apr 1995.

[85] C. Huang, W. Lu, M. Zhou, C. E. Clayton, C. Joshi, W. B. Mori, P. Muggli, S. Deng, E. Oz, T. Katsouleas, M. J. Hogan, I. Blumenfeld, F. J. Decker, R. Ischebeck, R. H. Iverson, N. A. Kirby, and D. Walz. Hosing instability in the blow-out regime for plasma-wakefield acceleration. *Phys. Rev. Lett.*, 99:255001, Dec 2007. doi: 10. 1103/PhysRevLett.99.255001. URL http://link.aps.org/doi/10.1103/PhysRevLett. 99.255001.

[86] S. Hillenbrand, R. Assmann, and P. Muggli. A multi-parameter optimization of plasma density for an advanced linear collider. *Proceedings of IPAC11*, 2011.

[87] J. B. Rosenzweig, A. M. Cook, A. Scott, M. C. Thompson, and R. B. Yoder. Effects of ion motion in intense beam-driven plasma wakefield accelerators. *Phys. Rev. Lett.*, 95:195002, Oct 2005. doi: 10.1103/PhysRevLett.95.195002. URL http://link.aps. org/doi/10.1103/PhysRevLett.95.195002.

[88] Reza Gholizadeh, Tom Katsouleas, Patric Muggli, and Warren Mori. Preservation of ultra low emittances using adiabatic matching in future plasma wakefield-based colliders. *AIP Conference Proceedings*, 1086(1):575–579, 2009. doi: 10.1063/1.3080971. URL http://link.aip.org/link/?APC/1086/575/1.

[89] R. Gholizadeh, T. Katsouleas, P. Muggli, C. Huang, and W. Mori. Preservation of beam emittance in the presence of ion motion in future high-energy plasma-wakefield-based colliders. *Phys. Rev. Lett.*, 104:155001, Apr 2010. doi: 10.1103/PhysRevLett. 104.155001. URL http://link.aps.org/doi/10.1103/PhysRevLett.104.155001.

[90] Reza Gholizadeh, Tom Katsouleas, Patric Muggli, and Warren Mori. Analysis of ion motion and scattering in the extreme regime of high intensity electron beams in plasma wakefield accelerators. *AIP Conference Proceedings*, 877(1):504–510, 2006. doi: 10.1063/1.2409176. URL http://link.aip.org/link/?APC/877/504/1.

[91] Miaomiao Zhou. *Accelerating Ultra-short Electron/Positron Bunches in Field Ionization Produced Plasmas*. PhD thesis, University of California, Los Angeles, 2008.

[92] J.E. Leiss. Beam loading in linear accelerators. *IEEE Transactions on Nuclear Science*, Jun 1965.

[93] Ralph Assmann, Weiren Chou, Dino Jaroszynski Eric Esarey, Yun Liu, Mike Seidel Tor Raubenheimer, Toshiki Tajima, and Kaoru Yokoya. Laser applications for future high-energy and high- intensity accelerators. www-bd.fnal.gov/icfabd/workshopreport_chapter1.pdf, 2011.

[94] C. Rechatin, J. Faure, X. Davoine, O. Lundh, J. Lim, A. Ben-Ismail, F. Burgy, A. Tafzi, A. Lifschitz, E. Lefebvre, and V. Malka. Characterization of the beam loading effects in a laser plasma accelerator. *New Journal of Physics*, 12(4):045023, 2010. doi: 10.1088/1367-2630/12/4/045023. URL http://stacks.iop.org/1367-2630/ 12/i=4/a=045023.

[95] S van der Meer. Improving the power efficiency of the plasma wakefield accelerator. Technical Report CERN-PS-85-65-AA. CLIC-Note-3, CERN, Geneva, 1985.

[96] P. Muggli, V. Yakimenko, M. Babzien, E. Kallos, and K. P. Kusche. Generation of trains of electron microbunches with adjustable subpicosecond spacing. *Phys. Rev. Lett.*, 101(5):054801, Jul 2008. doi: 10.1103/PhysRevLett.101.054801.

[97] A. Modena, Z. Najmudin, A. E. Dangor, C. E. Clayton, K. A. Marsh, C. Joshi, V. Malka, C. B. Darrow, C. Danson, D. Neely, and F. N. Walsh. Electron acceleration from the breaking of relativistic plasma waves. *Nature*, 377:606 – 608, 1995. doi: 10.1038/377606a0.

[98] S. Karsch, J. Osterhoff, A. Popp, T. P. Rowlands-Rees, Zs. Major, M. Fuchs, B. Marx, R. Hörlein, K. Schmid, L. Veisz, S. Becker, U. Schramm, B. Hidding, G. Pretzler, D. Habs, F. Grüner, F. Krausz, and S. M. Hooker. GeV-scale electron acceleration in a gas-filled capillary discharge waveguide. *New Journal of Physics*, 9 (11):415, 2007. URL http://stacks.iop.org/1367-2630/9/i=11/a=415.

[99] S M Wiggins, R C Issac, G H Welsh, E Brunetti, R P Shanks, M P Anania, S Cipiccia, G G Manahan, C Aniculaesei, B Ersfeld, M R Islam, R T L Burgess, G Vieux, W A Gillespie, A M MacLeod, S B van der Geer, M J de Loos, and D A Jaroszynski. High quality electron beams from a laser wakefield accelerator. *Plasma Physics and Controlled Fusion*, 52(12):124032, 2010. URL http://iopscience.iop.org/0741-3335/52/12/124032.

[100] O. Lundh, J. Lim, C. Rechatin, L. Ammoura, A. Ben-Ismail, X. Davoine, G. Gallot, J.-P. Goddet, E. Lefebvre, V. Malka, and et al. Few femtosecond, few kiloampere electron bunch produced by a laser-plasma accelerator. *Nature Physics*, 7(3):219–222, 2011. URL http://www.nature.com/doifinder/10.1038/nphys1872.

[101] Takashi Kameshima, Wei Hong, Kiyohiro Sugiyama, Xianlun Wen, Yuchi Wu, Chuanming Tang, Qihua Zhu, Yuqiu Gu, Baohan Zhang, Hansheng Peng, Shin ichi Kurokawa, Liming Chen, Toshiki Tajima, Tetsuro Kumita, and Kazuhisa Nakajima. 0.56 GeV laser electron acceleration in ablative-capillary-discharge plasma channel. *Applied Physics Express*, 1(6):066001, 2008. doi: 10.1143/APEX.1.066001. URL http://apex.jsap.jp/link?APEX/1/066001/.

[102] J. Osterhoff, A. Popp, Zs. Major, B. Marx, T. P. Rowlands-Rees, M. Fuchs, M. Geissler, R. Hörlein, B. Hidding, S. Becker, E. A. Peralta, U. Schramm, F. Grüner, D. Habs, F. Krausz, S. M. Hooker, and S. Karsch. Generation of stable, low-divergence electron beams by laser-wakefield acceleration in a steady-state-flow gas cell. *Phys. Rev. Lett.*, 101:085002, Aug 2008. doi: 10.1103/PhysRevLett.101.085002. URL http://link.aps.org/doi/10.1103/PhysRevLett.101.085002.

[103] C. E. Clayton, J. E. Ralph, F. Albert, R. A. Fonseca, S. H. Glenzer, C. Joshi, W. Lu, K. A. Marsh, S. F. Martins, W. B. Mori, A. Pak, F. S. Tsung, B. B. Pollock, J. S. Ross, L. O. Silva, and D. H. Froula. Self-guided laser wakefield acceleration

beyond 1 GeV using ionization-induced injection. *Phys. Rev. Lett.*, 105:105003, Sep 2010. doi: 10.1103/PhysRevLett.105.105003. URL http://link.aps.org/doi/10.1103/PhysRevLett.105.105003.

[104] Haiyang Lu, Mingwei Liu, Wentao Wang, Cheng Wang, Jiansheng Liu, Aihua Deng, Jiancai Xu, Changquan Xia, Wentao Li, Hui Zhang, Xiaoming Lu, Cheng Wang, Jianzhou Wang, Xiaoyan Liang, Yuxin Leng, Baifei Shen, Kazuhisa Nakajima, Ruxin Li, and Zhizhan Xu. Laser wakefield acceleration of electron beams beyond 1 GeV from an ablative capillary discharge waveguide. *Applied Physics Letters*, 99(9): 091502, 2011. doi: 10.1063/1.3626042. URL http://link.aip.org/link/?APL/99/091502/1.

[105] C. E. Clayton, K. A. Marsh, A. Dyson, M. Everett, A. Lal, W. P. Leemans, R. Williams, and C. Joshi. Ultrahigh-gradient acceleration of injected electrons by laser-excited relativistic electron plasma waves. *Phys. Rev. Lett.*, 70:37–40, Jan 1993. doi: 10.1103/PhysRevLett.70.37. URL http://link.aps.org/doi/10.1103/PhysRevLett.70.37.

[106] J. Arther et al. *Linac Coherent Light Source (LCLS) Conceptual Design Report.* SLAC, 2002.

[107] R. Akre et al. Commissioning of the LCLS linac and bunch compressors. *Proceedings of FEL09*, 2008.

[108] Romain Ganter, editor. *SwissFEL Conceptual Design Report.* Paul Scherer Institut, Jul 2010.

[109] M. J. Hogan, T. O. Raubenheimer, A. Seryi, P. Muggli, T. Katsouleas, C. Huang, W. Lu, W. An, K. A. Marsh, W. B. Mori, C. E. Clayton, and C. Joshi. Plasma wakefield acceleration experiments at FACET. *New Journal of Physics*, 12(5):055030, 2010. URL http://stacks.iop.org/1367-2630/12/i=5/a=055030.

[110] Massimo Altarelli et al., editor. *The European X-Ray Free-Electron Laser Technical Design Report.* DESY XFEL Project Group, Jul 2007. ISBN 978-3-935702-17-1.

[111] FERMI@Elettra Design Team. *FERMI@Elettra Conceptual Design Report.* Sincrotrone Trieste, Jan 2007.

[112] S. Hillenbrand, R. Assmann, A.-S Müller, and D. Schulte. Considerations for a higgs facility based on laser wakefield acceleration. *Proceedings of IPAC13*, 2013.

[113] The national ignition facility: An overview. *Energy and Technology Review*, Dec. 1994.

[114] Breanna Bishop. Lawrence livermore's national ignition facility achieves record laser energy in pursuit of fusion ignition. https://www.llnl.gov/news/newsreleases/2012/Mar/NR-12-03-02.html, Mar. 2012.

[115] Bob Yirka.   Nif facility fires record laser shot into target chamber. http://phys.org/news/2012-03-nif-facility-laser-shot-chamber.html, Mar. 2012.

[116] F. Amiranoff et al. Proposal for a european extreme light infrastructure (ELI), Jun 2007. ELI Scientific Case.

[117] ELI - extreme light infrastructure whitebook, 2011.

[118] Laserlab Europe.   Access facilities GSI - PHELIX.   http://www.laserlab-europe.net/transnational-access/access-facilities/access-facilities-gsi, Apr. 2011.

[119] GSI. PHELIX laser facility. https://www.gsi.de/en/start/research/forschungsgebiete _und_experimente/appa_pni_gesundheit/plasma_physicsphelix/phelix.htm,   FEB. 2013.

[120] A. Bayramian et al. High-average-power femto-petawatt laser pumped by the mercury laser facility. *J. Opt. Soc. Am. B*, 25(7):B57–B61, Jul 2008. doi: 10.1364/ JOSAB.25.000B57. URL http://josab.osa.org/abstract.cfm?URI=josab-25-7-B57.

[121] W. P. Leemans et al. The berkeley lab laser accelerator (bella): A 10 GeV laser plasma accelerator. *Proceedings of PAC11*, 2011.

[122] Scottish Centre for the Application of Plasma-based Accelerators.   Facilities. http://www.scapa.ac.uk/?page_id=103, Apr. 2011.

[123] Laboratoire d'optique appliquée.   Experimental facilities.   http://loa.ensta-paristech.fr/installations_lang_EN_menu_2, FEB. 2013.

[124] H. J. Kong et al. Current trends in laser fusion driver and beam combination laser systems using stimulated brillouin scattering phase conjugate mirrors for a fusion driver. *Journal of the Korean Physical Society*, 56(1):177–183, Jan. 2010.

[125] Osaka University Institute of Laser Engineering. Annual progress report 2007, 2008.

[126] M. Dunne. A high-power laser fusion facility for europe. *nature physics*, 2:2, Jan. 2006. doi: doi:10.1038/nphys208.

[127] M. Dunne et al. *HiPER Technical Background and Conceptual Design Report*, chapter 9 - Baseline Facility Design. 2007.

[128] G. A. Mourou, D. Hulin, and A. Galvanauskas. The Road to High Peak Power and High Average Power Lasers: Coherent-Amplification-Network (CAN). In M. Lontano and D. Batani, editors, *Superstrong Fields in Plasmas*, volume 827 of *American Institute of Physics Conference Series*, pages 152–163, April 2006. doi: 10.1063/1. 2195207.

[129] Toshiki Tadjima Gerard Mourou.   ICAN and 100GeV's ascent. http://indico.cern.ch/conferenceDisplay.py?confId=187383, May 2012.   Presented at EuroNNAc 2012 meeting.

[130] Gerard Mourou. Private Communication.

[131] STFC Central Laser Facility. Overview of astra gemini. http://www.clf.stfc.ac.uk/Facilities/Astra/Astra+Gemini/12258.aspx, FEB. 2013.

[132] Jason Cole et al., 2013. Private Communication.

[133] Jonathan Wood et al., 2013. Private Communication.

[134] J. Osterhoff et al. Transport and non-invasive position detection of electron beams from laser-plasma accelerators. *Proceedings of AAC2010*, 2010.

[135] R. Fedele, G. Miano, and V. G. Vaccaro. The plasma undulator. *Physica Scripta*, 1990(T30):192, 1990. URL http://stacks.iop.org/1402-4896/1990/i=T30/a=026.

[136] S. Corde and K. Ta Phuoc. Plasma wave undulator for laser-accelerated electrons. *Physics of Plasmas (1994-present)*, 18(3):033111, 2011. doi: http://dx.doi.org/10.1063/1.3569827. URL http://scitation.aip.org/content/aip/journal/pop/18/3/10.1063/1.3569827.

[137] J. Borer. Instrumentation and diagnostics used in LEP commissioning, with accent on the LEP beam orbit measurement system. Technical Report CERN/SL/90-107, CERN, Geneva, 1990.

[138] LAOLA - LAboratory fOr Laser- and beam-driven plasma Acceleration. http://laola.desy.de/, 2012.

[139] SPARC - Sorgente Pulsata Auto-amplificata di Radiazione Coerente. http://www.lnf.infn.it/acceleratori/sparc/, 2012.

[140] C. Huang, W. An, C. Clayton, C. Joshi, W. Lu, K. Marsh, W. Mori, M. Tzoufras, T. Katsouleas, I. Blumenfeld, M.J. Hogan, N. Kirby, T. Raubenheimer, A. Seryi, and P. Muggli. Simulations of 25 GeV PWFA sections: Path towards a PWFA linear collider. *Proceedings of PAC09*, 2009.

[141] Helmut Wiedemann. *Particle Accelerator Physics*, volume 2: Nonlinear and Higher-Order Beam Dynamics. Springer-Verlag, 1995. ISBN 0387575642.

[142] ILC Collaboration. ILC home page. http://linearcollider.org/, 2011.

[143] CLIC Collaboration. CLIC home page. http://clic-study.org/, 2011.

[144] W. Leemans and E. Esarey. Laser-driven plasma-wave electron accelerators. *Physics Today*, 62(3):44–49, 2009. ISSN 00319228. doi: DOI:10.1063/1.3099645. URL http://dx.doi.org/10.1063/1.3099645.

[145] J. Rosenzweig, N. Barov, E. Colby, and P. Colestock. A linear collider based on nonlinear plasma wake-field acceleration. *Proceedings of Snowmass '96*, pages 394–398, 1996.

[146] J. Rosenzweig, N. Barov, A. Murokh, E. Colby, and P. Colestock. Towards a plasma wake-field acceleration-based linear collider. *Nuclear Instruments and Methods in Physics Research Section A: Accelerators, Spectrometers, Detectors and*

Associated Equipment, 410(3):532 – 543, 1998. ISSN 0168-9002. doi: DOI:10. 1016/S0168-9002(98)00186-7. URL http://www.sciencedirect.com/science/article/ pii/S0168900298001867.

[147] A. Seryi et al. A concept of plasma wake field acceleration linear collider (PWFA-LC). *Proceedings of PAC09*, 2009.

[148] S. Lee, T. Katsouleas, P. Muggli, W. B. Mori, C. Joshi, R. Hemker, E. S. Dodd, C. E. Clayton, K. A. Marsh, B. Blue, S. Wang, R. Assmann, F. J. Decker, M. Hogan, R. Iverson, and D. Walz. Energy doubler for a linear collider. *Phys. Rev. ST Accel. Beams*, 5(1):011001, Jan 2002. doi: 10.1103/PhysRevSTAB.5.011001.

[149] Tor O. Raubenheimer. An afterburner at the ILC: The collider viewpoint. *AIP Conference Proceedings*, 737(1):86–94, 2004. doi: 10.1063/1.1842536. URL http: //link.aip.org/link/?APC/737/86/1.

[150] Chandrashekhar Joshi and Thomas Katsouleas. Plasma accelerators at the energy frontier and on tabletops. *Physics Today*, 56(6), Jun 2003.

[151] Chandrashekhar Joshi. Plasma accelerators. *Scientific American*, page 40, Feb 2006.

[152] Andrei Seryi. Multi-TeV upgrade concept for international linear collider based on proton driven plasma acceleration. *ILC-Note-2010-052*, May 2010.

[153] Vitaly Yakimenko and Tom Katsouleas. Proton-based driver for the plasma wakefield accelerator with TeV reach. *Plasma Physics and Controlled Fusion*, 53(8):085010, 2011. URL http://stacks.iop.org/0741-3335/53/i=8/a=085010.

[154] Vladimir D. Shiltsev. High energy particle colliders: past 20 years, next 20 years and beyond. *Usp.Fiz.Nauk*, 2012.

[155] C. B. Schroeder, E. Esarey, and W. P. Leemans. Beamstrahlung considerations in laser-plasma-accelerator-based linear colliders. *Phys. Rev. ST Accel. Beams*, 15: 051301, May 2012. doi: 10.1103/PhysRevSTAB.15.051301. URL http://link.aps. org/doi/10.1103/PhysRevSTAB.15.051301.

[156] Kazuhisa Nakajima et al. Operating plasma density issues on large-scale laser-plasma accelerators toward high-energy frontier. *Phys. Rev. ST Accel. Beams*, 14:091301, Sep 2011. doi: 10.1103/PhysRevSTAB.14.091301. URL http://link.aps.org/doi/10. 1103/PhysRevSTAB.14.091301.

[157] Kaoru Yokoya and Pisin Chen. Beam-beam phenomena in linear colliders. *KEK Preprint*, 91-2, 1990.

[158] Pisin Chen. Disruption effects from the collision of quasi-flat beams. In *Particle Accelerator Conference, 1993., Proceedings of the 1993*, pages 617 –619 vol.1, May 1993. doi: 10.1109/PAC.1993.308793.

[159] Chao. *Handbook of Accelerator Physics and Engineering*, chapter 2.6.2. World Scientific Publishing Company, 1999. ISBN 9810235003.

[160] W. P. Leemans, R. Duarte, E. Esarey, S. Fournier, C. G. R. Geddes, D. Lock-hart, C. B. Schroeder, C. Toth, J.-L. Vay, and S. Zimmermann. The BErke-ley Lab Laser Accelerator (BELLA): A 10 GeV laser plasma accelerator. *AIP Conference Proceedings*, 1299(1):3–11, 2010. doi: 10.1063/1.3520352. URL http://link.aip.org/link/?APC/1299/3/1.

[161] Andrei Seryi. Future prospects of accelerator science for particle physics. *Nucl. Instr. Meth. A*, 623(1):23 – 28, 2010. ISSN 0168-9002. doi: 10.1016/j.nima.2010.02.145. URL http://www.sciencedirect.com/science/article/pii/S0168900210004122. 1st International Conference on Technology and Instrumentation in Particle Physics.

[162] K. V. Lotov. Acceleration of positrons by electron beam-driven wakefields in a plasma. *Physics of Plasmas*, 14(2):023101, 2007. doi: 10.1063/1.2434793. URL http://link.aip.org/link/?PHP/14/023101/1.

[163] P. Muggli. Positron beams propagation in plasma wakefield accelerators. *Proceedings of LINAC08*, 2008.

[164] W. An et al. Positron acceleration by using a particle beam-driven wake field in plasma. *Proceedings of PAC99*, 1999.

[165] G. Xia, A. Caldwell, and P. Muggli. Future colliders based on a modulated proton bunch driven plasma wakefield acceleration. *Proceedings of IPAC12*, 2012.

[166] J. L. Abelleira Fernandez et al. A large hadron electron collider at cern: Report on the physics and design concepts for machine and detector. *arXiv:1206.2913v2*, Sep. 2012. URL http://arxiv.org/abs/1206.2913.

[167] Valery Telnov. Principles of photon colliders. *Nuclear Instruments and Methods in Physics Research Section A: Accelerators, Spectrometers, Detectors and Associated Equipment*, 355(1):3 – 18, 1995. ISSN 0168-9002. doi: 10.1016/0168-9002(94)01173-7. URL http://www.sciencedirect.com/science/article/pii/0168900294011737.

[168] V. Telnov. Photon collider technology overview. *Proceedings of Photon09*, 2009.

[169] Valery Telnov. Ultimate luminosities and energies of photon colliders. *AIP Conference Proceedings*, 397(1):259–273, 1997. doi: 10.1063/1.52997. URL http://link.aip.org/link/?APC/397/259/1.

[170] P. Chen. An introduction to beamstrahlung and disruption. In M. Month and S. Turner, editors, *Frontiers of Particle Beams*, volume 296 of *Lecture Notes in Physics*, pages 495–532. Springer Verlag, 1988. doi: 10.1007/BFb0031506.

[171] Kwang-Je Kim and Andrew Sessler. Gamma-gamma colliders. *Beam Line*, 26(1):16–22, 1996.

[172] D. Asner et al. Higgs physics with a $\gamma\gamma$ collider based on CLIC 1. *The European Physical Journal C - Particles and Fields*, 28:27–44, Mar. 2003. ISSN 1434-6044. URL http://dx.doi.org/10.1140/epjc/s2002-01113-3. 10.1140/epjc/s2002-01113-3.

[173] David H. Whittum, Andrew M. Sessler, John J. Stewart, and Simon S. Yu. Plasma Suppression of Beamstrahlung. *Part.Accel.*, 34:89–104, 1990.

[174] N.A. Solyak. COLLISION EFFECTS IN COMPENSATED BUNCHES OF LINEAR COLLIDERS. *Novosibirsk Preprint*, 88-44, 1988.

[175] J. B. Rosenzweig, B. Autin, and Pisin Chen. Instability of compensated beam-beam collisions. *AIP Conference Proceedings*, 193(1):324–339, 1989. doi: 10.1063/1.38740. URL http://link.aip.org/link/?APC/193/324/1.

[176] Daniel Schulte. Private Communication.

[177] Camille Bibeau, Paul J. Wegner, and Ruth Hawley-Fedder. UV sources: World's largest laser to generate powerful ultraviolet beams. *Laser Focus World*, Jun. 2006. URL http://www.laserfocusworld.com/articles/print/volume-42/issue-6/features/uv-sources-worldrsquos-largest-laser-to-generate-powerful-ultraviolet-beams.html.

[178] J. Vieira, C.-K. Huang, W. B. Mori, and L. O. Silva. Polarized beam conditioning in plasma based acceleration. *Phys. Rev. ST Accel. Beams*, 14:071303, Jul 2011. doi: 10.1103/PhysRevSTAB.14.071303. URL http://link.aps.org/doi/10.1103/PhysRevSTAB.14.071303.

[179] Mauro Trovo. Fermi / machine. http://www.elettra.trieste.it/FERMI/index.php?n=Main.Machine, Jan 2012.

[180] Paul Scherer Institut. SwissFEL accelerator. http://www.psi.ch/swissfel/swissfel-accelerator, 2012.

[181] Bolko Beutner. Emittance measurement procedures for the SwissFEL 250 MeV injector. *Proceedings of FEL2009*, 2009.

[182] DESY's XFEL Project Group. List of beam parameters for the XFEL linac. http://xfel.desy.de/technical_information/electron_beam_parameter/, 2012.

[183] M. Tzoufras, W. Lu, F. S. Tsung, C. Huang, W. B. Mori, T. Katsouleas, J. Vieira, R. A. Fonseca, and L. O. Silva. Beam loading in the nonlinear regime of plasma-based acceleration. *Phys. Rev. Lett.*, 101(14):145002, Sep 2008. doi: 10.1103/PhysRevLett.101.145002.

[184] B. B. Pollock, C. E. Clayton, J. E. Ralph, F. Albert, A. Davidson, L. Divol, C. Filip, S. H. Glenzer, K. Herpoldt, W. Lu, K. A. Marsh, J. Meinecke, W. B. Mori, A. Pak, T. C. Rensink, J. S. Ross, J. Shaw, G. R. Tynan, C. Joshi, and D. H. Froula. Demonstration of a narrow energy spread, $\sim$ 0.5 GeV electron beam from a two-stage laser wakefield accelerator. *Phys. Rev. Lett.*, 107:045001, Jul 2011. doi: 10.1103/PhysRevLett.107.045001. URL http://link.aps.org/doi/10.1103/PhysRevLett.107.045001.

[185] C. McGuffey, A. G. R. Thomas, W. Schumaker, T. Matsuoka, V. Chvykov, F. J. Dollar, G. Kalintchenko, V. Yanovsky, A. Maksimchuk, K. Krushelnick, V. Yu.

Bychenkov, I. V. Glazyrin, and A. V. Karpeev. Ionization induced trapping in a laser wakefield accelerator. *Phys. Rev. Lett.*, 104:025004, Jan 2010. doi: 10.1103/ PhysRevLett.104.025004. URL http://link.aps.org/doi/10.1103/PhysRevLett.104. 025004.

[186] A.J. Gonsalves et al. Tunable laser plasma accelerator based on longitudinal density tailoring. *Nat Phys*, 7:862–866, November 2011. doi: 10.1038/nphys2071.

[187] J. Faure, C. Rechatin, A. Norlin, A. Lifschitz, Y. Glinec, and V. Malka. Controlled injection and acceleration of electrons in plasma wakefields by colliding laser pulses. *Nature*, 444(7120):737–739, December 2006. ISSN 0028-0836. doi: 10.1038/nature05393. URL http://dx.doi.org/10.1038/nature05393.

[188] G. Fuchert, A. Bernhard, S. Ehlers, P. Peiffer, R. Rossmanith, and T. Baumbach. A novel undulator concept for electron beams with a large energy spread. *Nuclear Instruments and Methods in Physics Research Section A: Accelerators, Spectrometers, Detectors and Associated Equipment*, 672(0):33 – 37, 2012. ISSN 0168-9002. doi: 10.1016/j.nima.2011.12.097. URL http://www.sciencedirect.com/science/ article/pii/S0168900211023436.

[189] C. Widmann et al. Design of a dispersive beam transport line for the JETI laser wakefield accelerator. *Proceedings of IPAC11*, 2011.

[190] ELI - Extreme Light Infrastructure. http://www.eli-beams.eu/about/, 2013.

[191] A.-S. Müller et al. Far infrared coherent synchrotron edge radiation at ANKA. *Proceedings of PAC05*, 2005.

[192] Alexander Pukhov. Three-dimensional electromagnetic relativistic particle-in-cell code VLPL (virtual laser plasma lab). *Journal of Plasma Physics*, 61(3):425, 1999. doi: 10.1017/s0022377899007515.

[193] HDF Group. http://www.hdfgroup.org/hdf-java-html/hdfview/, 2013.

[194] S. Hillenbrand, R. Assmann, A.-S Müller, V. Judin, O. Jansen, and A. Pukhov. Study of laser wakefield accelerators as injectors for synchrotron light sources. *Proceedings of IPAC13*, 2013.

[195] S. Hillenbrand, R. Assmann, A.-S Müller, V. Judin, O. Jansen, and A. Pukhov. Study of laser wakefield accelerators as injectors for synchrotron light sources. *Nuclear Instruments and Methods in Physics Research Section A: Accelerators, Spectrometers, Detectors and Associated Equipment*, 740(0):153 – 157, 2014. Proceedings of the first European Advanced Accelerator Concepts Workshop 2013.

[196] W. Herr and F. Schmidt. A MAD-X primer. *CERN-AB-2004-027-ABP*, Jun 2004.

[197] M. Winkler et al. Development and test of iron-free quadrupole lenses with high magnetic flux densities. *Nuclear Instruments and Methods in Physics Research Section B: Beam Interactions with Materials and Atoms*, 204(0):454 – 459, 2003. ISSN

0168-583X. doi: 10.1016/S0168-583X(02)02120-1. URL http://www.sciencedirect.com/science/article/pii/S0168583X02021201.

[198] P. Antici, A. Bacci, C. Benedetti, E. Chiadroni, M. Ferrario, A. R. Rossi, L. Lancia, M. Migliorati, A. Mostacci, L. Palumbo, and L. Serafini. Laser-driven electron beamlines generated by coupling laser-plasma sources with conventional transport systems. *Journal of Applied Physics*, 112(4):044902, 2012. doi: http://dx.doi.org/10.1063/1.4740456. URL http://scitation.aip.org/content/aip/journal/jap/112/4/10.1063/1.4740456.

[199] Vitali Judin. Private Communication.

[200] A. Terebilo. Accelerator toolbox for matlab. *SLAC-PUB-9732*, 2001.

[201] CERN Document Server. Cern-di-0812015. http://cds.cern.ch/record/1260465, Jan. 2012.

[202] C. Hessler, R. Assman, B. Goddard, M. Meddahi, and W. Weterings. Beam line design for the CERN HiRadMat test facility. *Proceedings of PAC09*, 2009.

[203] Allen Caldwell. Private Communication.

[204] K.V. Lotov. Simulation of ultrarelativistic Beam Dynamics in Plasma Wake-Field Accelerator. *Physics f Plasmas*, 5:785–791, 1998. doi: 10.1063/1.872765.

[205] K. V. Lotov. Fine wakefield structure in the blowout regime of plasma wakefield accelerators. *Phys. Rev. ST Accel. Beams*, 6(6):061301, Jun 2003. doi: 10.1103/PhysRevSTAB.6.061301.

[206] S. Hillenbrand, R. Assmann, A.-S. Müller, and T. Tückmantel. Energy spectrometer studies for proton-driven plasma acceleration. *Proceedings of IPAC11*, 2011.

[207] Patric Muggli. Private Communication.

[208] David C. Cary. *The Optics of Charged Particle Beams*. Accel. Storage Rings. Hardwood Academic Publishers, Chur, 1 edition, 1987.

[209] Klaus G Steffen. *High energy beam optics*. Internat. Sci. Mono. Texts Phys. Astron. Interscience, New York, NY, 1965.

[210] Stephane Fartoukh. Private Communication.

[211] R. Assmann, C. Adolphsen, K. Bane, P. Emma, T. Raubenheimer, R. Siemann, K. Thompson, and F. Zimmermann. LIAR - a computer program for the modeling and simulation of high performance linacs. *SLAC/AP,Äì103*, 1997.

[212] Martin Lampe, Glenn Joyce, Steven P. Slinker, and David H. Whittum. Electron-hose instability of a relativistic electron beam in an ion-focusing channel. *Phys. Fluids B*, 5(6):1888–1901, 1993. ISSN 08998221. doi: DOI:10.1063/1.860772. URL http://dx.doi.org/10.1063/1.860772.

[213] M. J. Hogan, C. D. Barnes, C. E. Clayton, F. J. Decker, S. Deng, P. Emma, C. Huang, R. H. Iverson, D. K. Johnson, C. Joshi, T. Katsouleas, P. Krejcik, W. Lu, K. A. Marsh, W. B. Mori, P. Muggli, C. L. O'Connell, E. Oz, R. H. Siemann, and D. Walz. Multi-GeV energy gain in a plasma-wakefield accelerator. *Phys. Rev. Lett.*, 95:054802, Jul 2005. doi: 10.1103/PhysRevLett.95.054802. URL http://link.aps.org/doi/10.1103/PhysRevLett.95.054802.

[214] Brent Edward Blue. Hosing instability of the drive electron beam in the e157 plasma-wakefield acceleration experiment at the stanford linear accelerator, 2000.

[215] S. Deng, C. D. Barnes, C. E. Clayton, C. O'Connell, F. J. Decker, R. A. Fonseca, C. Huang, M. J. Hogan, R. Iverson, D. K. Johnson, C. Joshi, T. Katsouleas, P. Krejcik, W. Lu, W. B. Mori, P. Muggli, E. Oz, F. Tsung, D. Walz, and M. Zhou. Hose instability and wake generation by an intense electron beam in a self-ionized gas. *Phys. Rev. Lett.*, 96:045001, Jan 2006. doi: 10.1103/PhysRevLett.96.045001. URL http://link.aps.org/doi/10.1103/PhysRevLett.96.045001.

Acknowledgements